Functionality and versatility of aggregation-induced emission luminogens

Guangxue Feng, Ryan T. K. Kwok, Ben Zhong Tang, and Bin Liu

Citation: Applied Physics Reviews **4**, 021307 (2017); doi: 10.1063/1.4984020
View online: http://dx.doi.org/10.1063/1.4984020
View Table of Contents: http://aip.scitation.org/toc/are/4/2
Published by the American Institute of Physics

APPLIED PHYSICS REVIEWS

Functionality and versatility of aggregation-induced emission luminogens

Guangxue Feng,[1,a)] Ryan T. K. Kwok,[2,a)] Ben Zhong Tang,[2,b)] and Bin Liu[1,b)]
[1]*Department of Chemical and Biomolecular Engineering, National University of Singapore, 4 Engineering Drive 4, Singapore 117585*
[2]*Department of Chemistry, The Hong Kong University of Science and Technology, Clear Water Bay, Kowloon, Hong Kong, China*

(Received 6 December 2016; accepted 24 April 2017; published online 8 June 2017)

Breakthrough innovations in light-emitting materials have opened new exciting avenues for science and technology over the last few decades. Aggregation-induced emission (AIE) represents one of such innovations. It refers to a unique light-emitting phenomenon, in which luminescent materials that are non-emissive in molecular state can be induced to emit efficiently in aggregated state. The design and development of AIE luminogens (AIEgens) have overcome technical and fundamental limitations that exist in conventional light-emitting materials, and thus generate great opportunities for various applications. In this review, we aim to introduce the wonderful world of AIE to scientists from different disciplines by summarizing the recent progress made in this exciting research field. The mechanistic analyses and the working principles of the AIE processes are first elaborated, which reveal the restriction of intramolecular motions as the main cause for the AIE effect. The different molecular engineering strategies for the design of new AIEgens are subsequently discussed with examples of various AIEgen systems. The recent high-tech applications of AIEgens as optoelectronic materials, chemical sensors, and biomedical probes are presented and discussed. We hope that this review will stimulate more research interest from physics, chemistry, life science, and biomedical fields to this wonderland of AIE. *Published by AIP Publishing.*
[http://dx.doi.org/10.1063/1.4984020]

TABLE OF CONTENTS

I. INTRODUCTION

Light has been playing fundamental roles in science, technology, and the whole human society. As light is indispensable to human beings, the year of 2015 was proclaimed as the "International Year of Light and Light-based Technologies" by the United Nations. The breathtaking

[a)]G. Feng and R. T. K. Kwok contributed equally to this work.
[b)]Authors to whom correspondence should be addressed: tangbenz@ust.hk, Tel.: 852-2358-7375 and cheliub@nus.edu.sg, Tel.: (65) 65168049, Fax: (65) 67791936.

understanding of light-emitting processes and the development of luminescent materials have provided exciting opportunities in medicine, scientific discoveries, and high-tech innovations over the history, as light gives us the new "eye" to visualize the physical, chemical, and biological species and processes that have never been seen before. It is not surprising that light-based materials and techniques have been issued three Nobel Prize awards in the past decade. One was for the work on green fluorescent proteins (GFP) in 2008,[1] and the other two were for the work on light-emitting diodes (LEDs) and the development of super-resolved fluorescence microscopy in 2014.[2,3] With such a strong support and motivation from scientific community, it is expected that the research of luminescent materials will continue to evolve and remain as a hot topic in the future decades.

As a major class of luminescent materials, organic molecules have found their indispensable positions in numerous practical applications varying from optoelectronic field to biomedical research, due to their easy synthesis, convenient modification, and great accessibility.[4] Solid state or aggregate state has represented the most active physical state for these applications. For example, solid films and crystals are used in organic light-emitting diodes (OLEDs), organic field-effect transistors (OFETs), etc. In biomedical applications, although functional groups with water solubility are often conjugated with organic luminescent molecules, the intrinsic hydrophobicity of organic molecules almost always leads to aggregate formation in physiological microenvironments or aqueous buffer. In aggregate state, conventional organic molecules usually show weakened or totally diminished emission as compared to their single molecular state, which is referred to as aggregation-caused quenching (ACQ).[5] The studies of ACQ have been continued over the past half century, and most of the conventional aromatic luminescent materials suffer from different degrees of ACQ effect although they emit strong fluorescence as isolated molecules. In the aggregate state, the aromatic backbones of organic molecules, especially for those organic dyes with rod or disk-like shapes, pack in close proximity and hence experience intense intermolecular π-π stacking interactions. Along with this π-π stacking interaction, the non-radiative pathway dominates the relaxation of the exciton energy, which leads to fluorescence quenching. Considerable efforts have been made through chemical, physical, and engineering approaches to mitigate this notorious ACQ effect, but with limited success due to the natural tendency of aggregate formation of most organic molecules.[6]

In 2001, we observed a phenomenon that is a reverse of ACQ effect: non-emissive luminogens at isolated molecular state can be induced to emit strong fluorescence upon aggregate formation.[7] This novel phenomenon was named as aggregation-induced emission (AIE), and the luminogens with AIE characteristics were later termed as AIEgens. The very first coined AIEgen was hexaphenylsilole (HPS),[8] which is almost non-emissive when it is molecularly dissolved in a good solvent, such as tetrahydrofuran (THF), but shows bright green fluorescence in solid state or in the mixture of water/THF with high water fractions due to the formation of HPS aggregates. Ever since then, the family of AIEgens has rapidly expanded, and various approaches have been developed to design novel AIEgens or convert conventional ACQ fluorophores to be AIE-active.[9] The fluorescence turn-on mechanism is interpreted as the restriction of intramolecular motions (RIM).[10] The free active rotation, vibration, or other molecular motions of the flexible segments of AIEgens consume energy and cause the radiationless exciton energy dissipation, while the aggregates restrict such energy consuming pathways, leading to radiational dissipation and intensified emission. The development of AIEgens and exploration of the AIE mechanism further deepen our understanding of photophysical processes beyond the ACQ phenomenon, which provides the conceptual guidelines for multidisciplinary and interdisciplinary applications, from optoelectronic systems including liquid crystal displays (LCDs), OLEDs, OFETs, wave-guiding to biomedical research such as ion detection, disease diagnosis, and therapeutics.[9–16]

In this review, we introduce the great opportunities of AIE and AIEgens to the readers and scientists from different disciplines. We first interpret the guiding concepts and working mechanisms of AIE processes, followed by the demonstration of different molecular engineering approaches to convert ACQ fluorophores to AIEgens. Various AIE systems from small molecules to macromolecules and unconventional systems are subsequently presented. At last, novel technological applications of AIEgens are discussed. Considering the rapid development of AIE research in recent years, and the numerous excellent review papers appeared in different journals,[9–16] herein, we would like to limit the scope of these technological applications developed in the past three years. With this review, we hope to stimulate new ideas and inspire new endeavors in this emerging wonderful world of AIE.

II. AIE MECHANISMS

Study of the AIE phenomenon and mechanisms helps deepen our understanding of the fundamental photophysical processes of light-emitting and exciton dissipation, which potentially leads to new theory for luminescence processes. The understanding also guides the design of new AIE systems with unique functions and properties to further widen their applications. Since 2001, researchers from different perspectives have been continuously exploring the real mechanisms that contribute to the AIE phenomenon.[7] Various hypothesized mechanisms have been raised, including J-aggregate formation, conformational planarization, twisted intramolecular charge transfer (TICT), etc.[10] These hypotheses can explain the AIE phenomenon for some specific examples, none of them is generally applicable to most AIE systems. After over one-decade effort from many experiments and also theoretical studies, the mechanism of AIE has evolved from the restriction of intramolecular rotations (RIR) to restriction of intramolecular vibrations (RIV) and finally to restriction of intramolecular motions (RIM), which includes both RIR and RIV. As active intramolecular motions are able to effectively dissipate the exciton energy to the diminished luminescence, any process that can cause RIM process is able to activate radiation dissipation with turn-on fluorescence.[10]

The RIR mechanism is proposed based on the iconic examples of AIEgens, HPS, and tetraphenylethene (TPE, **1**, Fig. 1). TPE consists of four phenyl rings through a

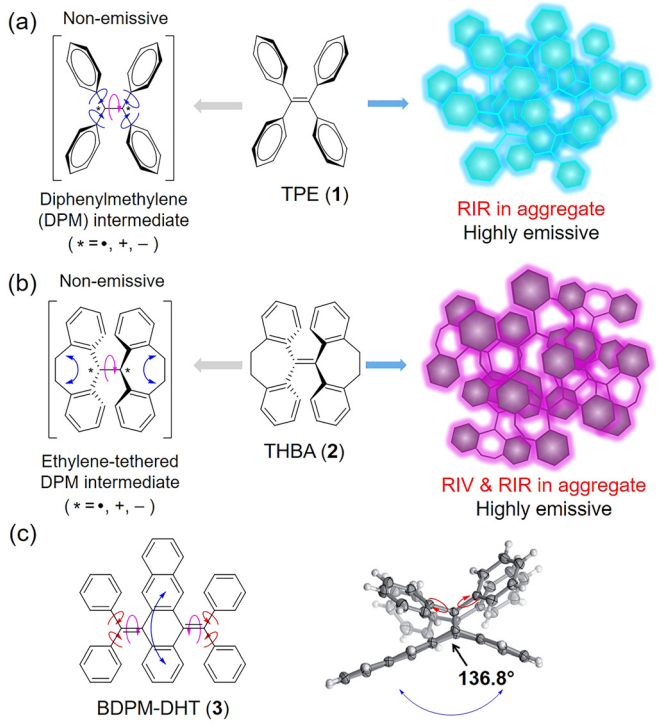

FIG. 1. Schematic illustration of AIE mechanism. (a) TPE (**1**) due to RIR; (b) THBA (**2**), and (c) BDPM-DHT (**3**) due to RIV + RIR (RIM). Reproduced with permission from Mei *et al*., Adv. Mater. **26**, 5429 (2014). Copyright 2014 Wiley-VCH.

connection of a C=C double bond, which takes a propeller-like structure with large torsion angles [Fig. 1(a)].[17] As a single molecule, TPE forms a diphenylmethylene (DPM) intermediate, and the four phenyl rings are able to undergo intramolecular rotation freely with negligible fluorescence. TPE is insoluble in water, and water is usually used as the poor solvent to induce aggregate formation. Due to its highly twisted conformation, the face-to-face packing and π-π stacking interaction become impossible in aggregate state, and blue emission of TPE is thus largely intensified in water when compared to that in THF solution. Various approaches to activate the RIR process have been proposed to turn-on the fluorescence of TPE and its derivatives. Enhancing the steric effect is an efficient way to activate the RIR process.[18] Decorating phenyl rings with multiple methyl groups at *o*-positions of TPE is able to elevate the rotational barriers with high steric hindrance and to activate the RIR process even in molecular state, and the resultant TPE derivative shows bright emission with a fluorescence quantum yield (η) of 64% in THF.[18] This directly validates the RIR hypothesis. Locking the rotor through covalent bonds is another effective way to activate the RIR process.[19] Using the "O" bridge to lock one pair of phenyl rings, its η in solution increased to 4.6% as compared to negligible η of TPE in solution. When two sets of phenyl rings are locked, its solution η further increased to 30.1%. The locking of phenyl rings suppresses the rotational motions, and the exciton energy cannot be depleted through a non-radiation pathway, leading to high emission in molecular state. Since the TPE derivatives with two "O" bridges still exhibited twisted conformation, it showed emission in solution and solid states, making it neither AIE-nor ACQ active. Besides these covalent bonds blocking rotational motions, other physical processes also have been introduced to modulate the RIR processes. For example, TPE derivatives have been incorporated with oligonucleotides to afford TPE-DNA bioconjugates to utilize the DNA hybridization process to increase the physical constraint and block phenyl rings rotations of TPE to realize DNA hybridization by means of fluorescence turn-on.[20] In addition, a coordination process can also activate RIR processes as exampled by tetrakis(bisurea)-functionalized TPE, whose fluorescence is negligible in solution but can be induced to turn on over the complexation with anions such as sulfates or phosphates.[21,22] Apart from experimental examinations, theoretical calculations and simulations also provided conventional evidence on activation of the RIR process to realize the AIE phenomenon.[23,24]

With the advances of AIE study, new AIEgens without rotatable units have been reported, where their AIE process could not be explainable by the RIR process, but they are still AIE active. One of the particular examples is 10,10',11,11'-tetrahydro-5,5'-bidibenzo[a,d][7]annulenylidene (THBA) [**2**, Fig. 1(b)].[25,26] THBA comprises no rotatable phenyl rings. Each pair of phenyl rings is linked and blocked by ethylene tethers. THBA is AIE-active as it exhibits no emission in solution and becomes highly fluorescent as aggregates. Any molecular motion is able to consume energy, which should not only be limited to rotations, but also applicable to vibrations. In this regard, RIV reserves the energy for radiative dissipation and is responsible for the AIE mechanism of THBA, although RIR can also come into play. The quantum mechanics and molecular mechanics (QM/MM) modelling further supported this RIV concept.[26] As an isolated molecule, six vibrational modes coexist for THBA, which consume a very large amount of excited-state energy up to 5639 cm^{-1}, while only three vibrational modes are present when THBA is in cluster with reduced consumption of the excited-state energy of 4016 cm^{-1}. The reduced vibration modes together with the 30% of energy consumption enable the radiative decay pathway for THBA, and lead to the AIE effect.

Now, it has become clear that the working mechanism for AIE involves both RIR and RIV processes, which is termed as RIM, where M (motion) refers to any molecular actions including, rotations, and vibrations such bending, twisting, scissoring, flapping, etc., or both, that consume excited energy.[10] Various examples of AIEgens that can be explained by RIM have been reported, and one of such AIEgens that comprises a vibrating core and rotatable peripheries is 5,12-bis(diphenylmethylene)–5,12-dihydrotetracene (BDPM-DHT) [**3**, Fig. 1(c)].[27] BDPM-DHT is not emissive in dilute THF solution, but shows intense fluorescence at 455 nm in aggregated state, revealing its typical AIE feature. In solution state, the acene backbone vibration and phenyl group rotation consume the excited energy, leading to the domination of non-radiative dissipation of excited state. In crystalline state, BDPM-DHT presents a highly contorted structure, where the diphenylmethyl groups and the tetracene backbone show large dihedral angles with weak conjugation. Such steric repulsion leads to the locking and separation of BDPM-DHT molecules in the crystals, which

blocks the non-radiative decay pathways and makes the BDPM-DHT crystal emissive.

RIM is a simple and fundamental mechanism that explains the AIE phenomenon, and it has been solidly elucidated by both experimental and theoretical works. In a RIM system, the RIR and RIV mechanisms can work independently or together, but all follow one trend: any intramolecular motion can consume energy and enhance non-radiative decay rates of molecules, whereas blocking the non-radiative pathways *via* structural restriction will relax excitons through radiative channels to lead to the AIE effect.

III. AIE SYSTEMS

As discussed in Sec. II, there are two main factors that determine the AIE properties, one is the blocking of the active intramolecular motions, and the other one is to form twisted 3D conformation to reduce the π-π stacking interactions faced by conventional ACQ fluorophores. This provides the guidelines for the design of novel AIE systems as well as strategies to convert ACQ fluorophores to AIEgens. Since the discovery of the AIE phenomenon, lots of work emerged to transform ACQ fluorophores to AIEgens that aim to introduce AIE features, while maintaining the desirable properties of conventional fluorophores. These successful examples have facilitated the rapid exploration of AIE systems with great diversities. In this section, we will introduce the different strategies to convert ACQ to AIE, and the development of different AIE systems including small molecules, macromolecules, and some nonconventional systems.

A. Conversion of ACQ to AIE

Conventional ACQ fluorophores usually exhibit disc-like structures, which form compact packing in solid state with strong π-π stacking interaction, leading to undesired ACQ effects. Various approaches (chemical, physical, and engineering) have been used to mitigate the ACQ effects but more or less introducing undesirable side effects to the properties of fluorophores.[28–30] The discovery of the AIE phenomenon and understanding of the AIE mechanism provide a win-win strategy to mitigate the ACQ effects faced by many conventional fluorophores without harming their original properties. A multitude of works have been reported for ACQ to AIE conversion, which involves the decoration of the ACQ fluorophore cores with AIE moieties, or vice versa, and creating new AIEgens directly from ACQ fluorophores based on the RIM mechanism.

AIEgens themselves are electronically conjugated, and hence it provides the opportunities of linking AIE and ACQ segments together at molecular levels to eliminate ACQ effects without sacrificing the AIE feature of the new fluorophores. One of the most straightforward strategies is to decorate the ACQ fluorophores with AIE moieties to introduce the intramolecular motions as isolated molecules to eliminate solution fluorescence and the twisted 3D structure in aggregate state to enhance the aggregate emission. One of the representative examples to demonstrate such ACQ-to-AIE conversion is the symmetrical decoration of a pyrene core with four TPE peripherals to form the 4TPE-Py (**4**) (Fig. 2).[31] Pyrene is a typical ACQ fluorophore that is commonly used as a blue emitter in OLEDs, which suffers from low emission in solid and film states. **4** emits weak fluorescence in solution but shows largely enhanced emission in solid state. The η of **4** in film state is measured to be up to 70%. In a more in-depth study, different numbers of TPE units have been attached to perylene bisimide (PBI), a flat heteroatomic molecule exhibiting the ACQ property, to study the effects of TPE decoration.[32] Without TPE peripheries, PBI shows an emission peak at 538 nm with a solution η of 95.2%, while its solid film exhibits very weak emission. With two TPE substituents, the resultant 2TPE-PBI (**5**) (Fig. 2) effectively consumes the excited-state energy through the free intramolecular rotation of TPE units, which endows **5** with a η of 0.07% in solution state. In solid state, due to the TPE impairing the π-π stacking interactions and RIR of phenyl rings, **5** displays strong red emission ($\eta = 18.9\%$). On the other hand, with only one TPE periphery, the analogue of **5**, TPE-PBI shows a much higher solution brightness ($\eta = 2.2\%$) and lower solid state emission ($\eta = 9.0\%$) as compared to **5**. Such results clearly reveal the importance of TPE in converting ACQ fluorophores to be AIE active, where a single TPE moiety in TPE-PBI can only consume a portion of the excited-state energy, while the two TPE moieties are able to totally exhaust such exciton energy, resulting in almost diminished emission in solution for **5**.

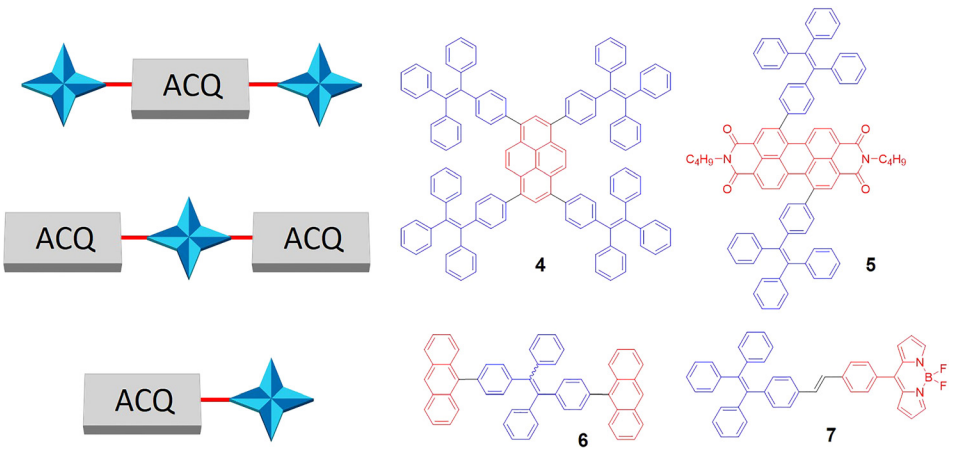

FIG. 2. Schematic illustration of different strategies to convert ACQ fluorophores to AIEgens.

Another strategy for converting ACQ fluorophores to AIEgens is to utilize AIEgen as the core and replace the moieties of AIE archetypes with ACQ units. Anthracene derivatives have been widely applied in OLED applications because of their excellent photoluminescent, electroluminescent (EL), and electrochemical properties.[33] However, the notorious ACQ effect due to the flat anthracene structures always leads to decreased η in solid state. Zhao *et al*. tethered two anthracene moieties to peripheral phenyl rings of the TPE core, and the obtained TPE-2An (**6**) exhibits a typical AIE characteristic (Fig. 2).[34] In THF solution, **6** has a low η of 0.29%, but the η increases to nearly 100% in the film state. The introduction of anthracene does not affect the structural flexibility and twisting instinct of the aryl rings of TPE, which still undergoes free intramolecular rotation in the isolated state to consume the excited-state energy of the whole molecules. At aggregated state, the RIR is activated, and the twisted 3D structure of TPE segments prevents the adjoining anthracene segments from forming π-π stacking interactions, both help to eliminate the emission quenching in the solid state, largely improving the performance of anthracene derivatives in OLED applications.

Directly attaching AIE moiety to ACQ fluorophores without a core-periphery structure can also convert ACQ to AIE. One example is to attach TPE to boron-dipyrromethene (BODIPY) *via* a vinyl bond to yield AIEgen TPE-VB (**7**) (Fig. 2).[35] As BODIPY itself is electron-deficient, integrating with an electron-rich TPE moiety readily generates a donor-acceptor (D-A) system with more photophysical properties, and thus, **7** exhibits both TICT and AIE characteristics. In THF solution, the TICT effect dominates the photophysical properties, **7** shows the TICT emission at 640 nm. When the water fraction in the THF/water mixture is increased to 10%, the TICT emission is completely quenched. The TICT emission quenching is likely due to the solvent polarity effects of the D-A system as well as the consumption of excited-state energy by the free intramolecular motions of the TPE moiety. The emission of **7** is invigorated and intensified when the water fraction is larger than 75%, at which stage **7** forms aggregates and the RIM dominates the photophysical process, indicating that **7** is AIE active.

Besides the illustrated examples *via* conjugation of ACQ fluorophores with AIEgens,[36–38] lots of other works have also successfully converted ACQ fluorophores to AIEgens without introducing AIE elements, which is normally achieved by connecting aromatic ACQ stators and rotors with rotatable single bonds. For example, embellishing quinoline with two rotatable phenyl rings can transfer quinoline to be AIE active, with a solution η of 0.3% and a solid-state η of 3.2%.[39] These converted AIEgens may exhibit varied degrees of emission in solution state if the free intramolecular motions cannot fully consume the excited-state energy. All these molecules have shown largely intensified emission in aggregate state, contributed by joint activities of the twisted 3D structures to impede the strong π-π stacking interactions, and the activation of the RIR effects. In this section, the successful examples of converting ACQ fluorophores to AIEgens have been demonstrated. Although not all fluorophores can be converted to be AIE active, these studies have expounded tremendous synthetic routes of AIEgens, further deepened our mechanistic understanding of AIE, and yielded various classes of AIE systems for different applications.

B. Small molecules

Despite the great diversities of AIEgens, small molecules remain an important class of AIE systems. Compound **8** (Fig. 3) based on aryl ring decorated hexa-1,3,5-trienes core represents one of the typical small molecular AIEgens.[40] **8** is almost not emissive as isolated molecules in chloroform, but is able to intensify its emission in solid state with a η of 25.0%. The central hexa-1,3,5-trienes core of **8** shows an almost planar structure, while the two pairs of phenyl rings form orthogonal conformation as the existing steric repulsion between the hydrogen atom at the *ortho*-position of the phenyl ring and the nearby hydrogen atoms on the central core. With weaker conjugation and larger dihedral angles (82.31° and 99.82°) with the core, the vertical phenyl ring pair can undergo free rotation. The phenyl ring pairs at horizontal position have dihedral angles of 15.16° and 15.77° with the hexa-1,3,5-trienes core, which are also able to twist around the single bonds. Both the rotation and twisting structures contribute to excited-state energy consumption and lead to emission quenching in solution. In aggregate state, the RIR is induced, and the orthogonal conformation of the two phenyl ring pairs impairs the detrimental π-π stacking interactions, both help to turn on the emission. Hexaphenylbenzene (HPB, **9**) (Fig. 3) is an AIEgen constructed from pure aryl rings, where the benzene ring is fully decorated with six phenyl rings.[41] HPB exhibits an aggregation-enhanced emission (AEE) characteristic. It shows weak but detectable emission in THF, and exhibits over 12-fold of fluorescence enhancement in the THF/water mixture at a water fraction of 80%. The crowdedness of the phenyl rings around benzene creates significant steric repulsion between adjoining phenyl rings, which restricts their free rotation to certain degree even at molecular state and leads to the observable emission. In aggregate or crystalline state, the existence of a large amount of C–H…π interactions rigidifies the molecular packing and blocks the phenyl ring motions leading to RIR, together with the propeller shape of HPB that avoids the close π-π stacking interactions; the emission of HPB in solid state is thus intensified.

Another category of AIE small molecules is based on the anthracene core. Two phenyl rings are conjugated to both sides of the anthracene core *via* vinyl bonds, and the obtained 9,10-di[(*E*)-styryl]anthracene (DSA, **10**) (Fig. 3) displays AIE character, which is non-emissive in THF solution, but shows a η of 50.8% in crystal.[42] Similar explanation to HPB can also be found for **10** as revealed by its crystal structure, where the orthogonal styryl arms prevent π-π interactions and the rigidified conformation activates the RIR process. Anthracene can also serve as the rotor for building small AIE molecules. AIEgen **11** was synthesized by linking two anthracyl units to the 1 and 2 positions of the central phenyl core *via* two vinyl bonds (Fig. 3).[43] Due to the steric repulsion of the two anthracyl arms, **11** adopts a twisted

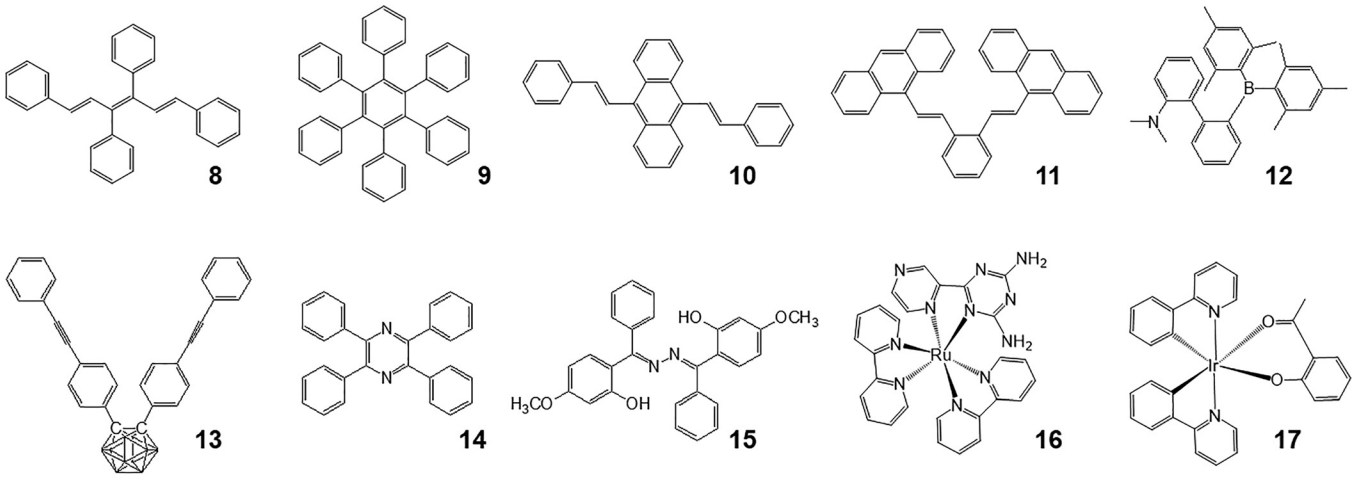

FIG. 3. Examples of AIE small molecules.

structure with the torsion angles ranging from 53.20° to 73.55°, which weakens the electron conjugation of the whole molecules. As a result, the anthracyl arms act as the rotors in isolated state, resulting in almost no fluorescence, and the activation of RIM in solid state leads to a η of 12.0%.

Besides the pure hydrocarbon small molecular AIE system, heteroatom-containing AIEgens have also been developed. Compound **12** (Fig. 3) reported by Zhao *et al.* is one of these examples.[44] Due to the strong intramolecular charge transfer (ICT) effect of N-B interaction, **12** adopts large steric congestion between boronyl and amino groups, showing emission in THF with a η of 27.0%. Benefiting from the twisted structure, **12** shows a η of 86.0% in neat film, clearly indicating its AEE activity. Another example is compound **13** (Fig. 3), which is constructed *via* conjugating two diphenylethynl groups to the 1,2-positions of *o*-carborane.[45] *o*-Carborane is an icosahedral boron cluster compound, which exhibits highly polarizable σ-aromatic characters, and the combination of *o*-carborane and the AIE system can create mutual benefits to both. Due to the active rotation of the aromatic rings, **13** shows negligible emission in THF solution with a $\eta < 0.02\%$. In solid state, the weak conjugation of phenyl leads to the formation of a twisted molecular conformation which prevents the π-π stacking interaction. Together with RIM, **13** shows a raised η of 12.0%. Tang *et al.* also reported a new type of small AIEgen, tetraphenylpyrazine (**14**) (Fig. 3) through a one-pot reaction.[46] The emission of **14** is weak in THF solution, but it shows gradually increased emission in the THF/water mixtures with increasing water fraction, indicative of its AIE properties. Single crystal analysis shows that **14** adopts non-planar conformation and the twisted angles between phenyl arms and pyrazine core range from 33° to 66°. The existence of multiple intramolecular C–H…π interactions with a short distance from 2.82 to 3.18 Å in the crystal packing of **14** also contributes to blocking the intramolecular motion and suppressing the radiationless dissipation pathway, leading to emission tum-on in solid state.

Excited-state intramolecular proton transfer (ESIPT) is an ultra-fast photoautomerization process (at subpicosecond scale) that holds the characters of the intramolecular hydrogen-binding formation with a large Stokes shift.[47] ESIPT properties have been widely adopted in the design of photosensitizers, luminescent materials and molecules, etc. The designs of ESIPT fluorophores with AIE features have shown promising performance of this amalgamation. Compound **15** (Fig. 3) is one of the AIE + ESIPT fluorophores, which emits almost no fluorescence in solution but shows bright emission in aggregates.[48] In molecular state, all kinds of hydrogen bonding in the ESIPT process is inhibited by the active intramolecular rotation around N–N, C–N, or C–N single bonds, so the excited-state energy is effectively dissipated through a non-radiative pathway. In aggregate state, the formation of intramolecular hydrogen bonding and the impaired π-π stacking interaction leads to the radiative decay pathway and bright emission. In addition, the hydrogen-bonding tautomerizes the excited enol state to lower excited keto state at a very fast rate ($k_{ESIPT} > 10^{12}\,s^{-1}$), and the smaller energy gap between keto state and ground state leads to red-shifted emission, and hence, **15** exhibits a large Stokes shift of 152 nm in aggregate state.

Transition metal based small molecular AIE systems have also drawn enormous interest. One of the examples is the Ru(II) polypyridyl complex. Through the coordination of the central Ru(II) with two bipyridine and one pyrazinly moieties, the obtained **16** (Fig. 3) displays a distorted octahedral sphere.[49] **16** shows a weak fluorescence centered at 613 nm in diluted acetonitrile solution upon excitation at 441 nm with a low η of 0.1%. Addition of toluene leads to an aggregate formation and enhanced red emission (at a toluene fraction of 90%), indicative of its AIE activity. It should be noted that the vibration of bipyridine and pyrazinyl triazine diamine ligands contributed to the excited-state energy consumption in isolated state, as their active rotation is blocked by the coordination between these ligands and the Ru(II) core. Another example of AIE-active transitional metal complexes is AIE-Ir(III) (**17**) (Fig. 3),[50] where the Ir(III) core is decorated with 2-phenylpyridine ligands. Similar to **16**, the vibrational motions rather than the rotational motions of these ligands consume the excited-state energy, and **17** shows hardly detectable emission with a $\eta < 0.1\%$ in isolated

state. In crystals, both the weak and angled π-π interactions between 2-penylpyridine arms and the strong C–H…π interactions work together to activate RIV of **17**, leading to intensified emission in solid state with a η of 4.3%.

Attaching simple rotatory ligands to linear, cyclic organic molecules or transition metal complexes can readily generate AIE-active fluorophores without hampering the useful and original functions of these cores. AIE systems have been proved to be highly compatible with various molecular systems and luminescence processes. AIE ligands as electron accepting or donating units can be easily introduced to combine the TICT with AIE properties in the molecular systems to fine tune the emission wavelengths that are desirable for different applications. With the rapid advances of the AIE world, more and more small AIE molecules have been developed, and these highlighted examples in this section aim to show the large variety and infinite possibility of AIEgens.

C. Macromolecules

Great progress has also been made for the development of macromolecular AIE systems.[13] As compared to small molecular AIEgens, the macromolecular AIEgens display several advantages. The molecular structures, morphology, and topology can be easily tuned for macromolecular AIEgens, which is hardly achieved in small molecular AIE systems. In addition, these macromolecular AIEgens usually exhibit excellent mechanical strengths as a result of the multiple covalent-bonded repeating units. AIE-moieties can be introduced into the backbones or side chains of AIE polymers, or to be incorporated into metal-organic frameworks (MOFs) to realized AIE-active macromolecules. In this section, several emblematic examples of AIE macromolecules will be elucidated.

One of the most common and straightforward strategies for developing AIE macromolecules is to incorporate typical AIEgens such as TPE or HPS as the monomers into the backbones of the polymeric structures. Compound **18** (Fig. 4) is a pure TPE-based fully conjugated polymer synthesized through the Suzuki coupling reaction by joining TPE units together.[51] **18** shows weak emission in THF solution with a η of 1.2%, while it displays high fluorescence enhancement with a η of 28.0% when it forms aggregates in the water/THF mixture at high water fractions. Due to the extended conjugation length and a more planar structure, **18** exhibits longer emission wavelength in solid state (centered at 506 nm) as compared to its TPE monomer (centered at 470 nm). The AIE feature of **18** should be contributed to its TPE monomer. In most cases, conjugated polymers suffer from fluorescence quenching in solid state due to the multiple π-π interactions. The highly twisted TPE conformation has prevented π-π stacking interactions, and endows the pure TPE polymer **18** with bright emission in solid state. Besides building the backbones with AIEgens, the macromolecular system has shown great varieties, where AIEgens can serve as the side chains of macromolecules. Poly[(2-(4-vinylphenyl)ethene-1,1,2-triyl)tribenzene] (PTPEE, **19**) (Fig. 4) is one of such AIE polymers.[52] **19** is synthesized through reversible addition-fragmentation chain transfer (RAFT) polymerization, which helps to control the number of AIE

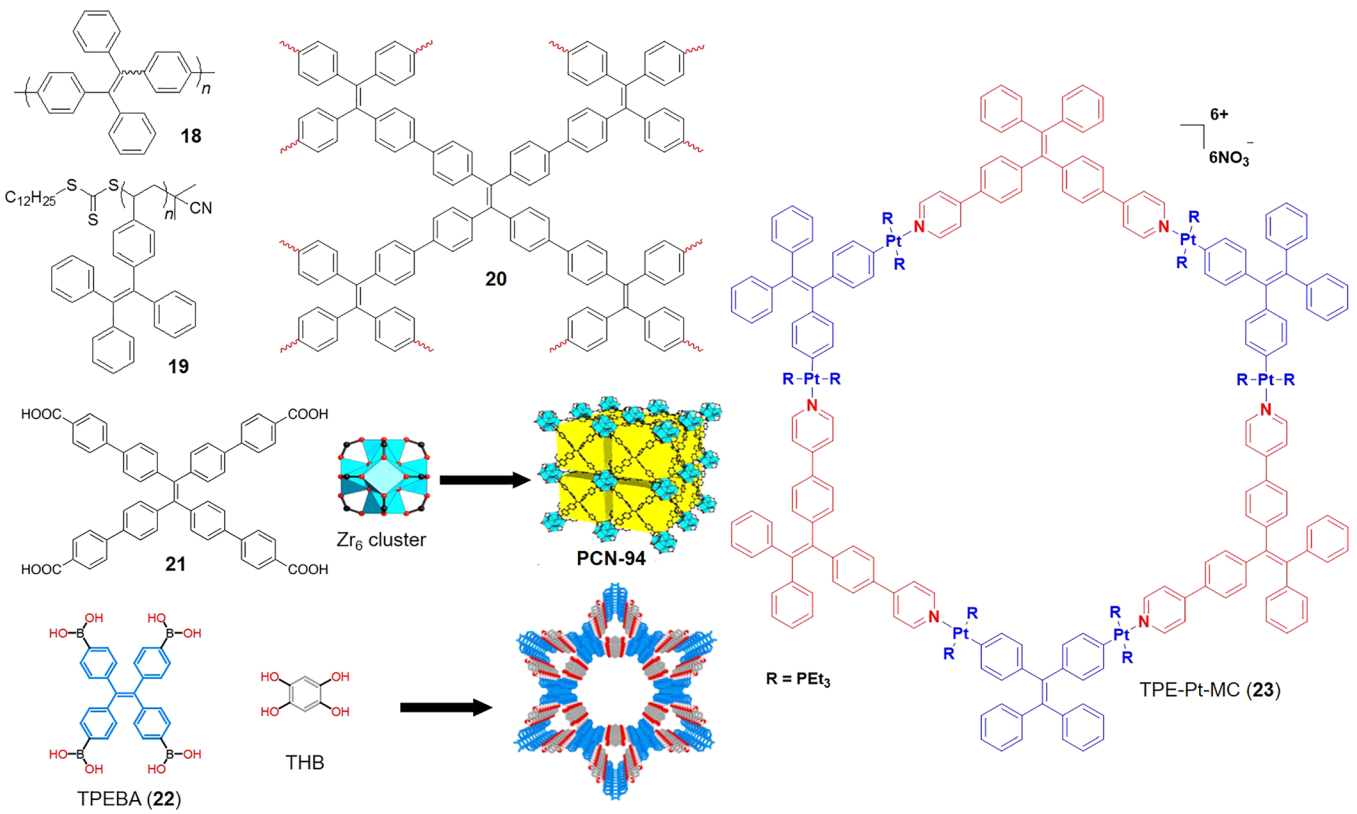

FIG. 4. Examples of AIE macromolecules. Reproduced with permission from Wei *et al.*, J. Am. Chem. Soc. **136**, 8269 (2014) and Dalapati *et al.*, J. Am. Chem. Soc. **138**, 5797 (2016). Copyright 2014 and 2016 American Chemical Society.

side chains in the resultant polymer. All the derivatives of **19**, with different repeating units and molecular weights, emit no fluorescence in THF solution, while their emission is intensified in THF/water mixtures with high water fractions. It is noted that **19** displays higher aggregated state η when the polymer chain is longer. This is attributed to the increased hydrophobicity and decreased solubility of longer chain polymers, which forms larger nanoaggregates with more tight packing and constrained RIM. TPE is a versatile building block, which can also be used for constructing fully conjugated microporous polymers with confined architectures. Jiang *et al*. reported compound **20** (Fig. 4) with highly ordered hyperbranched networks through the Yamamoto coupling reaction.[53] **20** possesses an interlocked network structure, which can sufficiently block the phenyl ring rotations even in the isolated state when molecules dissolved in different solvents. As such, **20** exhibits bright fluorescence with red-shifted emission of 551 nm and a η of 40.0%. Nitrogen sorption isotherm measurement at 77 K reveals its high surface area up to 1665 $m^2\ g^{-1}$ and the presence of micropores with a size of about 0.8 nm. This interweaving scaffold could effectively interlock the rotation of these TPE units by covalent bonds from all four directions, which provided validation of the RIM mechanism from a different perspective.

MOFs that comprise inorganic metal-containing nodes and organic linkers with large internal surface rears and diverse structures have shown promising performance in catalysts, OLEDs, and luminescent sensors.[54] The incorporation of AIEgens especially TPE derivatives is able to generate MOFs with intrinsic luminescence. One of the AIEgens that has been used for MOF construction is **21** (Fig. 4).[55] The AIE-active **21** displays bright yellow fluorescence centered at 545 nm with a η of 30.0% in solid state. The corresponding MOF **PCN-94** with a porous and robust structure is built by the crystallization of **21** with Zr(IV). **PCN-94** adopts a 3,3,3,12-c net, where the Zr_6 cluster serves as a 12-connected node and **21** acts as 3,3-connected nodes. The crystal structure reveals that each Zr_6 cluster is connected to 18 other Zr_6 clusters through 12 units of **21**. The strong coordination with the Zr_6 cluster immobilizes the free rotation of **21**, and hence, the rigid **PCN-94** exhibits a largely improved η nearly unity (100%). **PCN-94** exhibits a blue shifted emission (centered at 470 nm) as compared to **21**. The blue shifted emission is caused by the breakdown of the delocalized conjugation system in **PCN-94** by the more nonplanar conformation as compared to **21** itself, which widens the HOMO and LUMO energy gap.

AIEgens have also been used for construction of covalent organic frameworks (COFs). COFs are crystalline porous polymers that can integrate organic units into periodic columnar π-arrays and inherent pores, making them valuable in different applications. Through the solvothermal condensation of the TPE-cored boronic acids (TPEBA, **22**) (Fig. 4) and 1,2,4,5-tetrahydroxybenzene (THB) in the mixture of dioxane/mesitylene, Jiang *et al*. reported the highly emissive two-dimensional COF (TPE-Ph).[56] The obtained TPE-Ph COF shows rectangular belt shapes, and its size increases with reaction time. TPE-Ph COF contains a dual-pore Kagome lattice with trigonal micropores and hexagonal mesopores. TPE units at the vertices and the phenyl linkers at the edges of the polygons form periodic columnar TPE π-arrays. Nitrogen sorption measurement at 77 K gives a combination of micropores and mesopores in TPE-Ph COF, with a Brunauer-Emmett-Teller (BET) surface area of 963 $m^2\ g^{-1}$ and pore sizes of 1.3 and 2.6 nm. The TPE-Ph COF solid sample shows a higher η of 32.0% as compared to **22** ($\eta = 15.0\%$), which suggests that the π-π interactions among different layers of COF further restrict the rotation of the four phenyl rings and rigidify the TPE structure.

Besides the above mentioned MOF and COF, Stang *et al*. recently also reported another type of organic-inorganic hybrid AIE macromolecule, namely, TPE-based discrete organoplatinum(II) metallacycle (TPE-Pt-MC, **23**) (Fig. 4).[57] Some of these hybrid molecules have shown unique bright luminescence in both solution and aggregated states. Taking **23** as an example, the 2D structured **23** has a ca. 4.0 × 6.0 nm cavity and six positive charges, which is able to form a 3D biohybrid complex through the hierarchical self-assemble with 1D rod-like tobacco mosaic virus (TMV) with turn-on fluorescence. The TMV rod has a dimension of 300 × 18 nm and a cavity of 4.0 nm has been widely used for development of novel functional materials,[58,59] and this fluorescence turn-on provides a direct observation of hierarchical assembly and disassembly of individual virus. In water/dimethyl sulfoxide (DMSO) (3/7, v/v) solution, **23** has an absorption band at around 334 nm in dichloromethane with a molar absorptivity of $1.48 \times 10^5\ M^{-1}\ cm^{-1}$ and exhibits a very weak fluorescence centered at 490 nm. The formation of the 3D biohybrid complex is achieved by simply mixing the TMV aqueous solution with the **23** DMSO solution, which is evidenced by the morphology of TMV changes from discrete rod-like shape to network-like ones with several micrometers. Due to the electrostatic interaction between TMV and **23**, the absorption of the formed biohybrid complex slightly shifted to 331 nm with a decreased ε of $1.28 \times 10^5\ M^{-1}\ cm^{-1}$. The hierarchical self-assembly between TMV and **23** forms tight and well-ordered arrays, which rigidify the twisted TPE moieties in the confined environment, leading to large fluorescence enhancement. In addition, the emission intensity of **23** shows a linear increase with TMV in a concentration range of 0–0.6 mg/ml, with a fluorescence enhancement factor of 5.41-fold observed at TMV and **23** concentrations of 0.6 mg/ml and 10 μM, respectively. The bright emission provides the opportunities for direct visualization of the self-assembly processes and the morphology change of the hybrid materials.

D. Nonconventional AIE systems

For most of the organic fluorophores, they have to possess enough electron conjugation to be luminescent. For example, in THBA (Fig. 1), the phenyl rings and the vinyl rods are connected through single bonds to obtain large π-conjugated systems to realize its fluorescence. However, there were increasing reports of fluorophores that do not require through-bond conjugation but still display the AIE phenomenon. Compound **24** [Fig. 5(a)] is one of such

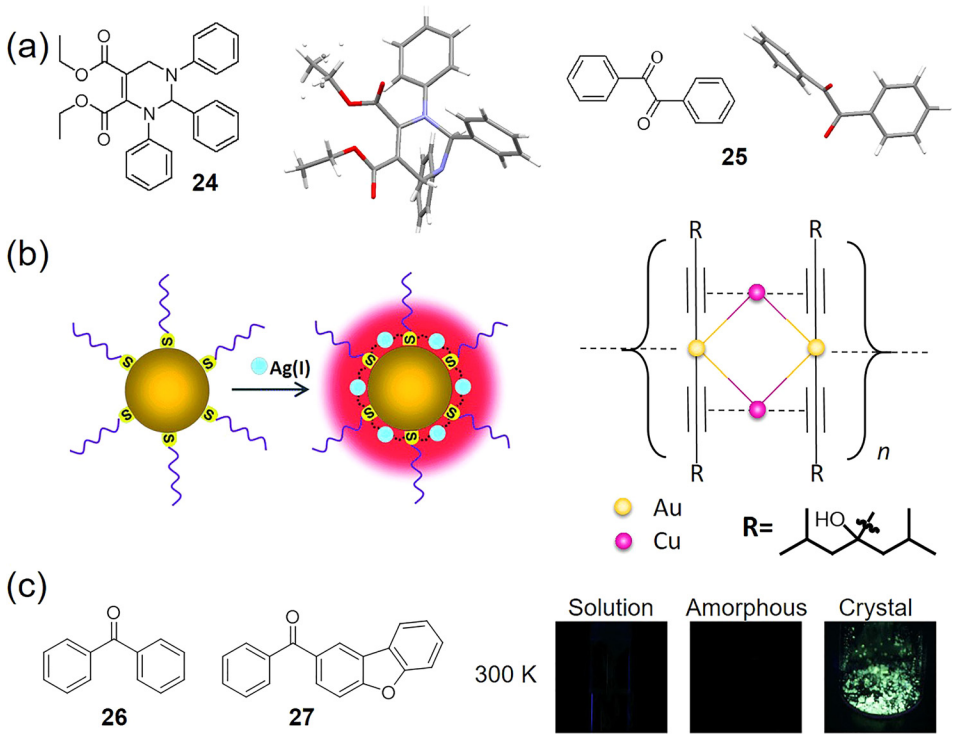

FIG. 5. Examples of nonconventional AIE systems. (a) Represented unorthodox AIE molecules *via* through-space electronic conjugation. (b) Light up thiolated Au@Ag nanoclusters. Reproduced with permission from Dou *et al.*, Nanoscale **6**, 157 (2014). Copyright 2014 Royal Society of Chemistry. (c) Room temperature phosphorescent (RTP) AIE molecules. Reproduced with permission from Zhao *et al.*, Chem **1**, 592 (2016). Copyright 2016 Elsevier Inc.

fluorophores.[60] As a simple molecule, **24** only has one of the carbonyl π systems extended to the π cloud of the C=C double bond, and such a weak through-bond π conjugation can hardly realize emission. **24** emits no fluorescence in solution but shows bright emission in crystals with a η over 50%. The crystal structure analysis helps to reveal the reason of their bright emission in crystals: the lone-pairs between heteroatoms, e.g., oxygen and nitrogen, are in close proximity in crystal state. The distances between O–O, O–N, and N–N are all very short around or less than 3 Å, which form electronic interactions through space. This existence of multiple and strong through-space electronic interactions actually provides largely enough electronic conjugation when their structures are rigidified. Furthermore, the presence of interactions between C–H…O, C–H…N, and C–H…π in crystalline state also restricts the active intramolecular motions, and thus, **24** gives bright emission in crystals. In solution, the active rotation of aryl and ester units and vibration of tetrahydropyrimidine rings not only consume the excited-state energy, but also possibly separate the through-space electronic conjugation between these heteroatoms, which leads to very weak fluorescence of **24** in solution. Another example of such nonconventional AIE molecules is **25** [Fig. 5(a)].[61] **25** is a TPE derivative with a folded conformation, where two phenyl rings and vinyl rod are organized into a large π-electronic conjugation through single bonds. **25** is almost not emissive in polar and nonpolar solvents, such as THF, hexane, toluene, and acetonitrile, at normal temperature, as it has a highly twisted conformation and can actively rotate. But when these solutions are frozen at low temperature of 77 K or **25** is in crystal form, bright green fluorescence can be observed. It implies that the specific molecular motions are locked or impeded by ordered molecular packing as well intermolecular interactions. Crystal structure analysis further provides insight into the turn on process. As crystal, eight intermolecular C–H…O hydrogen bonds exist between molecules of **25** and six surrounding cousins with a short distance (2.416, 2.417, 2.482, 2.483 Å). These intermolecular interactions fully lock molecular rotation of phenyl rings and carboxyl groups. In addition, this unique structure of **25** in crystalline state also generates an electronic delocalization system through space π-conjugation. Both the through bond and through space electronic conjugations work together to afford **25** with the AIE feature.

Besides these high luminescent AIE systems based on organic molecules, AIE active metal clusters have also been reported. Xie *et al.* developed the AIE active Au@Ag nanoclusters (NCs) [Fig. 5(b)] with bright luminescence.[62] The mono-metallic cluster, glutathione (GSH)-protected Au NCs show very weak fluorescence at an emission wavelength of 800 nm in aqueous solution with a η of 0.37%. The addition of Ag(I) ions into the Au NCs can generate Au@Ag NCs, as observed by the change of solution color from greenish brown to brown. The Au@Ag NCs show light-up red fluorescence with an increased η of 6.8%. Au@Ag NCs have a lifetime of 2.21 μs, indicating that the emission of Au@Ag NCs actually is phosphorescence, which is generated from the complexation of Au(I) and Ag(I). At isolated state, Au NCs hold long lifetime and excited state, which provide sufficient time for excited-state energy consumption by the active vibration of the GSH arms, leading to weak fluorescence. The complexed Ag(I) on Au@Ag NCs provides multiple interactions with GSH arms through the functions such as carboxyl, carbonyl, and amine groups. These interactions form a grid network around the whole Au@Ag NCs, which restricts the GSH arm vibrations, and such activation of RIV leads to radiative relaxation of excitons with enhanced phosphorescence. The design of metal clusters or complexes

provides a simple approach for developing light-emitting materials with strong fluorescence or phosphorescence. The demonstration of decoration metal centers to provide luminescence has further proven the genericity of AIE mechanisms for realizing strong emission in solid state *via* blocking the excited-state energy consumption through RIM. Moreover, the AIE mechanism is more significant in phosphorescent materials, where phosphorescence is more susceptible to non-radiative quenching due to the prolonged lifetime originated from intersystem crossing (ISC) to the triplet excited state.

Phosphorescence, especially room temperature phosphorescence (RTP), has attracted extensive attention in wide applications, ranging from electronics to optics and biological science.[63] However, due to the sensitive response of the excited triplet state emission to temperature and oxygen as well as the inefficient ISC caused by weak spin-orbit coupling and fast non-radiative decay, RTP from pure organic molecules has been very limited. Recently, RTP from pure organic fluorophores has been achieved with the help of AIEgens. **26** [Fig. 5(c)] represents one of the simplest small AIE molecules with RTP.[64] **26** in solution is transparent and exhibits no emission upon excitation at room temperature, but it shows high phosphorescence under UV irradiation when being cooled to 77 K. In addition, the amorphous solid of **26** is not emissive but its crystalline state gives blue emission even at room temperature, with phosphorescence peaks centered at 420, 449, and 483 nm. Moreover, **26** crystal has a mean lifetime (τ) of $\sim$316.5 μs with three relaxation pathways, indicating that the phosphorescence originates from the radiative decay of triplet excited states. In addition, the molecular packing in crystals reveals that the multiple C–H…O hydrogen bonds between two benzene rings of two adjacent **26** molecules over the whole crystal structure help to rigidify the molecular conformations, leading to efficient RTP. Very recently, Tang *et al*. also reported how to achieve persistent and efficient RTP for four organic fluorophores.[65] 1-(Dibenzo[b,d]furan-2-yl)phenylmethanone (**27**) is one of the typical examples. **27** is not emissive in solution or amorphous state, but its crystalline powders emit intense green emission at room temperature under 365 nm UV irradiation [Fig. 5(c)]. In addition, the phosphorescence spectra are nearly identical measured in air and in an inert atmosphere, indicating that rigidification of intramolecular motions by crystallization is an effective approach to realize RTP by blocking the emission quenching from oxygen contacting or other non-radiative decay pathways. The τ of **27** is 0.23 s with a phosphorescence quantum yield of 34.5% at 300 K in ambient conditions. These examples clearly reveal that introducing AIE into phosphorescence compounds is an efficient approach to achieve persistent and efficient pure organic RTP.

IV. TECHNOLOGICAL APPLICATIONS

Great research interests have been attracted to AIE, since the concept was first coined in 2001. Along with the diversities of AIEgens developed, enormous AIE materials have been implemented in various applications that involve light emitting or RIM processes, which also have inspired the great innovations in plentiful techniques. AIEgens as bright solid emitters have been promising in the fabrication of high performance optoelectronic devices. The unique fashion of AIEgen fluorescence turn-on processes has shown great possibilities for the development of new sensing and detection systems with high signal to noise ratios. In this section, we discuss the various applications for AIEgens, with main focus on the emerging new applications reported since 2013.

A. Optoelectronic devices

Optoelectronics is one of the cutting-edge research areas, which has played indispensable roles in our daily lives. As the core components of the optoelectronic technique, these optical-to-electrical or electrical-to-optical transducers and other optoelectronic devices require luminescent materials to be fabricated in solid state with promising performance. As bright solid emitters with excellent photostability and thermal stability, AIEgens represent one of the most promising optical materials for optoelectronic devices and applications, such as OLEDs, OFETs, optical waveguides, etc.

1. OLEDs

As the key components of novel display devices, OLEDs have recently attracted great attention. Thanks to the great solid state performance of AIEgens, AIE-based OLEDs with primary RGB (red, green, and blue) colors and promising performance have been developed, and in this subsection, we will illustrate the excellent performance of AIEgens in fabrication of OLEDs with different emitting colors.

Among solid state emitters, the design of deep blue emissive fluorogens is crucial for the full color OLED displays. One of the main problems is the wide bandgap of blue emitters and the associated large driving voltage and low device efficiency due to their large and unbalanced charge injections. In 2015, We reported a deep blue emitting AIEgen to overcome these problems.[66] This new AIEgen, **28** (Fig. 6), is designed by conjugating two triphenylethene groups onto a deep blue building block of phenanthro[9,10-d]imidazole. **28** has absorption and emission maxima centered at 340 nm and 449 nm in THF, respectively. In addition, the insensitivity of **28** emission in response to solvent polarity changes makes it ideal for improved charge balance in OLEDs, as indicated by only 6 nm red-shift upon changing the solvent from nonpolar toluene to polar *N*,*N*-dimethylformamide. Upon increasing the water fraction in the THF/water mixture, **28** shows largely intensified fluorescence with an enhancement factor of 5-fold, indicating that it is AIE-active. Moreover, the thin film of **28** has a η up to $\sim$93.8%, and **28** has HOMO and LUMO levels of -5.50 eV and -2.45 eV, respectively. Such a high solid emission and good carrier injection property make it a promising candidate for electroluminescent (EL) device with a simple configuration. A non-doped OLED device with a configuration structure of indium tin oxide (ITO)/NPB (60 nm)/**28** (20 nm)/TPBi (40 nm)/LiF (1 nm)/Al (100 nm) was fabricated, where NPB ([*N*,*N*′-di(1-naphthyl)-*N*,*N*′-

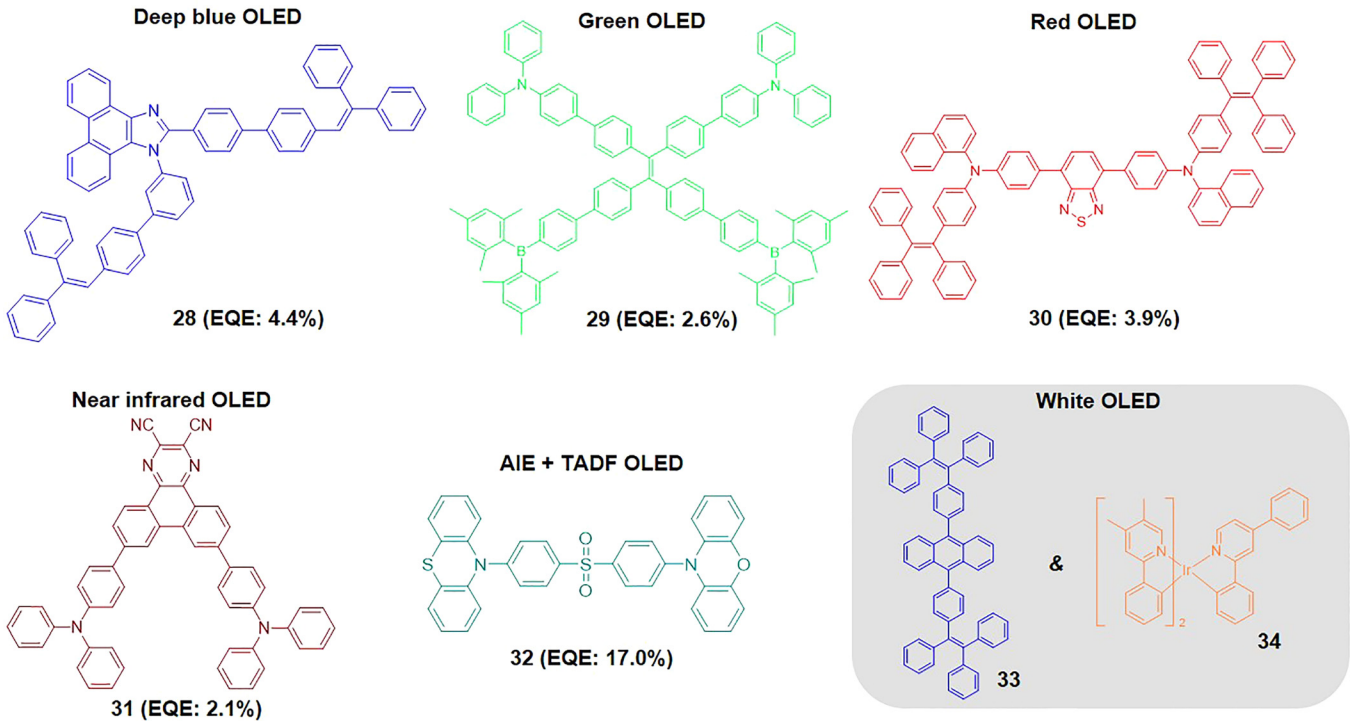

FIG. 6. Representative AIEgens for OLED applications.

diphenyl-(1,1′-biphenyl)-4,4′-diamine]) functioned as a hole-transporting layer, TPBi ([1,3,5-tri(phenyl-2-benzimidazolyl)-benzene]) served as both the electron-transporting layer (ETL) and hole-blocking layer. The fabricated device displays good EL performance, where it can turn on at a very low bias voltage of 3.2 V with a maximum bright blue luminescence up to 20 300 cd/m^2, a maximum current efficiency (CE) of 5.9 cd/A, and a power efficiency (PE) of 5.9 lm/W, respectively. The device has a very high external quantum efficiency (EQE) up to 4.4% (close to the theoretical limit of 5.0%). The device also has a very small roll-off of 14.4% when the brightness increased from 1000 cd/m^2 to 5000 cd/m^2. Such excellent deep blue EL performance of **28** further makes it possible to develop white light OLEDs with International Commission on Illumination (CIE) coordinates of (0.33, 0.33).[66]

With the increased diversity of AIE family, it becomes possible to fabricate OLEDs through a solution-processable manner with defined structures, much improved efficiency and reduced production cost as compared to the conventional vacuum vapor deposition method.[67] AIEgen **29** (Fig. 6) with a star-shaped structure is one of such solution-processable AIEgens for green OLED fabrication.[68] **29** shows absorption and emission maxima at 350 and 526 nm in THF, respectively, with a low η of 2.8%. The fluorescence of **29** is greatly intensified in solid film state as wells as in aggregates with a η up to 95%, indicating its AIE characteristics. Thermogravimetric analysis (TGA) and differential scanning calorimetry (DSC) results revealed the excellent thermal stabilities of **29**, enabling it to function reliably as active layers in OLEDs. A representative solution-processed non-doped green OLED was then fabricated based on **29** as the light emitting layer. The OLED exhibits excellent EL performance, with a low turn-on voltage of 3.4 V. The maximum luminance of the green OLED is up to 11 665 cd/m^2, with the maximum current, EQE, and current efficiency of 8.3 cd/A, 2.6% and 7.5 lm/W, respectively.

As an indispensable element for full-color OLEDs, the lack of red emissive organic fluorogens with high brightness and excellent thermal abilities has been limiting the development of red OLEDs. D-A conformation and extended π-conjugation have been the major approaches for design of red fluorogens, which often suffer from ACQ effects. In this regard, the advances of AIE families offered a unique solution to red OLEDs. AIEgen **30** (Fig. 6) reported by Tang *et al.* in 2015 demonstrated an excellent example of AIEgens for high performance red emissive OLEDs.[69] **30** exhibits both ICT and AIE characteristics, where its emission maximum red shifts along with the increased solvent polarity, and it shows a high solid state η of 63.0%. **30** is a thermally stable AIEgen with a glass transition temperature up to 169 °C, which is much higher than that of commercial red-doped OLED materials (~98 °C). The EL device with **30** as the emitting layer shows a turn-on voltage of 3.2 V with an emission maximum around 604 nm. Luminance of the device is as high as 16 396 cd/m^2, and the maximum current, EQE, and current efficiency were measured to be 7.5 cd/A, 3.9%, and 7.3 lm/W, respectively, which demonstrated an impressive EL performance over previous literature.

Due to the great potential in optical communication and night-vision devices, OLEDs with near infrared (NIR) emission have attracted increasing research attention in recent years. However, the η of emitting materials tends to decrease along with increased emission wavelength, and it is further diminished in solid state due to ACQ effects, which has led

to low EQE for most NIR OLEDs (<1%). In 2015, Wang *et al*. introduced AIE to NIR OLEDs and reported a high EQE of 2.1% for non-doped OLED devices.[70] The NIR emitter, **31** (Fig. 6), adopts a V-shaped D-π-A-π-D structure, where 2,3-dicyanopyrazino phenanthrene (DCPP) serves as the centered acceptor, and diphenylamine (DPA) acts as the electron donor. Due to the structure associated ICT effect, **31** shows an emission peak at 504 nm in hexane, but a largely red-shifted emission peak centered at 810 nm in dichloromethane. **31** has very weak fluorescence in THF solution but becomes highly emissive in solid state with an emission peak centered at 708 nm, and its neat film exhibits a high η of 14.0%. The characteristic AIE effect should originate from the activation of RIM and the highly twisted conformation of **31** in solid state, which makes it an excellent emitting material for OLEDs. Using **31** as the emitting layer, the fabricated non-doped EL device shows an emission maximum at 710 nm with a CIE coordinate of (0.70, 0.29). The NIR OLED shows a luminance brightness of 591 cd/m^2, which represents the highest EQE value among the reported non-doped NIR OLEDs with similar emission spectra.

Thermally activated delayed fluorescence (TADF) materials are exciting discoveries for OLEDs, as all the excitons from phosphorescent emitters can be contributed to the EL process.[71,72] To achieve efficient TADF, the energy gap (ΔE_{ST}) between singlet (S_1) and triplet (T_1) states should be minimized, which is largely achieved through introduction of the D-A system but often accompanied by quenched emission in solid state. The design of AIE TADF emitters ideally can solve this problem, and the compound of **32** (Fig. 6) is one of the representatives.[73] **32** is AIE-active as confirmed by a high η up to 80.0% in film state as compared to the negligible fluorescence in THF solution. Both the activation of RIR of phenothiazine and phenoxazine rings, and the steric hindrance between hydrogen of the diphenylsulfone core and hydrogen of phenothiazine and phenoxazine contribute to the AIE characteristics. The ΔE_{ST} for **32** is ∼0.09 eV, and the delay fluorescence lifetime is 6.2 μs. The corresponding non-doped EL device shows a high EQE of 17.0%, which is contributed by the TADF effect, while AIE maintains the high EQE in non-doped devices. Compound **31** with a small ΔE_{ST} of 0.13 eV also exhibits the TADF effect, where its delayed fluorescence decay is 0.76 μs.[70] When **31** is doped in the TPBi film with 10 wt. %, the delay fluorescence shows a prolonged lifetime of 86.2 μs and a high η of 50.0% with the emission centered at 645 nm. Using the doped films as the EL layers, a high EQE of 9.6% was achieved, indicating nearly 100% triplet harvesting for the EL device.

With the rapid emergence of AIE in the OLED field, large numbers of AIEgens have been reported for OLEDs. Especially with the development of deep blue AIE OLEDs, it becomes possible to build high color rendering index white OLEDs (WOLEDs). To achieve the WOLEDs with efficient performance, Tang *et al*. reported the AIE emitter, 9,10-bis[4-(1,2,2-triphenylvinyl)phenyl]anthracene (BTPEAn, **33**) (Fig. 6) for building deep blue OLEDs and WOLEDs.[74] The deep blue OLED has a configuration of indium tin oxide (ITO)/1,4,5,8,9,11-hexaazatriphenylene hexacarbonitrile (HAT-CN)/NPB/**33**/ETL/LiF/Al. When using bis[2-(2-hydroxyphenyl)-pyridine] beryllium ($Bepp_2$) as the ETL, the obtained blue OLED shows a very low turn-on voltage of 2.75, 3.15, and 4.05 V at a luminance of 1, 100, and 1000 cd/m^2, respectively, with a maximum luminance up to 17 221 cd/m^2. **33** based deep blue OLED displays maximum forward-viewing power efficiency (PE) of 4.3 lm/W, and its value is around 3.6 lm/W at a luminance of 1000 cd/m^2, indicating the low efficiency roll-off. Galvanized by its excellent performance in blue OLEDs, **33** is applied to build high performance WOLEDs with the incorporation of yellow phosphor $Ir(dmppy)_2(dpp)$ (**34**) (Fig. 6). The mixture of NPB/$Bepp_2$/**34** served as the phosphorescent layer to reduce the phosphorescence annihilation and quenching to guarantee the yellow emission. An interlayer was also introduced between blue **33** and the yellow NPB/$Bepp_2$/**34** layers to inhibit the Dexter energy transfer and Forster energy transfer. The maximum forward-viewing PE and current efficiency (CE) for the WOLED are 18.8 lm/W and 19.0 cd/A, respectively. The maximum total PE is up to 32.0 lm/W which is much higher than incandescent lamps (12–17 lm/W). The obtained WOLED displays a very stable pure-white emission close to white equivalent point of (0.33, 0.33) under different luminance conditions. Very recently, Chi *et al*. reported a white emissive TADF AIEgen with CIE white-emission coordinates (0.33, 0.33), which further reveals the great opportunities of development of WOLEDs with a single AIEgen as the white light emitting layer.[75]

Benefited from the excellent emission in solid state of these AIEgens, the introduction of AIEgens to OLED configurations has realized full-color display and WOLEDs with high efficiencies. Besides the illustrated examples, various AIEgens have been used for OLED applications with satisfactory results. It should also be noted that the devices have not yet been optimized thoroughly; thus, there is large room for further development and improvement, especially for red emissive AIE solid emitters.

2. OFETs

OFETs have recently attracted great interest to realize low-cost and large area electronics.[76] Along with the flow of current through the transistor, OFETs can use current to modulate the light emission, enabling the fabrication of full color and flexible displays. Considering the excellent emission of AIEgens in solid state, they are expected to be promising in OFETs. In 2016, Ma and coworkers developed an AIEgen **35** [Fig. 7(a)] by introducing cyano groups to a typical ACQ dyetrans-1,4-distyrylbenzene (trans-DSB) and demonstrated the great potential of AIE in OFETs.[77] **35** is a typical AIEgen, which emits weak fluorescence in dilute solution, but can be induced to be highly emissive in aggregate and crystalline states. Its slice-like single crystal shows green emission around 520 nm with a η of 75.0%. The **35** single crystal is further applied to fabricate OFETs with calcium (Ca)/gold (Au) asymmetric electrode geometry [Fig. 7(b)]. In this asymmetric Ca-Au OFET configuration, the Ca has a very close work function of −2.87 eV to the LUMO level of **35** (−3.26 eV), which is able to reduce the accumulated threshold voltage to be less than 20 V as compared to OFETs with a symmetric Au-Au electrode system (30 V). Such a good energy match also affords the asymmetric

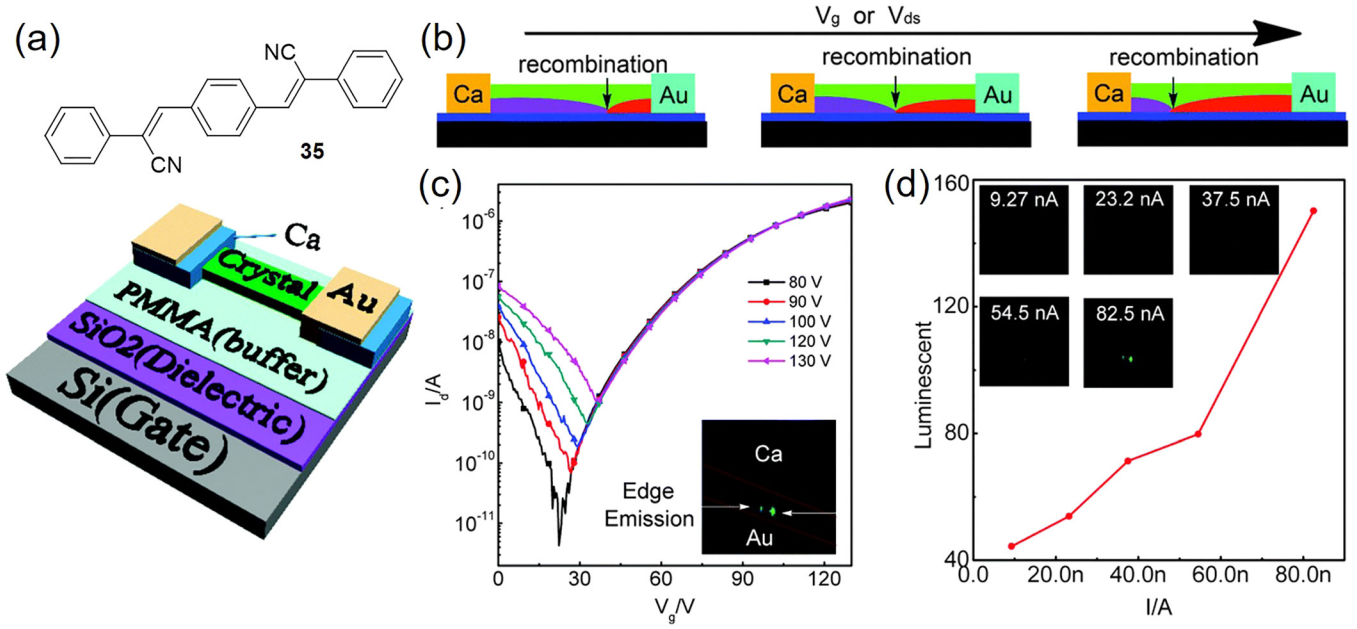

FIG. 7. (a) Structure of **35**, and schematic representation of the **35** based single-crystal device. (b) Schematic diagram of the recombination zone's shift when the V_g or V_{ds} increase. (c) $I_d - V_g$ characteristic of OFET devices with Ca-Au asymmetric electrodes during the electroluminescence test. Inset: the light mission in the device channel at $V_{ds} = 130$ V. (d) Emission brightness of the OFET device, derived from the captured images when the device worked under different I_d. Reproduced with permission from Deng *et al.*, Chem. Commun. **52**, 2370 (2016). Copyright 2016 Royal Society of Chemistry.

OFET with a very high maximum current density to 200 A/cm^2 as well as an improved highest electron and hole motilities to 2.50 and 2.10 cm^2 V^{-1} s^{-1}, respectively. When applying positive gate voltage (V_g) at relatively high source-drain voltage (V_{ds}) (e.g., 40 V), both the opposite carriers are accumulated within the channel which induces the p-n junction and leads to the recombination of the electron and holes [Figs. 7(b) and 7(c)]. Along with the increased V_d, the recombination zone moves forward towards source electrodes. In this ambipolar OFET, the surface of the crystal displays no emission, while its side edge provides bright green and the electroluminescence increases with the increased drain current (I_d) [Fig. 7(d)]. With this demonstration, we can conclude that AIE active materials not only exhibit high solid or crystal luminescence, but also show high mobility. We therefore foresee great potential of the AIE materials in OFETs and the flexible and all plastic electronics.

3. Organic photovoltaic cells (OPVs)

Solar cells that convert sun light energy into electric powers have become the third largest renewable energy sources. Among various types of photovoltaics, organic photovoltaic cells (OPVs) represent one of the most promising alternatives for traditional environmental-harmful fossil fuel combustion ways.[78] To achieve high performance OPVs, two major requirements have to be met, namely, small domain sizes and sufficient electron mobility. However, traditional small organic molecule acceptors tend to form large crystalline domains due to their large planar structures. Introducing twisted confirmation with a bulky bridging unit to these small molecules could help prevent the aggregate formation, but they commonly exhibit a low electron mobility of 10^{-5} to 10^{-4} cm^2 V^{-2} s^{-1}. In addition, these common small molecule acceptors hardly adopt 3D ball-shaped conformations to facilitate the 3D charge-transporting networks as like fullerene derivatives, the best-performance OPV to date. The high electron mobility and unique 3D twisted structures of AIE active materials appear to be the ideal small molecule candidates to replace fullerenes. Yan *et al.* reported one of such AIE active materials for OPVs with a high power-conversion efficiency (PCE) of 5.53% in 2015.[79] The AIE active small molecule, **36** (Fig. 8), was synthesized by connecting four perylenediimide (PDI) units to the centered TPE core. From density functional theory (DFT) calculation, all 3 possible locally optimal confirmations of **36** adopt 3D molecular structures. **36** exhibits excellent solubility in common organic solvents such as THF, chloroform, and hexane, which makes it possible to form very smooth thin films by the solution processed approach. For high performance OPVs, the crystallization of PDI should be avoided. The twisted TPE core structure could largely prevent the crystallization, and **36** forms an amorphous thin film with a root-mean-square roughness of 0.207 nm, making it a suitable candidate for OPVs. Utilizing **36** as the acceptor and poly[4,8-bis(5-(2-ethylhexyl)thiophen-2-yl)benzo[1,2-b;4,5-b']dithiophene-2,6-diyl-alt-(4-(2-ethylhexyl)-3-fluorothieno[3,4-b]thiophene-)-2-carboxylate-2-6-diyl)] (PBDTT-F-TT) as the donor, the blended film has surface features with sizes around 20–30 nm, indicating that **36** does not form large domains. Without thoroughly optimizing the device parameters, the OPV device shows a high PCE of 5.53% (Fig. 8). The open circuit voltage (V_{OC}) of the PBDTT-F-TT:**36** device is around 0.91 V, which is much higher than that using the fullerene derivative [e.g., [6,6]-phenyl-C61-butyric acid methyl ester (PCBM)] as the acceptor. In addition, the PBDTT-F-TT:**36** device has a very simplified configuration, which does not require additional interlays or additives to

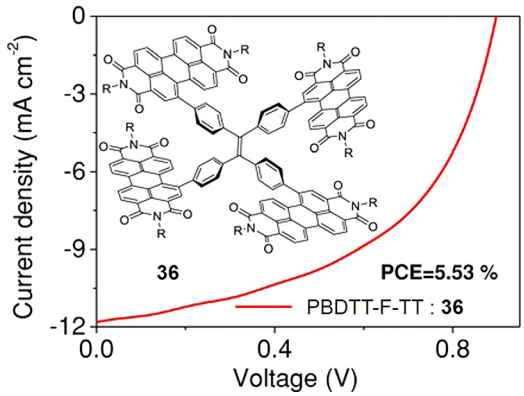

FIG. 8. J-V curve of the solar cells fabricated from **36**. Reproduced with permission from Liu *et al*., Adv. Mater. **27**, 1015 (2015). Copyright 2015 Wiley-VCH.

achieve high performance. The high performance is attributed to the 3D molecular conformation which leads to amorphous film property and high electron mobility, and is evidenced by using a PDI dimmer connected by a biphenyl-bridging group (BP-PDI_2) with a 2D structure as the control group. The electron mobility of **36** is around 1×10^{-3} cm^2 V^{-1} s^{-1} which is 5-fold higher than that of BP-PDI_2. As a contrast, the PBDTT-T-TT:BP-PDI_2 film has large domain sizes around 60–80 nm with a low PCE of 3.1%. AIEgens usually adopt high twisted structures in solid state, which not only activate RIM and prevent strong π-π stacking interactions to achieve high luminescence, but also are able to form 3D charge-transporting networks. Although the development of AIE based OPV materials has been rare until now, it indeed represents one of the excellent light-to-electricity converting materials for clean energy to solve increased environmental concerns and global warming issues.

4. Optical waveguides

Besides OLEDs, OFETs, and OPVs, AIE active materials have also been developed with optical wave-guiding properties for propagation of luminescence emission. Pyridinium-substituted TPE salt, **37** [Fig. 9(a)], developed by Zhang *et al*. has been reported to show optical wave-guiding properties.[80] **37** is non-emissive in good solvents, and the addition of poor solvent leads to amorphous precipitates with largely increased emission centered at 617 nm with an η of 37.0%. **37** forms microcrystals under slow evaporation of the solution in the methanol/water mixture, which displays blue shifted emission centered at 528 nm with a higher η of 77.0% as compared to its amorphous solid. The dense arrangement of the cations (pyridinium-substituted TPE) and the $(CF_3SO_2)_2N^-$ anion in crystalline state leads to a more twisted conformation, which interprets the blue-shifted emission for **37**. The crystalline **37** exhibits multiple short interatomic interactions with more rigidified conformation as compared to amorphous solids, and hence, **37** microcrystals display higher brightness. In addition, the amorphous and crystalline states of **37** can be tuned via solvent vapor exposure and grinding. On exposure to methanol vapor, the red emissive amorphous solid is transformed into crystalline with green emission, which can be further converted back to amorphous solids by exposure to CH_2Cl_2 or grinding. The microcrystals of **37**, in the shape or microrods, exhibit green emissive spots at the two ends of the microrods, with weaker emission at rod-bodies [Fig. 9(b)]. The optical wave-guiding behavior was studied by excitation of the microrod at designated positions (labelled as 1′, 2′, 3′, 4′, 5′, and 6′) [Fig. 9(c)] and the emission spectra were collected by the ends of the microrods of **37**. Upon increasing the propagation distance, the emission brightness at the end of microrod decreases, correspondingly [Fig. 9(d)], while the intensity at the excited locations does not change substantially. The optical loss coefficient of **37** microrod at 530 nm is calculated to be 15.74 dB/mm. As demonstrated, AIEgens are able to form well-ordered morphologies, and together with their bright luminescence in the solid and crystalline states, which makes AIEgens active wave-guiding materials.

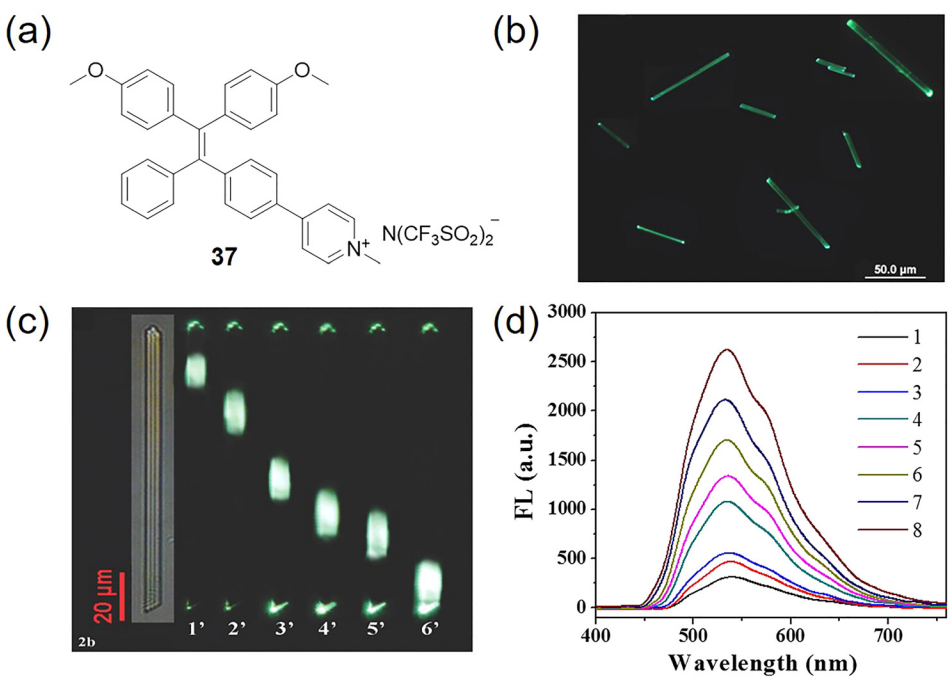

FIG. 9. (a) Chemical structure of **37**. (b) Fluorescence (FL) microscopy images of microrods of **37**. (c) Bright-field (inset, left) and microarea FL images of **37** by exciting the respective microrods at six different positions with the focused UV laser (380 nm). (d) Spatially resolved FL spectra of the emission that are out-coupled at the microrod tip of **37**. Reproduced with permission from Hu *et al*., Small **11**, 1335 (2015). Copyright 2015 Wiley-VCH.

5. Luminescent solar concentrator (LSC)

Luminescent solar concentrators (LSCs) are light harvesting devices that concentrate the sunlight to photovoltaic devices located at the edges, which could improve the output of OPVs, especially in urban environments with limited direct sunlight.[81,82] A typical LSC is a transparent plastic waveguide slab embedded with fluorophores of high quantum yields [Fig. 10(a)]. These fluorophores absorb sunlight and emit light inside LSCs. The emitting light is trapped by the internal reflection and concentrated to the small solar cells at the edge. Two limiting factors have hampered the LSC developments: one is fluorescence quenching at high concentrations and in solid state, which restricts the amount of doped dyes to be used and affects the light harvesting and emission; the other is the emission reabsorption due to small Stokes shifts of conventional dyes.[83] AIEgens exhibit remarkable high fluorescence quantum yields in aggregated state and large Stokes shift with minimum reabsorption loss, which provide good opportunities for the development of LSCs with high fluorophore doping concentration without compromising the emission.[84] Wong and coworkers demonstrated this proof-of-concept idea by using two AIEgens, TPE and **38** [Fig. 10(b)] as the fluorophores for LSC fabrication in 2014.[85] They fabricated a monolithic LSC by drop casting 10% w/w of TPE in poly(methyl methacrylate) (PMMA) onto the surface of 10 mm × 10 mm × 1 mm glass substrate with a geometric ratio of 2.5. This TPE-based PMMA LSC showed a thickness of 116 nm. Benefiting from the AIE feature of TPE, this LSC showed a high absolute fluorescence quantum yield of 40%. As compared to its face emission, the LSC edge showed a much higher intensity [Fig. 10(c)], indicating that the emitted photons can be effectively trapped and concentrated to the edge. The optical efficiency of the LSC, defined by the ratio of the edge photons to the total number of incident photons, is measured to be 13.2%, which is very close to the predicted

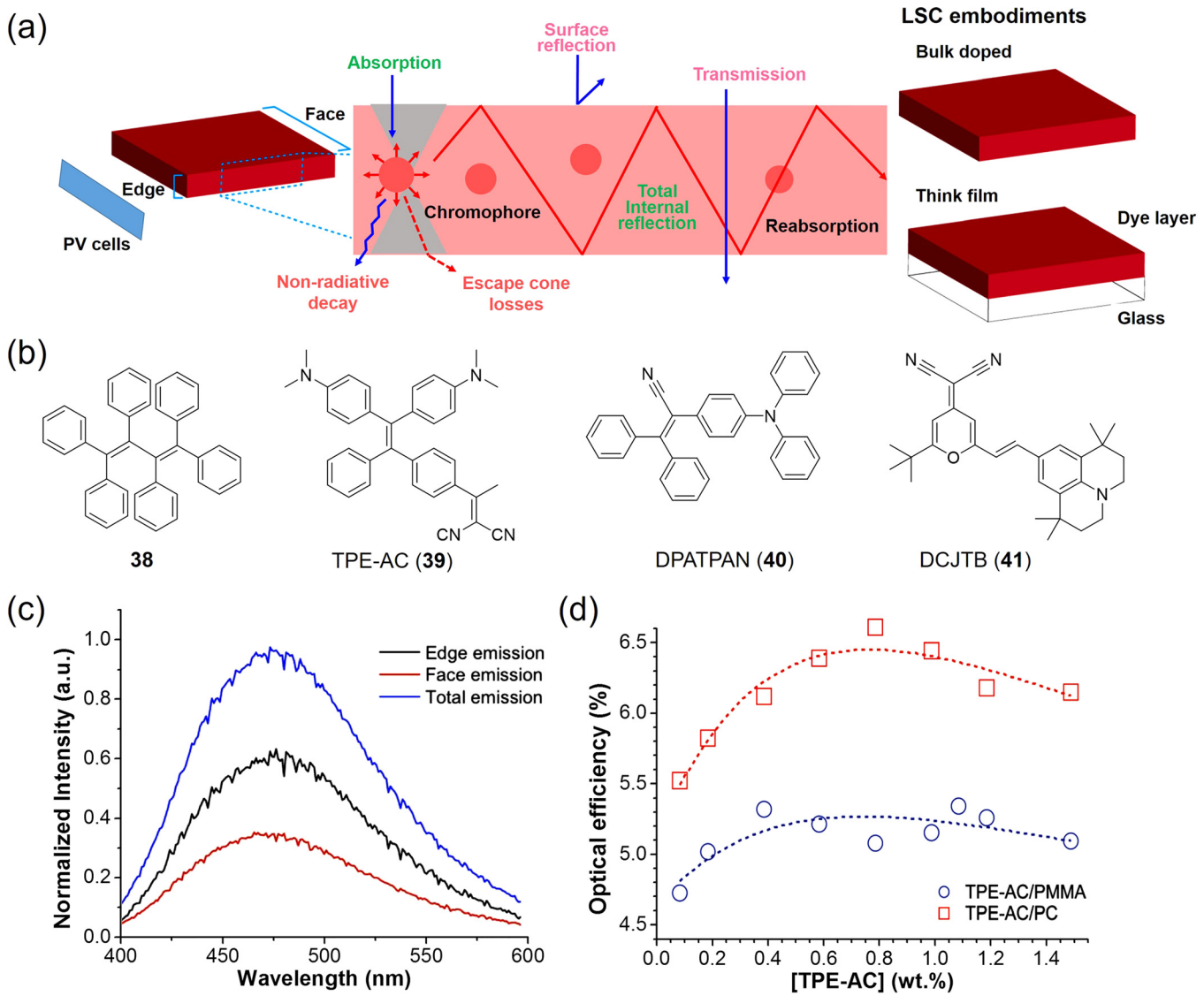

FIG. 10. (a) Schematic illustration of luminescent solar concentrators (LSCs). Adopted from Wong *et al.*, Acc. Chem. Res. **50**, 49 (2017). Copyright 2017 American Chemical Society. (b) Chemical structures of **38**, TPE-AC (**39**), DPATPAN (**40**), and DCJTB (**41**). (c) Total, edge, and face emission spectra of TPE-based LSCs. Reproduced with permission from Wong *et al.*, Sci. Rep. **4**, 4635 (2014). Copyright 2014 Nature Publishing Groups. (d) Optical efficient variations of TPE-AC/PMMA and TPE-AC/PC LSCs as a function of fluorophore content. Reproduced with permission from Pucci *et al.*, Mater. Chem. Front., "Red-emitting AIEgen for luminescent solar concentrators" (published online). Copyright 2017 Royal Society of Chemistry.

stimulation value of 13.4% with the same geometric ratio and zero reabsorption loss. On the other hand, TPE analogue **38**, with an extended absorption spectrum as compared to TPE, shows a quantum yield of 31.2% but a lower optical efficiency of 8.0% when casted in PMMA films. The decreased optical efficiency is ascribed to the higher reabsorption loss for **38** (2.3%) as compared to TPE (0.2%) due to its higher extent of absorption and emission spectra overlap (over two orders of magnitude higher than TPE). As a proof of concept, AIEgens with high emission in solid state lead to fabrication of LSCs with higher fluorophore doping concentration without scarifying the emission quantum yield, and the large Stokes shift also leads to lower reabsorption loss, which shall represent a novel class of LSC materials.

Very recently, Pucci and coworkers used a red emissive AIEgen, TPE-AC [**39**, Fig. 10(b)] for LSC development.[86] TPE-AC is doped in two transparent polymers, PMMA and polycarbonate (PC) for LSC fabrication, which showed a thickness of 25 ± 5 μm. TPE-AC showed a broad absorption band from 400 to 550 nm which is highly favorable for harvesting light in the UV and visible regions. The emission peaks for TPE-AC/PMMA and TPE-AC/PC films are located at 600 and 620 nm. The large Stokes shift of over 150 nm could largely reduce the reabsorption of emission. At 0.1 wt. % TPE-AC doping concentration, the fluorescence quantum yields for TPE-AC/PMMA and TPE-AC/PC films were measured to be 50% and 46%, respectively. The quantum yields decreased to 30% when further increasing the TPE-AC concentration to 1.2-1.5 wt. %, which are still considered excellent for LSC fabrication at such a long wavelength emission. The optical efficiency variations as a function of TPE-AC concentration are shown in Fig. 10(d). The TPE-AC/PC showed an optical efficiency of 6.7%, which is comparable and higher than most red-emitting fluorophore based LSCs at the same concentration.[87,88] Besides solely utilizing AIEgens as the emitting fluorophores in LSCs, Wong *et al.* also reported an excitation energy transfer approach for LSCs by using 2-(4-(diphenylamino)phenyl)-3,3-diphenylacrylonitrile (DPATPAN, **40**), an AIEgen as the energy donor and a conventional dye 4-(dicyanomethylene)-2-tert-butyl-6-(1,1,7,7-tetramethyljulolidyl-9-enyl)-*4H*-pyran (DCJTB, **41**) as the acceptor [Fig. 10(b)].[89] Benefited from the AIE feature, DPATPAN showed a nearly 100% quantum yield in solid state, which allowed it to be used in high concentrations to provide efficient energy transfer to the acceptor dye without the concentration quenching issue. 10% w/w of the dye blend (DCJTB:DPATPAN = 1:99) in PMMA was used for LSCs, which gave a high optical efficiency of 58.2%. This clearly demonstrated the superiority of AIEgens in LSCs as compared to conventional dyes. High dye doping concentration could also largely reduce the thickness of LSCs to achieve efficient light absorption without compromising its emission quantum yields. Hence, we foresee the great opportunities of AIEgens in the development of commercially viable LSC devices.

6. Circularly polarized luminescence (CPL)

CPL reflects the chirality of materials in excited state, which has been using to study the conformational and stereochemical structural information. Materials with excellent CPL performance have been widely applied in various optoelectronic and biosensing applications.[90] The emission efficiency and emission dissymmetry factor (g_{em}), are two important parameters to evaluate CPL performance, which should be as high as possible for better CPL properties. However, most commonly used CPL materials have a very small g_{em} value of $\sim 10^{-5}$ to 10^{-2} in solution. When used in condensed phases, the g_{em} values become even worse due to the ACQ effect, which also leads to lower luminescence efficiency. As a unique phenomenon exactly opposite to ACQ, AIE shall represent one of the promising solutions to surmount these limitations of the ACQ effect. The appropriate introduction of AIEgens to chiral moieties could afford novel AIE-active CPL materials with much improved luminescence efficiency and g_{em}. Utilizing a characterized silole as the centered AIE core, and mannose or phenylethanamine as the chiral blocks, the obtained **42** and **43** represent two of the particular examples of AIE-active CPL materials.[91]

42 [Fig. 11(a)] displays no luminescence or circular dichroism (CD) signal in good solvents such as CH_2Cl_2. Upon inducing aggregate formation by addition of poor solvent hexane, **42** shows largely intensified emission with η increased from 0.6% in solution to 31.5%. And the η further increases to 81.3% in solid thin film, indicating **42** is AIE active. The aggregation of **42** also leads to the switch-on of the CD signal as observed by the emergence of CD absorption at 278 and 340 nm, indicating the aggregation-induced CD. The peak centered at 340 nm also suggests that the chiral sugar pendant and the triazolylphenyl together induce the silole core to form helical arrangement with a preferred screw sense. The aggregation-induced CD effect was further proved by the case films formed through doping **42** in the PMMA matrix, as well as the right-handed helical nanoribbon and superhelical rope morphologies of **42** self-assembled aggregates. The dependence of g_{em} on wavelength under different situations is shown in Fig. 11(b). In solution, no CPL signal is detected due to the free and random intramolecular motions. Once **42** forms aggregates in heterogeneous solution or cast films, the g_{em} showed a range of −0.17 to −0.08 [Fig. 11(b)], such a two orders of magnitude higher value than previously reported organic CPL materials, which clearly suggests the excellent CPL performance of **42**. Moreover, the pattern formed by a Teflon-based microfluidic technique gives a much higher g_{em} value up to −0.32, owing to largely enhanced parking order by a confined microenvironment. As a conclusive remark, the AIE-active **42** shows the best result among the reported organic conjugated molecular systems in terms of emission efficiency, dissymmetry factor, and spectral stability, which represents a class of desired molecular functional materials for generating efficient CPL in the solid state.

Compound **43** [Fig. 11(a)] synthesized by linking silole with chiral phenylethanamine through thiourea linkage is a new AIE active CPL material with a controllable signal.[92] **43** exhibits classic AIE properties, where it shows no emission in solution but the fluorescence can be turned on by aggregate formation in poor solvent or in solid thin film with a nearly unity η of 95.0%. Different from **42**, the CD signal of

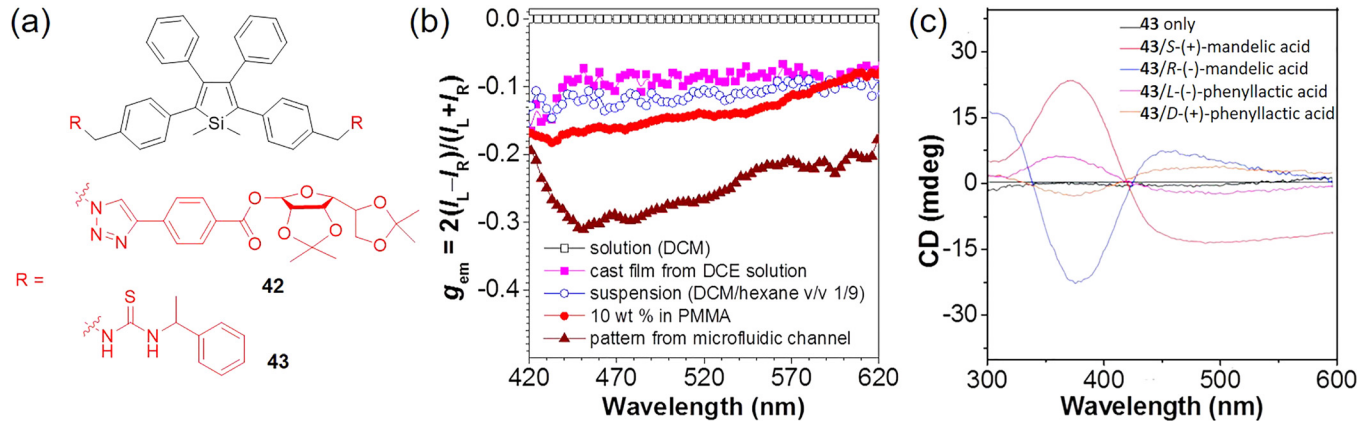

FIG. 11. (a) Chemical structures of **42** and **43**. (b) CPL dissymmetry factor gem (g_{em}) versus wavelength for **42** existing in different formats: DCM solution, DCM/hexane (v/v, 1:9) mixture (suspension), neat cast film from DCE solution of 2 mg/ml, dispersion in the polymer matrix (10 wt. % in PMMA), and fabricated micropattern by evaporation of DCE solution in microfluidic channels. Reproduced with permission from Liu *et al.*, Chem. Sci. **3**, 2737 (2012). Copyright 2012 Royal Society of Chemistry. (c) CD spectra of **43** in the presence of chiral hydroxyl acids in solid thin film state. [**43**] = 1 mM, [acid] = 40 mM. Reproduced with permission from Ng *et al.*, J. Mater. Chem. C **2**, 78 (2014). Copyright 2014 Royal Society of Chemistry.

43 cannot be switched on in aggregate state or even in solid thin film, due to the non-favorable self-assembly properties of the thiourea bridge and the weak intermolecular interactions. The complexation of **43** with special chiral hydroxyl acids, such as mandelic acid, could lead to the potential hydrogen-bonding between the thiourea and the carboxylic acid groups, which is able to induce the silole cores to be rearranged in helical manners with observed CD signals [Fig. 11(c)]. The chiral aliphatic acids such as malic and tartaric acids cannot induce the CD signal, which indicates the important role of the phenyl group from mandelic acid played in the complexation-induced CD. This is also evidenced by the fact that phenyllactic acid with phenyl rings and two hydroxyl groups can also switch on the CD signals of **43** [Fig. 11(c)]. The g_{em} values of **43** are about −0.01, or +0.01 when it is complexed with *R*-(-)-mandelic acid or *S*-(+)-mandelic acid, respectively, indicating that the CPL can be tuned to be left- or right-handed by enantiomer types of mandelic acid. The luminescence and CD signal of **43** remain silent in solution. As such, the AIE-active materials represent a class of novel organic molecules for generating excellent CPL in solid state.

7. Liquid crystals (LCs)

As compared to conventional liquid crystal displays (LCDs) where the non-emissive liquid crystals (LCs) require an extra light source, the emergence of luminescent LCs has shown great advantages in terms of simplified device design, low energy consumption, high brightness, and contrast ratios.[93] However, the luminescence efficiency of LCs still remains challenging, mainly due to the fluorescence quenching associated with the highly ordered molecules in crystalline for conventional ACQ fluorophores.[94] The unique feature of AIEgens to have bright emission in solid especially crystalline state makes them a promising candidate for light-emitting LCs. In this subsection, we would like to reveal the great potential of AIEgens for LCs using the compound **44** [Fig. 12(a)] synthesized by linking four mesogenic units of 4-ethynylpropylbenzene to TPE as an example.[95] The liquid crystalline property of **44** is first revealed by the polarized optical microscopy [Fig. 12(b)], where **44** forms an anisotropic mesomorphic texture when being heated in the temperature range of 218–228 °C. In addition, the **44** LC is monotropic as the mesomorphic texture disappears upon

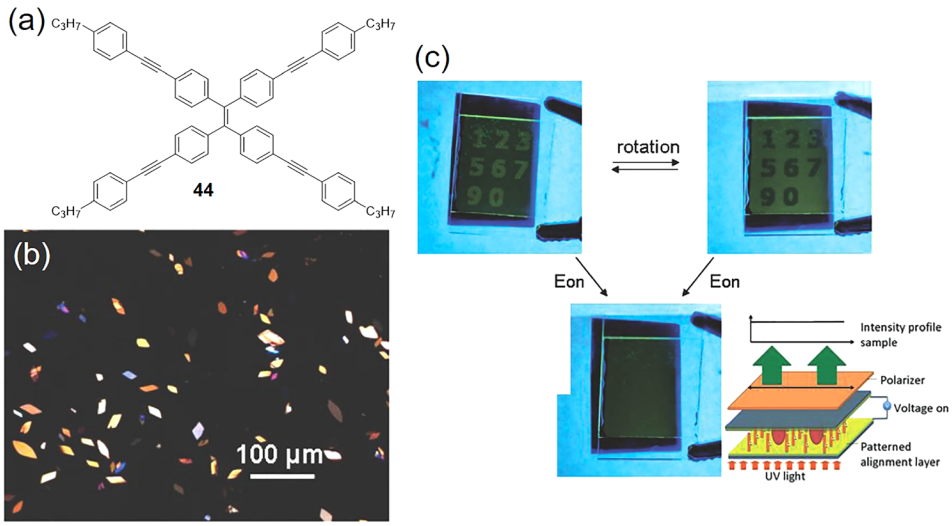

FIG. 12. (a) Chemical structure of **44**. (b) POM photograph recorded on heating **44** at 222 °C. (c) The LE-LCD in the electric field off/on condition. Under UV irradiation and field-off condition, the regions with and without figures in the device are alternately bright and dark, viewing through the rotatable polarizer. Under UV irradiation and field-on condition, both the two regions are light-emitting and the figures disappeared. Reproduced with permission from Zhao *et al.*, Adv. Opt. Mater. **3**, 199 (2015). Copyright 2015 Wiley-VCH.

cooling, which is also confirmed by the differential scanning colorimetry (DSC). Utilizing the AIE and mesogenic properties, **44** (0.1 wt. %) is dissoluted into nematic LC PA0182 to prepare the LC mixture for polarized fluorescence. The light-emitting liquid crystal display (LE-LCD) device based on the LC mixture was further fabricated as shown in Fig. 12(c). A UV lamp was used as the light source and a polarizer was applied to analyze the changes of photoluminescence efficiency. At voltage off state, the different direction of the polarizer is able to change the dark and bright area reversibly, where either the numbers or the background shows photoluminescence to give clear display of the number combination. Applying a voltage of 8 V (1 kHz) leads to the same photoluminescence efficiency for the whole cells, and all the figures in two original displays disappear. This strategy of synthesizing AIE LCs presents a valuable strategy for development of LC devices with a simplified structure and low energy consumption.

8. Photonic crystals

Photonic crystals (PCs) are able to display emitted light by controlling the propagation of light *via* the photonic band gaps, and many living organisms switch their PC colors for social communication, sexual attractions, etc.[96] The combination of reflected light from PCs and the luminescence from fluorophores would create miraculous phenomena, and is of great importance for lots of potential applications. However, the ACQ effect always leads to diminished emission in solid or crystalline state. Conversely and luckily, the excellent emission of AIEgens in solid state makes it possible to realize the luminescence for PCs. In 2016, Tang *et al.* reported a unique PC system based on AIEgen **45** and PMMA nanoparticles where the simultaneous tuning of reflected light and emitted light becomes possible.[97] An emulsion polymerization approach is chosen to synthesize the **45**-loaded PMMA nanoparticles, where the THF solution of **45** is mixed with hot aqueous solution containing methyl methacrylate (MMA) and sodium dodecyl benzene sulfonate [Fig. 13(a)]. The polymerization was induced by $K_2S_2O_8$ under 1 h incubation at 80 °C. During the polymerization, the hydrophobicity leads to the encapsulation of **45** by PMMA nanoparticles with sodium dodecyl benzene sulfonate (SDBS) as the hydrophilic surface, which was also evidenced by the occurrence of the light creamy yellow solution. The PC hydrogel assembly was formed by centrifuging the PMMA nanoparticles at a high speed of 12 000 rpm. These PMMA nanoparticles have a uniform size of 120 nm and are arranged in a face-centered cubic pattern [Figs. 13(b) and 13(c)]. The **45**-PMMA PC hydrogel displays a violet color under light. The reflectance peak centers at 460 nm with a very narrow photonic band gaps. The obtained PC is able to change its color upon exposure to water stimulation [Fig. 13(d)]. With increased water volume from 0 to 150 μl, the reflected light color changes from violet to blue, green, yellow, orange and red, with the corresponding bathochromic shifted reflection spectra from 460 to 618 nm [Fig. 13(e)]. The red shifted photonic band gap is ascribed to the expanded PC lattice space by aqueous medium, as **45**-PMMA nanoparticles were surrounded by the SDBS aqueous solution. The fluorescence emitted from **45** in the **45**-PMMA PC can also be tuned. Due to the TICT characteristics, **45**

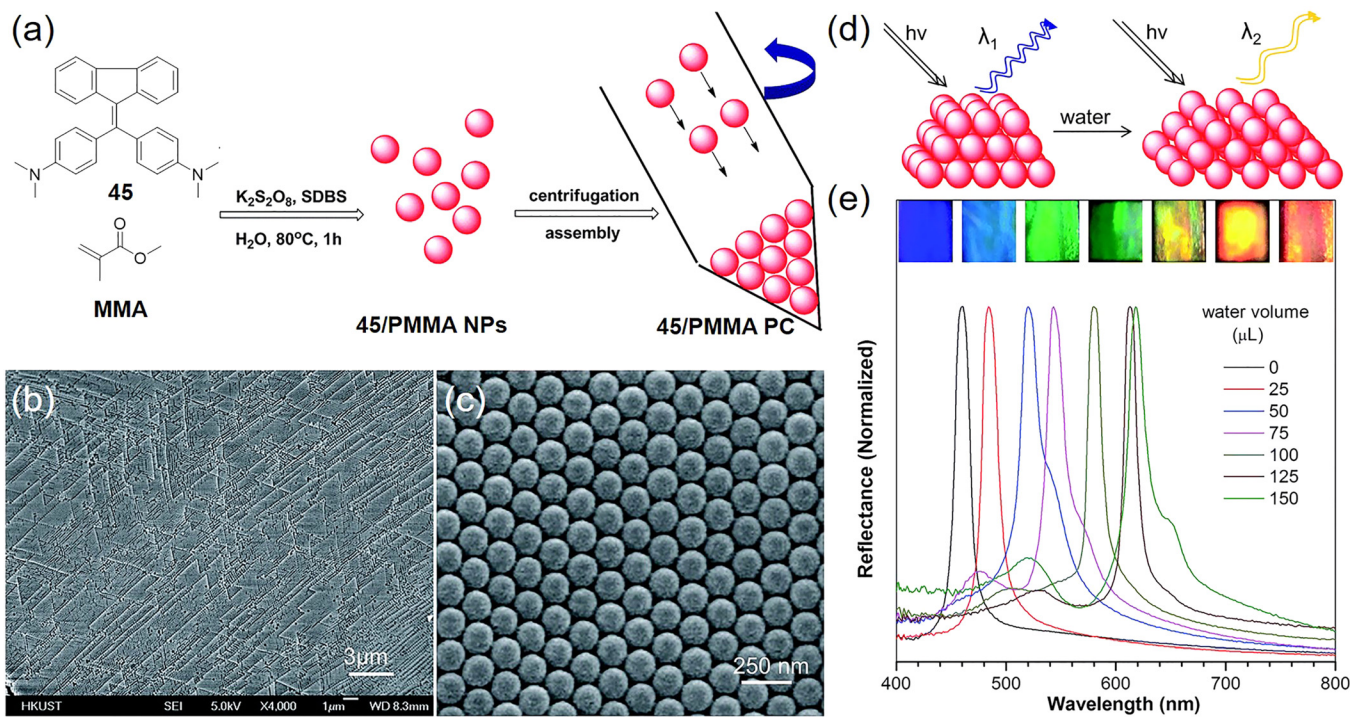

FIG. 13. (a) Schematic illustrating the molecular structure of **45** and the assembly process of the **45**/PMMA PC. (b) SEM image and (c) enlarged SEM image of **45** functionalized PMMA PC. (d) Schematic illustrating the swelling process of the **45**/PMMA PC. (e) Photographs (inset) and corresponding reflection spectra of the **45**/PMMA PC hydrogels upon adding different amounts of water: 0, 25, 50, 75, 100, 125, and 150 ml (by volume), respectively. Reproduced with permission from Wang *et al.*, Chem. Sci. **7**, 5692 (2016). Copyright 2016 Royal Society of Chemistry.

exhibits prolonged emission in polar solvent, which helps explain the longer emission of **45** aggregates in THF/water (630 nm) than **45**-PMMA PC (583 nm) as PMMA encapsulation provides a less polar microenvironment for **45**. Along with increased water content, the photonic band gap becomes smaller, and it is able to inhibit the light propagation and quench the emission of **45**, which leads to reduced full width at half maximum from 127 nm at water volume of 0 μl to 92 nm at water volume of 150 μl. With the help of AIEgens, the luminescent PC system with multi-functionality and controllability is developed, which can be potentially applied in humidity detection as well as other photoelectric devices.

9. Aggregation-induced photon upconversion

Most of the reported AIE systems we have discussed earlier are mainly based on single-excitation processes to achieve bright fluorescence in solid state. Very recently, Kimizuka *et al*. reported that triplet-excitation processes could also have the AIE effect and they realized the aggregation-induced photon upconversion through two excited triplet annihilation.[98] In this process, a donor (sensitizer) in triplet excited state is able to populate triplet excited state of the acceptor (emitter) *via* triplet-triplet energy transfer. The collision and annihilation of two triplet states during their lifetime are able to form a higher singlet energy level and emit delayed and upconverted fluorescence. They used (2Z,2′Z)-2,2′-(1,4-phenylene)bis(3-phenylacrylonitrile) (**46**) and Pt^{II}octaethylporphyrin (PtOEP) as the acceptor and donor pair [Fig. 14(a)]. **46** exhibits a typical AIE character, nearly no emission in solution is observed, but it shows intensified fluorescence centered at 485 nm in solid powder. The **46**/PtOEP mixture in THF solution does not show upconverted emission upon excitation at 532 nm, even with an excitation power up to 220 mW/cm^2, while their mixed powder displays clear upconverted emission at 485 nm under the same laser excitation [Fig. 14(b)]. In THF solution, PtOEP itself shows bright phosphorescence at 650 nm with a single exponential decayed lifetime of 66 μs. The presence of **46** not only efficiently quenches the phosphorescence of PtOEP, but also significantly promotes the phosphorescence decay, indicating that the triplet energy of PtOEP is transferred to the triplet state of **46** in solution. However, the triplet states of **46** cannot undergo the two excited triplet annihilation process to produce upconverted fluorescence. Their triplet excited states undergo immediate ISC to ground state due to the conformational twisting around double bond and the photoisomerization in triplet state. In solid state, the large structural change is prohibited which also prevents the crossing from triplet state to ground state, and **46** exhibits a very long triplet state lifetime of ~90 μs, which is long enough for the triplet excitons to migrate, collide, and eventually annihilate to produce upconverted emission [Fig. 14(c)].

10. Logic gate

Molecular logic systems have great potential in the applications of information process and medicine.[99] Fluorescence materials show superior performance in construction of simple and combinational logic systems in terms of sensitivity and feasibility, but these devices employ

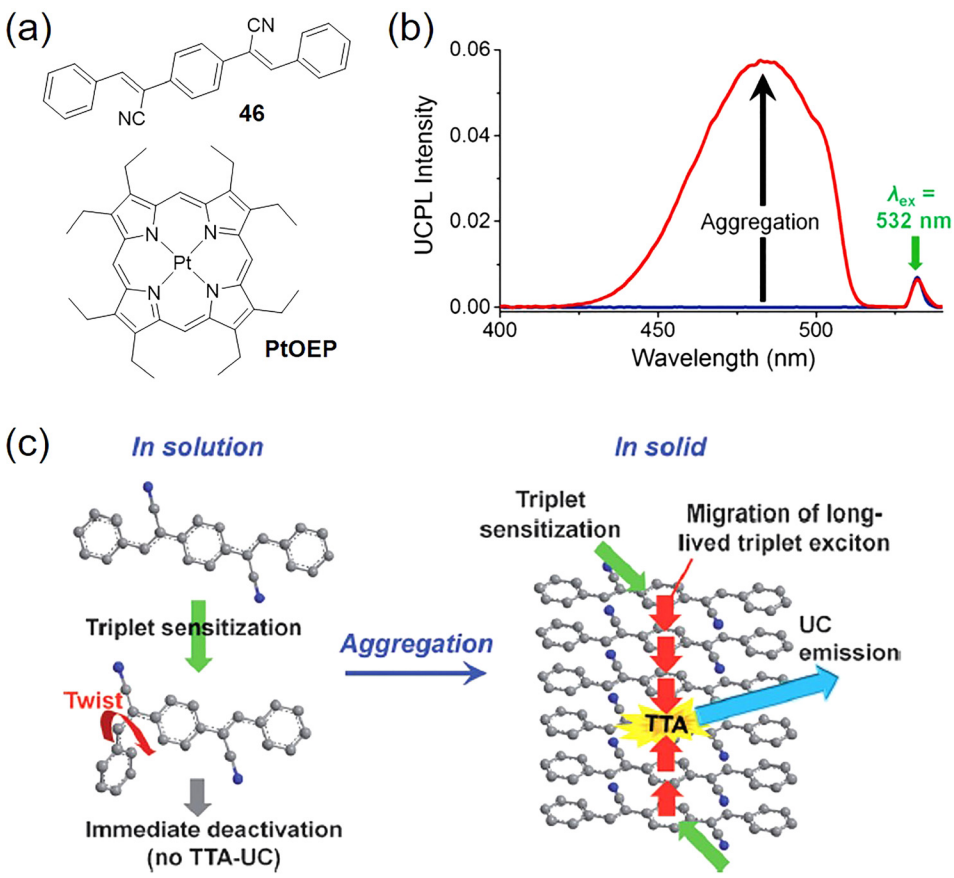

FIG. 14. (a) Chemical structures of **46** and PtOEP. (b) PL spectra of **46**/PtOEP pair in THF deaerated by repeated freeze-pump-thaw cycle (blue line, [PtOEP] = 0.1 mM, [**46**] = 10 mM), and in solid powder under vacuum (red line, PtOEP/**46** = 1:500). (c) Schematic representation of aggregation-induced photon upconversion (AIPUC). Reproduced with permission from Duan *et al*., Angew. Chem. Int. Ed. **54**, 7544 (2015). Copyright 2015 Wiley-VCH.

fluorescent properties of molecules in solution. The discovery of AIE provides great opportunities to develop bright and tunable solid-state emitters, which opens the new avenue for memory devices, sensors, and the solid state logic operation.[100] The Λ-shaped 3,4-bis(4-(9-carbazolyl)phenyl)-*N*-methylmaleimide (**47**) [Fig. 15(a)] is one example of AIEgens that have been used for construction of solid state logic gate systems where fluorescence intensity or wavelengths are used as a signal output.[101] **47** adopts a D-π-A-π-D structure, and the strong ICT effect from the carbazole donor to maleimide carbonyl acceptor leads to a large Stokes shift of over 200 nm as well as a distinctive solvent-dependent emission behavior. Its emission peak shifts from 574 nm in toluene to 649 nm in acetonitrile. **47** exhibits a typical AEE feature, which shows weak emission with a η of 4.0% in good solvents such as dichloromethane, but emits strongly in solid state. The η of **47** in powder and film state was measured to be 38.0% and 10.0%, respectively. As the powder adopts a crystal structure while the film is amorphous, **47** exhibits crystal-induced emission enhancement (CIEE) activity. Three different crystals for **47** are obtained (RC, YC1, and YC2), where RC shows a red emission with a η of 23.0%, while YC1 and YC2 exhibit similar greenish emission with ηs of 72.0% and 80.0%, respectively. Moreover, applying different external stimuli is able to tune the optical properties of these solids [Fig. 15(b)]. Grinding the yellow emissive pristine powder ($\eta = 38.0\%$) leads to weak orange emission with a η of 8.0%, while further heating the powder at 105 °C for 3 min or fuming in acetone vapor for 5 min could return the solid back to its initial yellowish state. This yellow-orange-yellow switching can be reversibly repeated many times. In addition, heating at 160 or 290 °C, grinding or fuming could also lead to the switching between different fluorescence states for RC crystal of **47**. Four simple sequential logic (AND, NAND, INHIBITOR, and IMPLICATION) and one non-sequential gate NOR can be constructed based on the fluorescence intensity and wavelength changes upon different treatments [Fig. 15(c)]. For example, using heating RC at 290 and 105 °C for 3 min as input and yellow fluorescence at 560 nm as the output (I_{560}) an AND gate operation was designed. The unique properties of **47** crystals with tunable fluorescent properties (as the output, I_{560}, I_{640}) under different inputs (290, 105, 160 °C, grinding) make it possible to construct more complicated logic gates [Fig. 15(c)].

B. Physical processes

Most of the organic materials are soft materials and they are flexible and dynamic. Their conformational shapes can be changed along with different physical processes, during which their property changes can reflect and probe these processes, such as morphology changes, crystallization, and other single or multiple physical processes. Fluorescence is a very sensitive technique with ease of handling and accessing, which further makes AIE materials an excellent toolbox for detection and visualization of different physical processes. In this section, we discuss how AIEgens are engineered to respond to or monitor different physical processes such as glass transition, crystallization, self-assembly, and polymer gelation.

1. Glass transition

Glass transition refers to the reversible transition between glassy state and rubbery PMMA of amorphous polymers which normally is associated with large changes in their mechanical properties.[102] The determination of the glass transition temperature (T_g) is very important in their

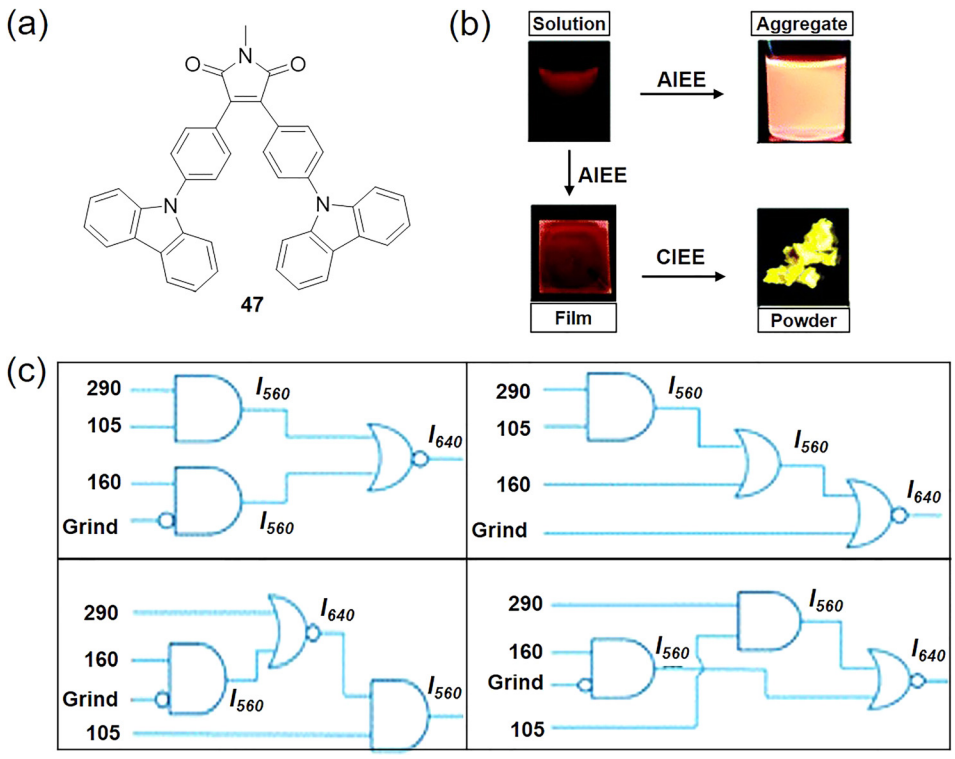

FIG. 15. (a) Chemical structure of **47**. (b) Pictures of **47** solid with different treatments under UV light. (c) Combinational logic operations with four sequential inputs based on **47** solid. Reproduced with permission from Mei *et al.*, J. Mater. Chem. C **3**, 7267 (2015). Copyright 2015 Royal Society of Chemistry.

practical applications, such as solar cells and drug release. The current techniques for T_g determination are based on dilatometry or dynamic mechanical analysis and DSC, which suffer from different drawbacks. For example, dilatometry has poor accuracy,[103] dynamic mechanical analysis requires a large amount of samples,[104] and DSC only gives a temperature range.[105] Fluorescence with high sensitivity appears to be a promising approach but the weak fluorescence of conventional fluorophores in aggregated state hampers their sensitivity. In this regard, AIE active materials are able to provide accurate information about T_g based on their excellent brightness in solid state that cannot be achieved by conventional ACQ fluorophores.[106] In one study reported by Tang and Liang *et al*., amorphous polystyrene with narrow molecular weight distribution was selected as the model polymer. TPE (**1**) was uniformly doped into the polystyrene matrix without forming large aggregates, which renders the TPE/polystyrene mixture bright blue emission under UV radiation. DSC analysis reveals that TPE doping does not cause noticeable changes to the glass transition of polystyrene, which occurs in a temperature range of 78–98 °C with a center at 89.5 °C (T_g). The emission spectra of the TPE/polystyrene mixture at different temperatures are shown in Fig. 16(a). It clearly shows that the fluorescence intensity of TPE decreases with rising temperature. The plot of peak intensity against temperature gives two straight dropping lines below and above 80 °C, and the slope increases after 80 °C [Fig. 16(b)]. The T_g for polystyrene was determined to be 80 °C, which was very close to the onset temperature of 78 °C, much more accurate than the DSC result. At low temperature below 80 °C, TPE molecules are doped in glassy polystyrene polymer matrices, the rigid structure can restrict the intramolecular motions of TPE, which leads to an enhanced radiation dissipation pathway, and hence, TPE gives high fluorescence. Above T_g, the polystyrene is in rubbery state, the movement of polystyrene chains is not able to restrict the free intramolecular motions of TPE. These motions consume more excited state energy, leading to less efficient fluorescence of TPE. TPE also shows excellent repeatability in monitoring the glass transition of the TPE/polystyrene mixture, where repeatedly altering the temperature between 40 and 110 °C gives reversibly switchable fluorescence intensity. Considering the ease of luminescence spectrometers, AIEgens provide a facile and straightforward determination of the glass transitions of the polymers.

2. Crystallization

The transformation from amorphous-to-crystalline (ACT) of organic molecules has played indispensable roles in lots of research fields such as semiconducting processing, catalysis, and drug delivery.[107] Although the ACT process in semiconductors is fairly well studied, it remains challenging to reveal the detailed crystallization processes for complex molecules, especially the solid state crystallization. Due to the ambiguous interface between amorphous and crystalline regions, the study of ACT is still really rare even with high-edge instrumentation.[108] AIEgens exhibit bright emission in different solid states, and their emission colors and brightness could vary between amorphous and crystalline states, which thus could provide a facile way to realize real-time monitoring of the ACT process using a standard optical microscope. Tao *et al*. reported an *in situ* microscopic observation of ACT by using AIE microparticles.[109] Figure 17(a) shows the structure of the selected AIE active molecule, 1,2-bis(7-bromo-9,9-dibutyl-fluorenyl)-1,2-diphenylethene (**48**). **48** crystal gives a deep-blue emission (emission peak at ~460 nm) and the fluorescence changes to greenish color (emission peak at ~520 nm) when it forms amorphous powders [Fig. 17(b)] with an absolute η over 90.0%. The microparticles with size around 3 μm formed solely from **48** were used for ACT process study. Before exposure to ethanol vapor, these microparticles exhibit bright green fluorescence with a relatively dark spot in the center. Exposing them to ethanol vapor could induce the ACT process, where at 10 h, the microparticles emit dense blue fluorescence with a shallow blue ring around, which separated the blue crystal core from an amorphous greenish shell. Along with the increased fuming time, the shallow ring disappeared and the blue crystalline core kept increasing in size. Moreover, diffraction analysis also revealed that the green-to-blue emission transition was associated with crystalline formation, which thus provided a direct visualization of the ACT process. Further investigation was carried out to study how small fragment interaction with the microparticle shell could affect the ACT process. When a small fragment slightly touches the particle surface, it is gradually absorbed by and merged into the microparticles, which does not affect the

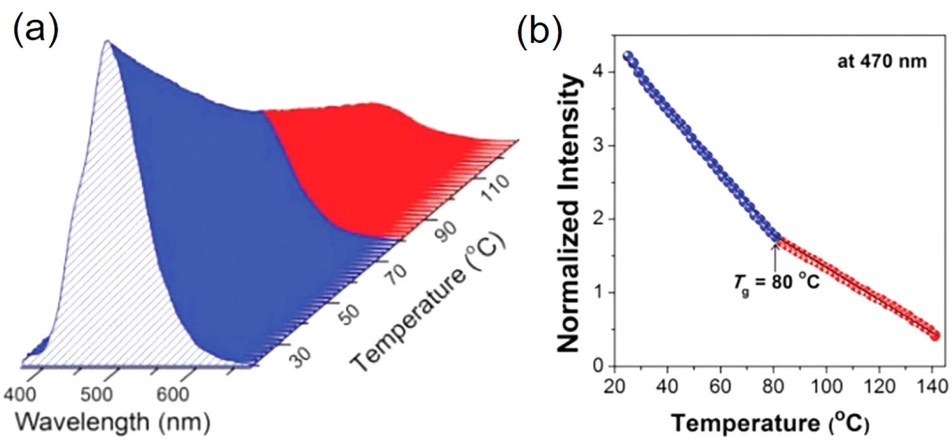

FIG. 16. (a) Fluorescence spectra of polystyrene doped with 0.1 wt. % TPE (**1**) at various temperatures and (b) fluorescence intensity at 470 nm as a function of temperature normalized to 110 °C. Excitation: 350 nm. Reproduced with permission from Bao *et al*., Polym. Chem. **6**, 3537 (2015). Copyright 2015 Royal Society of Chemistry.

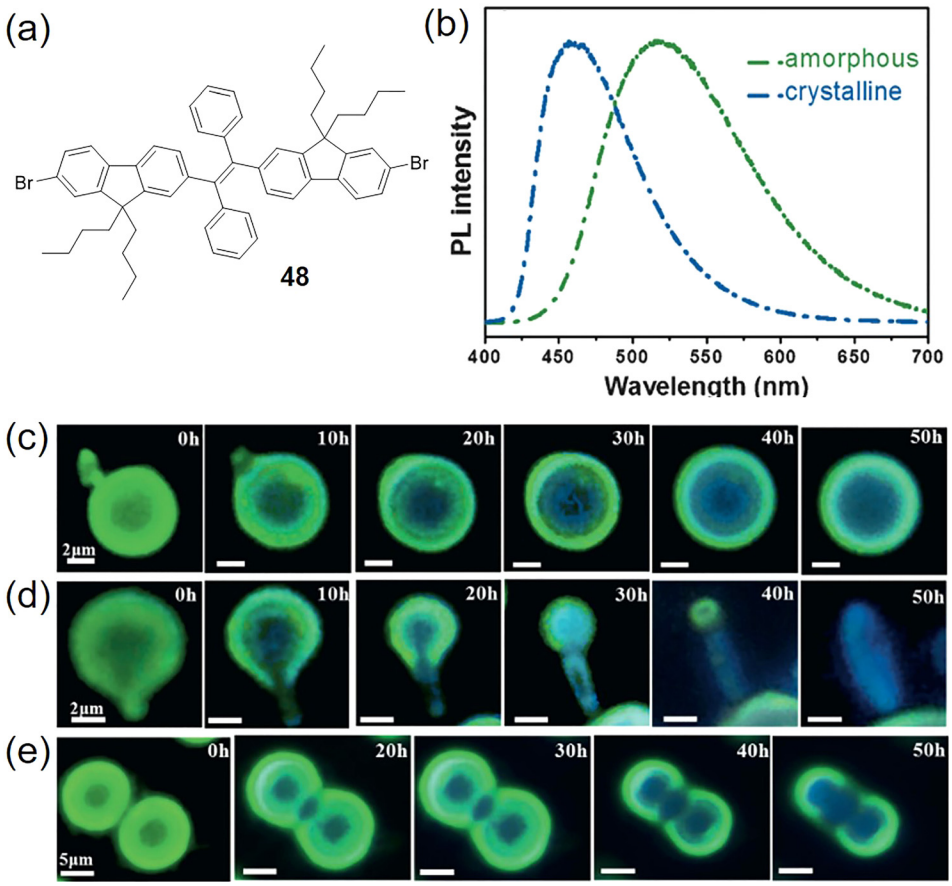

FIG. 17. (a) Chemical structure of **48**. (b) PL spectra of **48** in crystalline and amorphous states. (c)–(e) Fluorescence images of the crystallization process due to contact between microparticles. (c) Slight contact with a fragment, (d) in-depth contact with fragment, and (e) twin microparticles. The scale bars in (c) and (d) are 2 μm, and those in (e) are 5 μm. Reproduced with permission from Ye *et al.*, Angew. Chem. Int. Ed. **54**, 7976 (2015). Copyright 2015 Wiley-VCH.

crystallization of the core [Fig. 17(c)]. When the fragment is moved heavily to strike a microparticle, crystallization takes place at the contact site as well as the microparticle core, both crystalline sections join together to form a longer ribbon at the expense of the microparticle size [Fig. 17(d)]. When two microparticles contact with each other, both the cores and the interacted location have the ACT process, and the crystalline parts eventually join together to form the capsule-like ellipsoid with a uniform amorphous shell [Fig. 17(e)]. As efficient solid state emitters with distinguishable emission color in amorphous and crystalline states, AIEgens could serve as excellent materials for monitoring crystallization processes.

3. Self-assembly

Self-assembly refers to the physical process where large organic molecules or polymer aggregates in response to solvent polarity or solubility change, and it plays fundamental roles in nature. The study of the spontaneous interfacial self-assembly process especially in highly dynamic interfacial layers remains to be captivating.[110] The unique feature of AIEgens to alter their emission properties in response to the microenvironment changes provides a special window for real-time monitoring of dynamic self-assembly at thin interfacial layers. A hyperbranched polymer (**49**) [Fig. 18(a)] was designed by incorporating TPE into polytriazine as the repeating unit.[111] **49** is an AIE-active polymer with strong emission as nanoaggregates or when forming rigidified patterns [Fig. 18(b)]. To study the self-assembly process, the chloroform solution of **49** was cast onto a glass side under humid airflow, which formed the honeycomb-like porous arrays driven by the hydrophobic force [Fig. 18(c)]. This self-assembly process was visualized in four steps [Figs. 18(d)–18(f)]. In step 1, small water droplets were first formed on the surface of chloroform solution without any observable fluorescence, indicating that **49** was well dissolved without aggregate formation. In step 2, the droplets assembled into ordered arrays and stop grows, and started to emit weak fluorescence, suggesting that **49** was enriched and aggregated at water-oil and water-air interfaces along with the chloroform evaporation. With further chloroform evaporation in step 3, the film around the water droplet started to burst in different directions, during which process **49** was accumulated at bursting gap edges. In the final step, a highly fluorescent film with ordered porous arrays was formed after complete evaporation of water and chloroform. This study reveals that wrapping the water droplet by a thin film layer followed by rupture and expansion plays an important role in the interfacial self-assembly process.

4. Micelle formation

Another example of self-assembly is the formation of micelles, which is the aggregation of surfactant unimers in aqueous solution when the surfactant concentration is above the critical micelle concentrations (CMC). The application of surfactants and study of surfactant micelle transition processes remain a very hot topic. The rapid advance of modern techniques has provided kinetic monitoring of these transitions such as using *in situ* small-angle X-ray scattering.

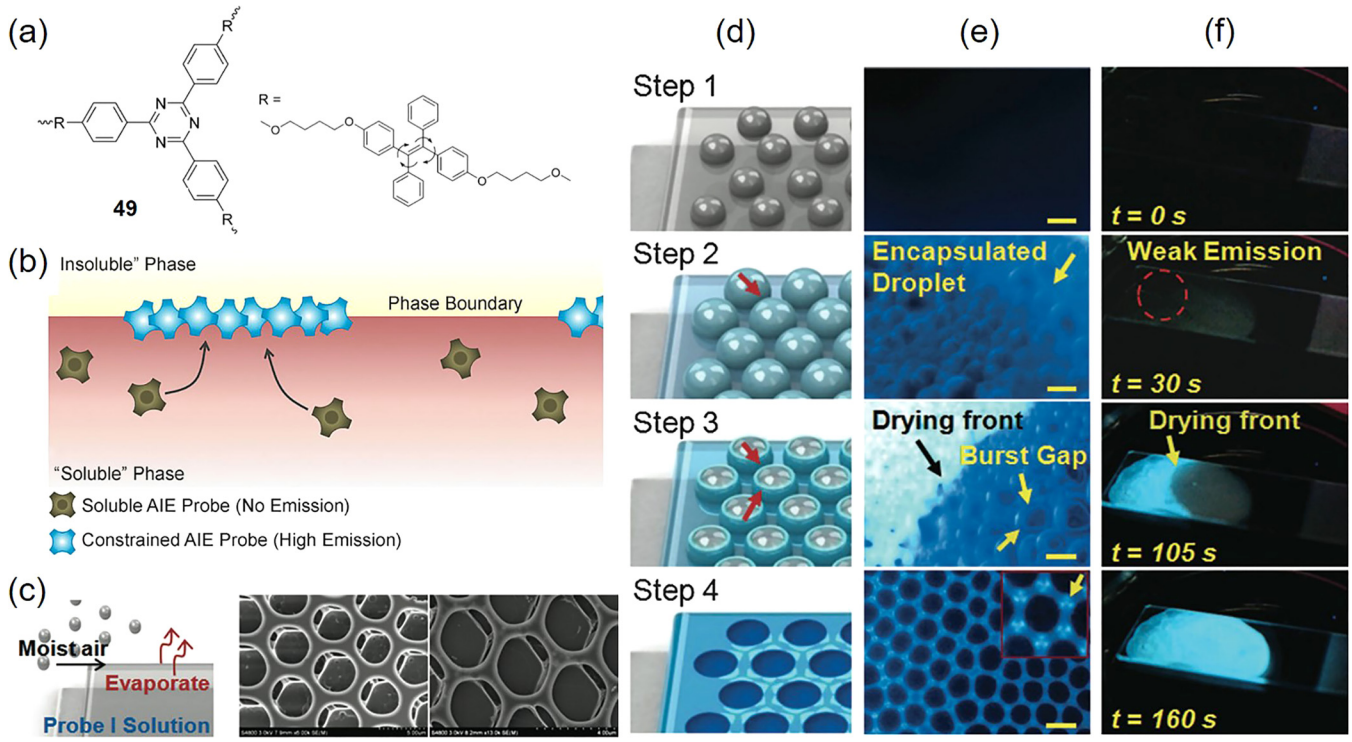

FIG. 18. (a) Chemical structure of **49**. (b) Schematic of **49**-based imaging technology for real-time monitoring of the interfacial processes. (c) Schematic of breath-figure formation and representative SEM images of the ordered porous film formed by breath figures. (d) Schematic illustration, (e) fluorescence microscopy images, and (f) representative progressing frames showing macroscopic evolution of emission signal of the four main steps of breath figures observed with *in situ* AIE imaging. Reproduced with permission from Li *et al.*, Angew. Chem. Int. Ed. **53**, 13518 (2014). Copyright 2014 Wiley-VCH.

However, as the most widely used imaging method, direct visualization of micelle transition by fluorescence still remains rare, mainly due to the ACQ effect of conventional fluorophores. With the help of AIEgens, efficient emission in aggregate state is achieved. By incorporating TPE units into sodium dodecyl sulfonate, the AIE surfactant (**50**) [Fig. 19(a)] was designed for direct observation of micelle transitions and formation of microemulsion droplets (MEDs).[112] The CMC for **50** was evaluated by surface tension as well as conductivity variation measurements, which gave a CMC value around 30 μM. The transmission electron microscope (TEM) image for 40 μM **50** reveals spherical shaped micelles with a radius of 3.5 $\pm$ 0.5 nm, suggesting that **50** is a typical anionic surfactant. **50** has two absorption peaks at 250 nm and 318 nm corresponding to phenyl groups and conjugated TPE, respectively. Along with increased concentration in aqueous solution, **50** shows gradually increased fluorescence with an inflection point at 30 μM, after which the fluorescence enhancement rate decreases, indicating the changes of aggregate state. Such changes should be due to the formation of micelles, where the TPE units presented in the nonpolar interior of micelles have more freedom as compared to that in the aqueous environment. The structure transitions of **50** micelles can be induced by adding the neutral electrolyte (e.g., NaCl) into water and monitored by a confocal microscope. The size of **50** micelles is beyond the resolution of confocal measurement, and hence they exhibited as luminescent dots due to the diffraction blur [Fig. 19(b)]. Upon addition of 0.5 M of NaCl into the **50** micelle aqueous solution, the effective thickness of the micelle double layers reduced, which resulted in the reduced repulsion between micelle anionic heads. As a result, the anionic heads pack in a more compact manner, and the spherical micelles are transitioned into rod-like micelles [Fig. 19(c)]. Further increasing the

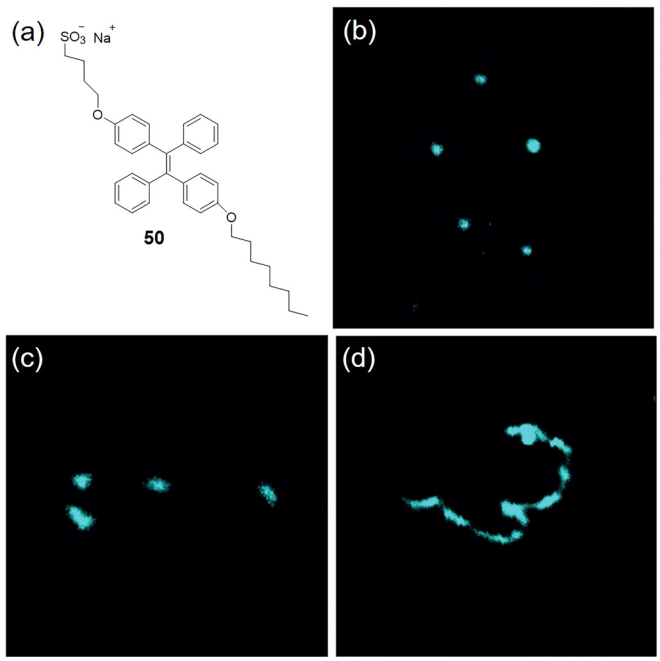

FIG. 19. (a) Chemical structure of **50**. (b)–(d) Fluorescence microscopy images of the **50** micelles in (b) pure water, (c) 0.5 M NaCl solution, and (d) 1.0 M NaCl solution. [**50**] = 80 μM. Reproduced with permission from Guan *et al.*, Angew. Chem. Int. Ed. **54**, 15160 (2015). Copyright 2015 Wiley-VCH.

NaCl concentration to 1.0 M leads to elongated rods and occurrence of wormlike micelles [Fig. 19(d)]. TEM and rheology measurements also show similar micelle transition processes, but they are not able to provide the most direct visualization of the native state of these transition processes. Computational analysis using a mathematical model revealed that the distance between two adjacent TPE units should be less than 0.54 nm (half of TPE length) to activate the RIR and micelle emission. This study not only demonstrated a feasible approach for real-time monitoring of the micelle transition process, but also further elucidated the AIE mechanism.

5. Gelation

Hydrogels, especially chitosan (CS) based hydrogels that provide a large range of applications, have drawn tremendous research attention.[113] Among different methods used to fabricate CS based hydrogels such as cross-linking and complexation with other polymers, the solubilization of CS in acidic aqueous solution represents the most facile approach. Using alkali-urea as the aqueous medium, CS hydrogels with excellent hardness, strength, and toughness have been developed.[114] However, detailed understanding of the gelation process is still limited. The current direct gelation visualization methods are based on a scanning electron microscope (SEM) or TEM, which requires dry samples, so that they cannot be used to study the native stage of hydrogels.[115] Due to the lack of suitable tools, direction visualization of the transformation during the entire gelation process has not been investigated. Utilization of fluorescence techniques is a convenient approach, but the diminished emission in aggregate state has hampered their great potential. Very recently, Tang *et al*. have successfully realized the visualization of the gelation process of CS LiOH-urea solution with the help of AIEgens.[116] In their demonstration, TPE was used to label CS to yield TPE-CS (**51**) [Fig. 20(a)]. TPE-CS with different degrees of labelling (DLs) were synthesized, and these samples exhibited light yellow color under normal room light and emitted strong blue light under UV illumination [Fig. 20(b)]. TPE-CS showed intensified brightness and decreased solubility along with increased DLs, and TPE-CS with DL of 1.54 mol. % to minimize the TPE interference towards the CS gelation was used for monitoring of the gelation processes of CS, where CS and TPE-CS exhibited similar gelation behaviors. A confocal laser scanning microscope was used to real-time visualize the gelation process in a CS concentration range of 10^{-2} g/ml. The solution of TPE-CS shows a uniform light blue image without any specific pattern [Fig. 20(c)]. At the thermal gelation stage upon heat absorption starts, some areas appear bright blue emission, which keep growing along with the heating time. The fluorescence increase stops after a certain time with stabilized patterns, indicating the terminal point of thermal gelation [Fig. 20(d)]. However, this point does not represent the termination of the entire gelation process, as the removal of LiOH and urea could further induce the development of gel structures [Fig. 20(e)]. Further study of optical transparency and elastic behaviors showed good consistence with the fluorescence imaging, which indicated that the entire gelation process involved two stages. The embryonic structure and crystal were formed during the thermal gelation stage driven by elevated temperature; the rinse stage increased these inter/intramolecular hydrogen bonds which caused the increased toughness and volume shrinkage. This study provides a simple and straightforward method to study various gelation systems.

6. Inorganic composite dispersion

Organic-inorganic composites have been very actively involved in various scientific researches. Understanding how the inorganic compounds are dispersed into organic matrices plays important roles for further improving their properties.[117] The dispersion state and the dispersion-property correlation have been widely studied by TEM or 3D-TEM tomography. However, these observations require very complex and time-consuming handling from professional personnel. In addition, the small observation windows of TEM are

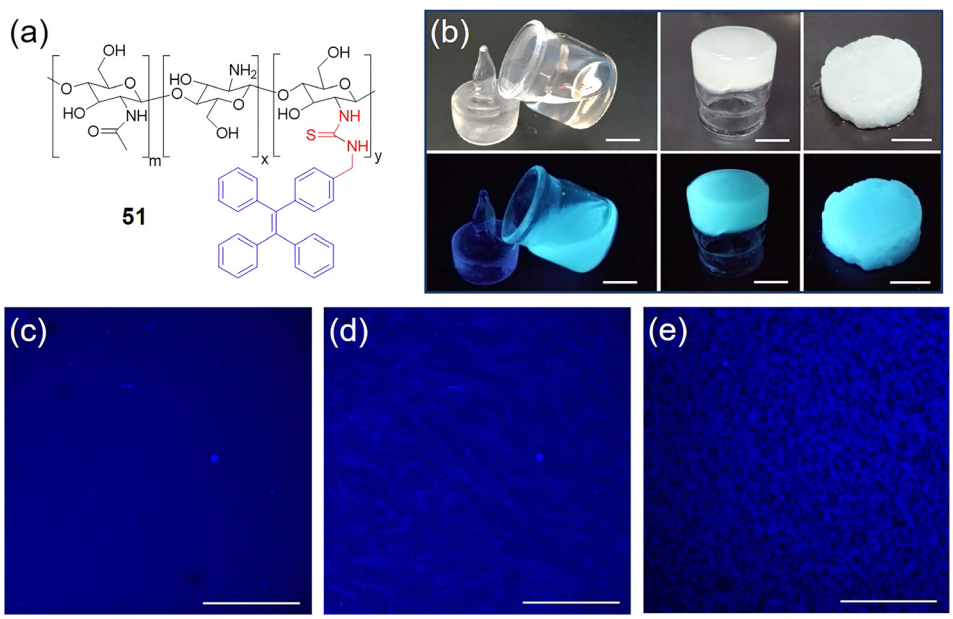

FIG. 20. (a) Chemical structure of **51**. (b) Digital images of formation of hydrogel with **51**: solution of **51**, **51** gel after thermal gelation, and **51** hydrogel after complete removal of LiOH and urea; scale bar: 5.0 mm. The fluorescent photographs were taken under ultraviolet illumination (365 nm). (c)–(e) Confocal laser scanning fluorescence microscope images of the gelation process of **51**: (c) solution; (d) gel after thermal gelation; (e) hydrogel after rinse procedure; Scale bar: 250 μm (c)–(e). Reproduced with permission from Wang *et al*., Nat. Commun. **7**, 12033 (2016). Copyright 2016 Nature Publishing Group.

only suitable for organic-inorganic composite dispersion at nano-scales, which is not truly representative of the whole sample. A fluorescence microscope with ultrafast scanning speed and 3D visualization functionalities appears to be a powerful imaging technique for organic-inorganic composite dispersion study with large windows, but has not yet been applied until the emergence of AIEgens to provide efficient emission in solid state. Utilizing TPE-cored dodecyltrimethylammonium bromide cationic surfactant (**52**) [Fig. 21(a)], the polyvinyl chloride (PVC)/montmorillonite (MMT) organic-inorganic composite macrodispersion was directly observed under a confocal fluorescence microscope.[118] The conductivity measurement revealed a CMC value of 32 μM for **52**. The plot of peak fluorescence of **52** at 490 nm versus its concentration showed two straight lines with different slopes and an inflection point at 32 μM, which indicated that fluorescence properties could also be used for CMC determination. It is well known that mixing Na^+-MMT with an organic polymer matrix induces the agglomeration of Na^+-MMT particles to form organic-inorganic composites. **52** was intercalated into the interlayer space of Na^+-MMT and the external surface inorganic cation Na^+ was replaced by TPE-DTA^+ with a zeta potential (ξ) change from -28.8 mV to approximately 0 mV due to the positive ξ of **52** around 43.5 mV. With more hydrophobicity, the **52**-modified MMT appeared to be very swollen as compared to the well dispersed Na^+-MMT particles. **52**-modified MMT powders emit very strong blue fluorescence, with a much improved η of 42.1% as compared to **52** in solution ($\eta = 5.8\%$), while Na^+-MMT does not emit any fluorescence. The higher η of **52**-modified MMT is contributed to the tightly restricted intramolecular motions of **52** in the rigid framework of the MMT layer. The macrodispersion of **52**-modified MMT on the PVC/MMT (5 wt. %) composite is investigated by TEM and confocal microscope. The TEM image only shows the morphology and microdispersion of **52**-modified MMT in the PVC matrix from its lateral slice [Fig. 21(b)]. The morphology and the dispersion state of **52**-modified MMT can be clearly observed from the strong blue emission, and with a large imaging window (600 × 600 μm^2) where hundreds of luminescent particles are seen on the dark ground [Figs. 21(c) and 21(d)]. Using the Z-scan technique, multiple images with different depths provide a spatial distribution of the **52**-modified MMT particles in the PVC matrix [Fig. 21(e)], which thus provides a real and impartial 3D dispersion state of MMT. In addition, the rapid advance of fluorescence imaging techniques with high spatial resolution such as stimulated emission depletion impartial or stochastic optical reconstruction microscope (STORM) could further provide more accurate information of these organic-inorganic composites. To conclude, using AIEgens as efficient solid state emitters, the confocal imaging technique has facilitated the investigation of various solid state physical processes of organic-inorganic hybrid composites with high sensitivity and feasibility.

C. Stimulus processes

AIEgens are "smart" materials as they are able to change their properties, particularly fluorescence properties, in response to single or multiple stimuli processes. The unique feature of AIEgens to tune their optical properties towards changes from solution to aggregate, or from amorphous to crystals has facilitated the study of different stimuli processes, such as solvent polarity, temperature, pH, force, and fuming. In this section, we demonstrate how to engineer AIEgens to be stimuli responsive with some typical examples.

1. Mechanochromism

Organic molecules can easily form soft materials, which tend to show pronounced responses to external stimuli. These responses are not limited to the changes of molecular packing, but also can reflect the electronic or optic changes.

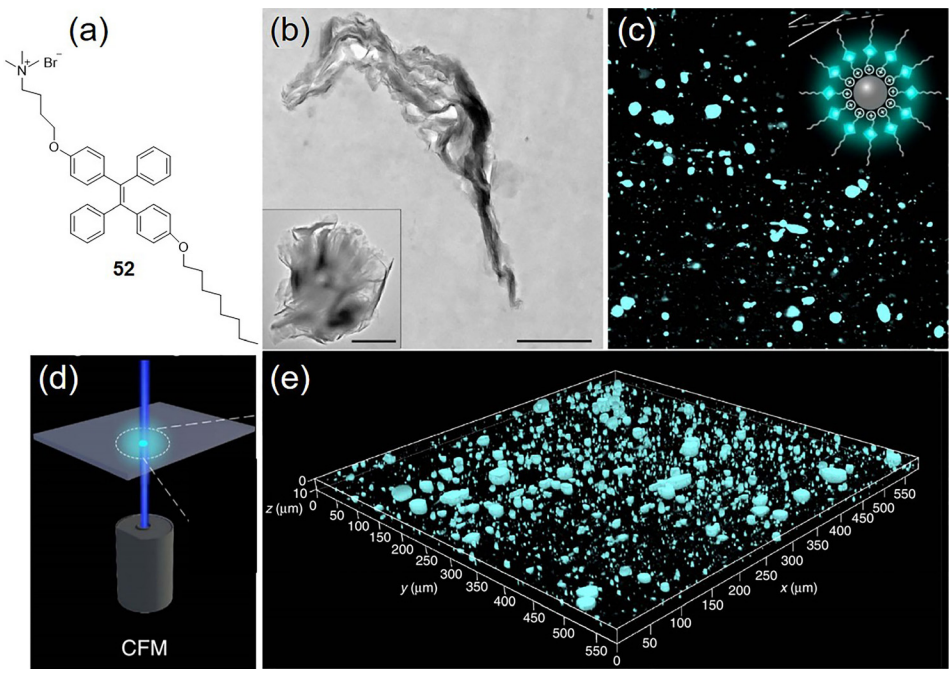

FIG. 21. (a) Chemical structure of **52**. (b) Cross-sectional TEM micrograph of PVC/**52**-modified montmorillonite MMT (5 wt. %) composite; the inset showed the TEM image of **52**-modified MMT. Scale bar: 1 mm. (c) Fluorescence microscopy image (600 × 600 μm^2) of PVC/**52**-modified MMT (5 wt. %) composite. (d) Schematic representation of visualization of 3D macrodispersion of fillers in organic-inorganic composites. (e) 3D representation of **52**-modified MMT dispersion (cyan parts) in PVC matrix. All fluorescence microscopy images were taken with a 405 nm laser. Reproduced with permission from Guan *et al.*, Nat. Commun. **7**, 11811 (2016). Copyright 2016 Nature Publishing Group.

The phenomenon that organic fluorophores change their luminescence in response to mechanical force is referred to as mechanochromism.[119] Materials with mechanochromism have been widely applied in various technological applications, such as memory chips, sensors, and optical storage. AIE materials that exhibit distinguished emission in crystalline and amorphous states are one representative of such smart materials. Their crystalline and amorphous states are controllable by mechanical forces such as shearing or grounding, or by appropriate thermal annealing or vapor fuming. Sun and Tang *et al*. took advantages of the static interaction and developed an ion pair containing a TPE derivative, $[TPE\text{-}DPy\text{-}DMe]^{2+}[PF_6]_2^{2-}$ [**53**, Fig. 22(a)] to demonstrate the mechanochromic behavior of AIE materials.[120] **53** has high yellow emission in crystalline state but moderate red fluorescence in amorphous state. Prepared directly from solvent evaporation, crystals of **53** show an emission peak at 560 nm and a η of 43.0%. When grounding with a pestle or shearling with a spatula, the solid emission peak shifts to ~605 nm with a η of 18.0%, indicating a typical mechanochromic behavior. Different from uncharged TPE molecules that vapor fuming can easily convert their amorphous solids to original crystalline states, the emission change for **53** is irreversible and cannot be recovered to the original yellow greenish state. Dichloromethane fuming for 5 min can only lead to a slight blue-shift of the emission peaks to 598 nm. However, the ground amorphous powder can be recrystallized into the initial state when it is redissolved in dichloromethane and dried. The amorphous ground sample is metastable and it should be recovered to the thermal-stable crystalline state by thermal annealing. However, the thermal annealing at 120, 140, 160, and 180 °C for 1 h can only lead to a slight blue-shift of the emission peak of 2, 6, 3, and 6 nm, respectively, which are very small as compared to the spectra shift between ground and crystalline samples (>40 nm) [Fig. 22(a)]. This thus further proves that the mechanochromic behavior of **53** is irreversible by vapor fuming and thermal annealing. Such irreversible mechanochromic behavior makes **53** an ideal candidate for long term storage applications. Another AIE example with mechanochromic behavior is **54** with an asymmetric D-A-D conformation [Fig. 22(b)].[75] **54** exhibits AIE-delayed fluorescence and white emission in solid state. The emission and XRD analysis were used to study the grinding stimuli effects to **54** [Fig. 22(b)]. With increased grinding time, the crystalline component of **54** is obliterated, where the blue emission centered at 456 nm decreases, while the yellow emission at 554 nm does not show any change. The blue emission is ascribed to the crystallographic state which probably exhibits "quasi-axial" conformer, and the yellow emission is attributed to amorphous state which probably displays "quasi-equatorial" conformers. In addition, **54** also exhibited temperature dependent emission properties, where the blue emission increased with declined temperature, while yellow emission was not responsive to temperature changes.

2. Piezochromism

Piezochromic materials are able to give observable signal changes in response to higher external pressure, which is desirable as pressure sensors for detection of damages. However, due to the collapsing of organic backbones and associated phase transition during compression, piezochromic materials with reversible and reproducible emission

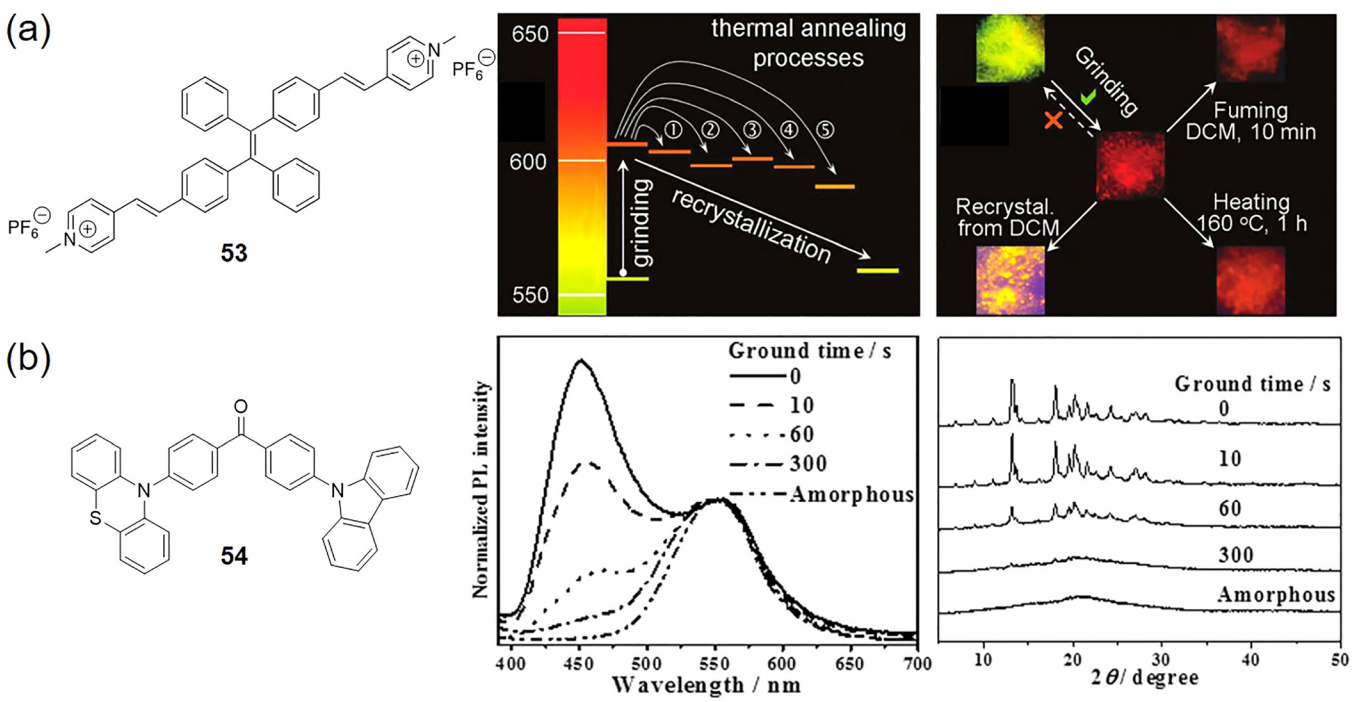

FIG. 22. (a) and (b) Representative examples of mechanochromic AIEgens. (a) Emission peak/color changes of **53** upon grinding or heating, and the photographs of the light emission from **53** of as-prepared crystals, grinded powders. Reproduced with permission from Hu *et al*., Chem. Commun. **51**, 8849 (2015). Copyright 2015 Royal Society. (b) Emission and XRD spectra of **54** upon different grinding time. Reproduced with permission from Xie *et al*., Angew. Chem. Int. Ed. **54**, 7181 (2015). Copyright 2015 Wiley-VCH.

color changes are very rare. AIE-active materials with rigid and highly twisted structures are potential piezochromic materials due to their intrinsic loose packing and space for molecular rearrangement. In 2016, Lu *et al*. reported the AIE crystals of **55** [Fig. 23(a)] with unique piezochromic fluorescence behavior for pressure sensing.[121] Containing cyano- and carbazole substituents, **55** exhibits a highly twisted conformation with strong green emission (emission peak at 529 nm, $\eta = 56.4\%$). Hydrostatic pressure generated from diamond anvil cells was applied to **55** crystals to study the influence of pressure on its fluorescence. Upon increasing the external pressure from 1 atm to 9.21 GPa, the emission color of **55** crystals changed from green to orange and further to red with a red shifted emission peak from 529 nm at 1 atm to 684 nm at 9.21 GPa [Fig. 23(a)]. In addition, the emission could fully recover to green (529 nm) upon releasing the pressure to 1 atm, indicating the excellent reversibility and repeatability of **55** crystals as the pressure indicator. In addition, plotting the emission peak wavelength against the external pressure gave a straight line, which demonstrated a good linear relationship between emission wavelength and pressure. Further *in situ* Raman analysis revealed that the as-prepared **55** crystals have porous and distorted configuration, which provide enough space to withstand high external pressure. The compression under high pressure could lead to shrinkage in a crystal lattice with large deformation but without destroying crystal structures. Such an excellent meta-stability of **55** crystals under external pressure changes ensures its reproducibility and reliability.

In addition to traditional AIE mechanochromic materials, organic-inorganic hybrid materials such as MOFs have also been developed for piezochromism. MOFs have very high porosity and internal surface area, which make them great candidates for various applications. Using TPE-based derivative as linkers, MOFs with high brightness have been demonstrated. Benefited from the highly twisted structure, Zhou *et al*. demonstrated a stable Zr-MOF using TPE derivative **21** as the linker, which showed a unique piezochromic behavior.[122] The Zr-MOF, denoted as **PCN-128W** (PCN stands for porous coordination network, W refers to white), prepared under solvothermal conditions using trifluoroacetic acid as the competing reagent is white crystalline powders under room light. Upon compression with glass slide or treatment with 6.0 M HCl solution, it turned into yellow powders denoted as **PCN-128Y** (Y represents yellow). Both powders are crystalline with a similar structure belonging to the same group (*P6/mmm*) and same topology (csq-a), where the Zr_6 clusters are linked by rectangular **21** planar ligands. However, the coordination sites between Zr_6 clusters are quite different, being trifluoroacetate groups for **PCN-128W** and terminal OH/H_2O groups for **PCN-128Y**. The rectangular linker sizes formed by the four oxygen atoms in **21** are 18.9 × 11.7 Å for **PCN-128W** and 19.7 × 10.0 Å for **PCN-128Y**, respectively [Fig. 23(b)]. The presence of two trifluoroacetate groups oppositely attached to adjacent Zr_6 clusters led to **PCN-128W** as in ascent mode. Under compression, the linkers of **PCN-128W** were able to shrink along the c axis upon compression to yield **PCN-128Y** in descent mode,

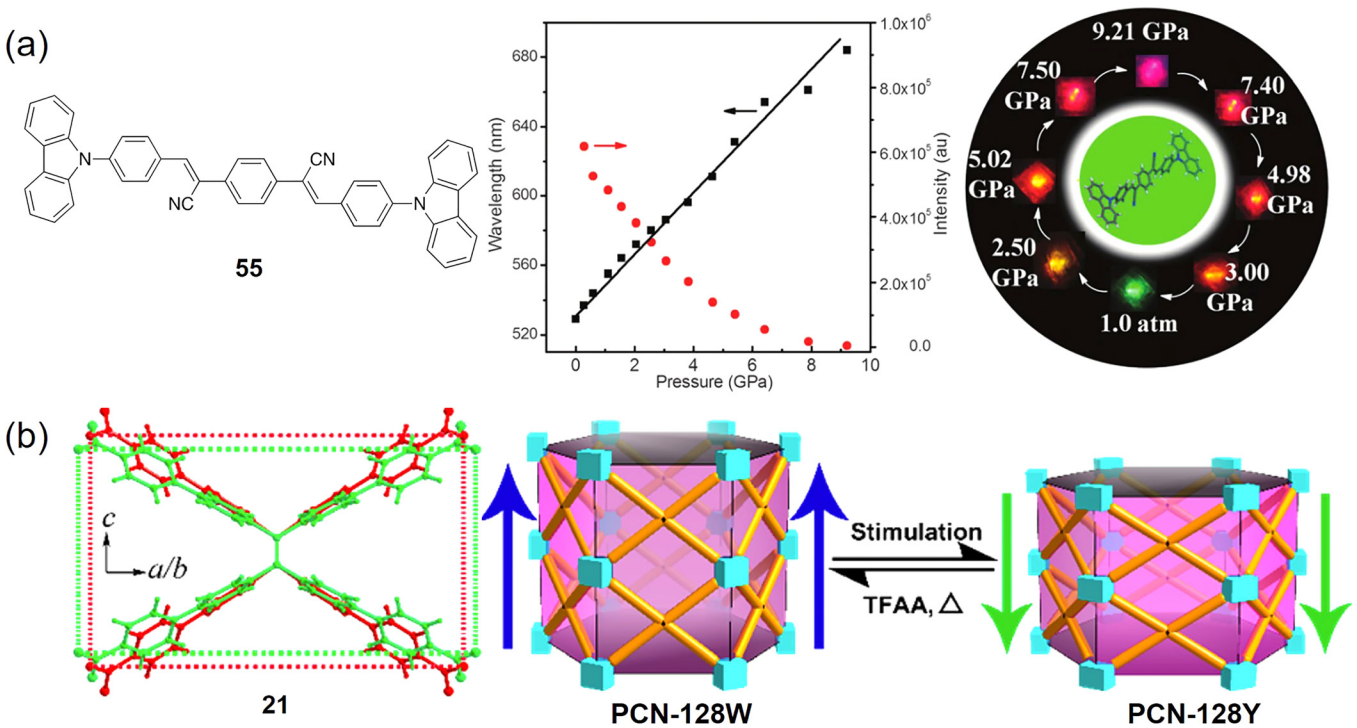

FIG. 23. Representative examples of piezochromic AIEgens. (a) Plot of relative emission wavelength and intensity of **55** *vs*. various pressure and the corresponding images of **55** crystal during a pressurizing and depressurizing cycle: excited by a 355 nm laser. Reproduced with permission from Feng *et al*., Chem. Commun. **52**, 3836 (2016). Copyright 2016 Royal Society of Chemistry. (b) Comparison of **21** linkers in **PCN-128Y** and **PCN-128Y**, and simplified schematic diagram illustrating the reversible motion of **PCN-128W** and **PCN-128Y**, respectively. Reproduced with permission from Zhang *et al*., J. Am. Chem. Soc. **137**, 10064 (2015). Copyright 2015 American Chemical Society.

and the whole process was reversible [Fig. 23(b)]. The freshly prepared **PCN-128W** showed bright blue emission at 470 nm, while the descent **PCN-128Y** emitted green fluorescence at 538 nm, and the emission color changes were associated with rectangular linker changes, indicating the piezochromic behavior of **PCN-128W**. For **PCN-128W**, the coordinated trifluoroacetate groups are able to lock the **21** linkers in an "open" shape, leading to a high HOMO-LUMO energy gap with blue emission. Treatment with strong acids could remove the trifluoroacetate groups, and also remove the hindrance between Zr_6 clusters, which lead to relaxation of the trifluoroacetate linker and slow transformation from **PCN-128W** to **PCN-128Y** at room temperature. Due to the restriction by trifluoroacetate groups, the compression towards **PCN-128W** by glass slide can only lead to the emission shift from 470 nm to 504 nm. After using DMF to remove the TPA groups, the emission of **PCN-128W** is shifted to 508 nm. Further applying compression could lead to red-shifted emission to 536 nm. Such study reveals the promising potential of AIEgens for the development of efficient piezochromic materials.

3. pH

Exhibiting strong proton capture ability, *N*,*N*-diethylbenzenamine has been widely used for developing pH sensors. By replacing the four phenyl rings with diethylbenzenamine groups, tetra(4–(diethylamino)phenyl)ethene (**56**) [Fig. 24(a)] was developed to show multiple stimuli responsive properties.[123] **56** exhibits typical AIE properties, where its fluorescence quantum yields increase from 0.2% in THF to 35.5% as nanoaggregates in the THF/water mixture at a water fraction of 95%. The emission peaks located at 513 and 509 nm are for amorphous and crystals, respectively, with a η of 63.5% for the former, and 68.9% for the latter. Benefiting from the electron rich nature of diethylbenzenamine groups, **56** possesses high electron density and exhibits a strong proton capture capability. The emission spectra of **56** in buffers with different pH vary obviously. Under acidic environments, **56** is protonated to form quaternary ammonium salts (**56a**) with good solubility in aqueous solution, which leads to the dissolution of **56** aggregate. The activation of the free intramolecular rotation of phenyl rotors leads to fluorescence quenching of **56a** in acidic buffer [Fig. 24(b)]. **56** shows very high fluorescence intensity changes in the pH range of 4.0 and 6.0, with a clear and good linear correlation ($R^2 = 0.9210$). The fluorescence switching in response to pH changes is very fast with high repeatability and reliability where no spectral profile changes can be found after 20 cycles [Fig. 24(c)]. As the pH range from 4.0 to 6.0 is crucially important for lysosome physiological processes (pH = 5), acid rain detection (pH = 5.6 – 4.6), and other life and environmental science studies, **56** represents a promising candidate for sensitive pH detection *via* fluorescence. Besides serving as a pH detector in solution, **56** is also responsive to acidic and basic vapors. At neutral state, the powder of **56** is yellow under room light and emits green fluorescence. Upon exposure to HCl for 5 min, the powders turn white under room light and its emission becomes sky-blue. Further treatment with hot trimethylamine

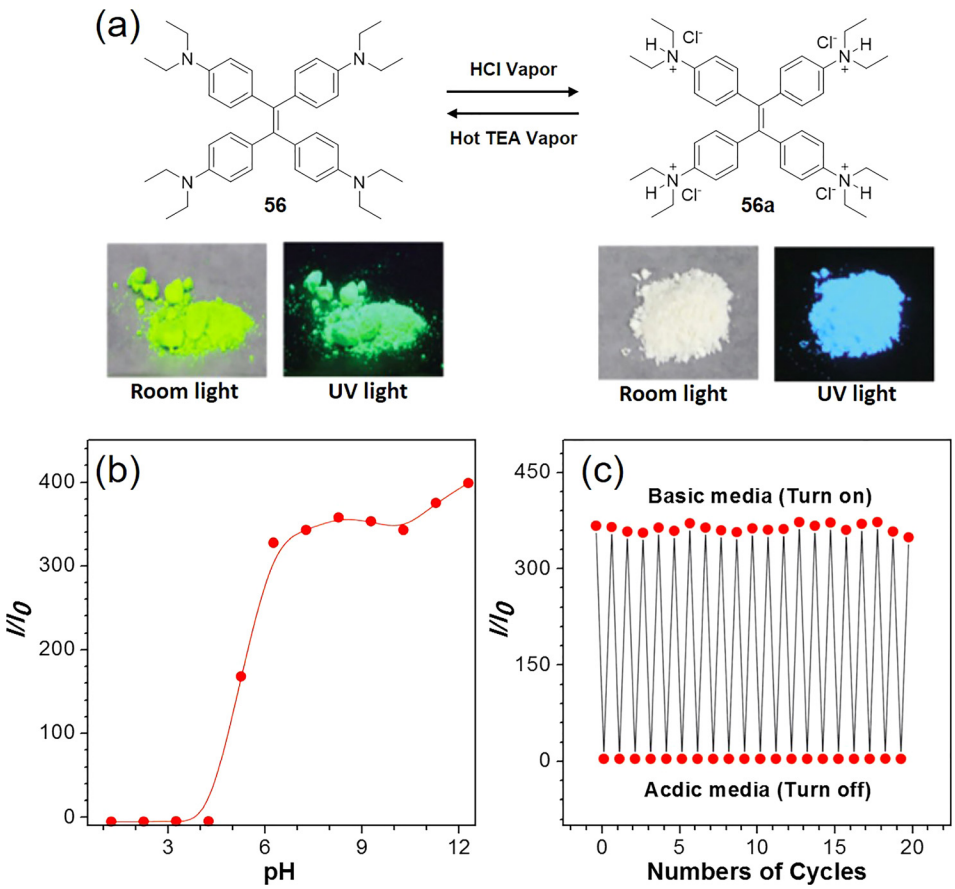

FIG. 24. (a) The structures and photographs of **56** and **56a** in powder form in room light and under UV light. (b) The plot of I/I_0 versus pH value, where I_0 is the PL intensity at pH = 1.0; (c) the reversible transformation in acidic medium (pH = 4.0, turn-off) and basic medium (pH = 10.0, turn-on), where I_0 is the PL intensity at pH = 4.0. Reproduced with permission from Wang *et al.*, J. Mater. Chem. C **3**, 9103 (2015). Copyright 2015 Royal Society of Chemistry.

vapor can return the powders to initial neutral state. To conclude this section, with proper molecular design, AIEgens are able to show smart responses to external stimuli or environmental changes. These fluorescence responses are not limited to solutions, where amorphous or crystalline AIE materials are able to switch their emission towards grinding, compression, pressuring, pH, temperature, and so on. With the rapid advances of AIE world, more advanced and smarter materials will be developed in future for various stimuli process studies.

D. Biomedical applications

Biological research area is a vast and crucially important field, where various species and numerous processes need to be monitored and investigated. Fluorescence as a versatile imaging technique with high spatial and temporal resolution is the most indispensable platform for biological applications.[124] Fluorescence imaging offers the most direct visualization of these biological species and events, in an on-site and noninvasive manner, which has shown great advantages over other modalities in the light of simplicity, high sensitivity, superior selectivity, high signal to background noise ratio, and so on. Various materials have been embedded in the biological sensing and imaging applications, including the inorganic nanoparticles, organic dyes, fluorescent proteins (FPs), etc. Inorganic nanoparticles, such as semiconducting quantum dots are well known for their high brightness and photostability but with inherently toxic heavy metal components.[124] FPs provide the most accurate and precise visualization of protein activities,[1] but they require a complex transfection process and suffer from silent gene expression and potential gene mutation issues. Organic dyes, on the other hand, have served in most biosensing and bioimaging applications, benefited from their tunable emission and feasible structure modifications. However, the ACQ effect faced by most conventional organic molecules has limited their use at high concentrations, which compromises the sensing sensitivity and imaging contrast. Exactly opposite to the ACQ fluorophores, the low emission of AIEgens as molecular species and the bright emission as nanoaggregates facilitate the design of specific light-up probes. These probes only turn on their fluorescence in response to specific biological stimuli such as protein recognition or enzymatic reaction. The low background noise also provides the opportunities for real-time continuous monitoring of biological processes with high sensitivity without washing steps. In this section, we focus on the showcase of the great performance of AIEgens in different biological applications, from sensing to imaging and therapy.

1. Bacteria sensing and imaging

Microorganisms play crucial roles in human being lives and environment, and some bacteria have been widely used in food processing, medical hygiene, or pharmaceutical industry, while other are found to be the origin of lots of human diseases.[125] The detection, imaging, and active monitoring of the bacteria activities have great implications. The specific feature of AIEgens to show their emission upon aggregate formation provides a facile approach for sensing and imaging of different types of bacteria.

Tracking of bacteria viability is of great importance in the study of disinfection efficiency, antibacterial pharmacokinetics and pharmacodynamics, and so on.[126] However, conventional methods by counting colony forming units are very laborious and often associated with underestimated results, while conventional viability dyes suffer from high toxicity and high background signal. In 2014, Tang *et al.* developed a highly emissive and photostable AIE probe, 4,4′-(1,2-diphenylethene-1,2-diyl)bis(4,1-phenylene)diboronic acid (**57**), for discrimination of live and dead bacteria.[127] Incubation with **57** for 0.5–3 h, no fluorescence can be detected from live bacteria, regardless of Gram-positive nor Gram-negative bacteria. While a short incubation time of 0.5 h can lead to bright fluorescence from dead bacteria [Fig. 25(a)]. The fluorescence intensity of **57** in the presence of dead bacteria is over 12-fold higher than that for the living ones. A series of experiments revealed that **57** was able to bind to the groove of the double-strained DNA of bacteria to give brightness but it cannot penetrate cell walls of live bacteria. For the live bacteria, the direct interaction of **57** with bacteria double-strained DNA was blocked by the presence of cell walls, leading to the isolated **57** molecules in solution. For dead bacteria, the membrane was broken, which opened the access of **57** with the protoplasm and the binding towards double-strained DNA to restrict the intramolecular motions, and hence, the bright fluorescence from dead bacteria was observed. Compared with commercial viability dyes, **57** possesses high brightness, excellent photostability, and appreciable biocompatibility, making it a suitable candidate for long-term tracking of bacterial viability.

Besides blue emitting AIE probes, AIEgens with other emission colors have also been designed for bacteria imaging, and the yellow emissive cationic TPE derivative **58** is one of such examples.[128] **58** possesses a styrylpyridinium unit and a long alkyl chain, with an emission maximum at ~580 nm. As an amphiphilic molecule, **58** dissolves well in water at low concentrations with faint emission, but it can form micelles at high concentrations with a CMC value of 20 μM. The micelles of **58** have an effective diameter of 240 nm with a polydispersity index of 0.20. Bearing two positively charged amino groups, **58** is able to bind to bacteria driven by electrostatic interactions as bacteria cell envelop is negatively charged. At a concentration of 10 μM, **58** is able to turn on its fluorescence after binding to bacteria with a very short incubation time of 10 min [Fig. 25(b)]. Benefiting from the AIE feature, the background signal from unbound **58** is very low, which does not require any washing process before imaging. Different from **57**, **58** is able to stain both dead and live bacteria. The cationic charges help facilitate the interaction with bacteria, and the long alkyl chains and the amphiphilic nature of **58** increase the intercalation and permeability into the membrane by disturbing the amphiphilic phosphatidyl lipid arrangement. The binding with and insertion into bacteria membrane lead to distinguishable brightness on the bacteria.

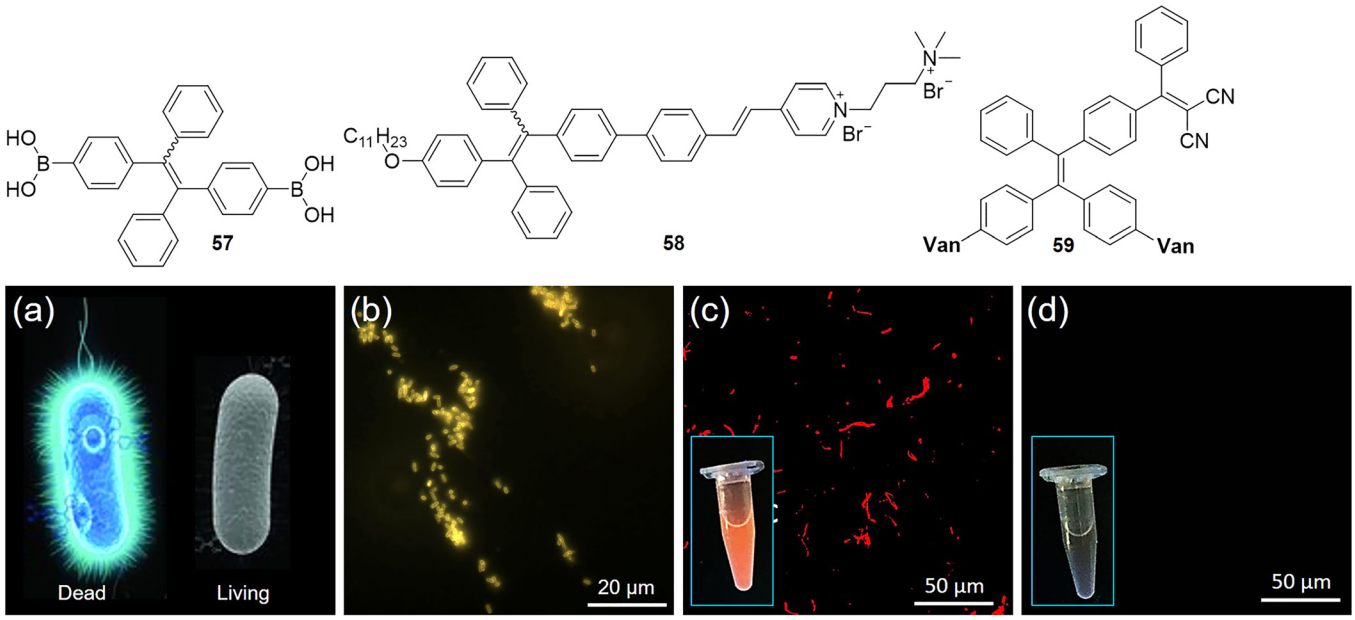

FIG. 25. Representative examples of AIEgens for bacteria sensing and imaging. (a) Schematic illustration of discrimination of dead/live bacteria by **57**. (b) Fluorescence image of *E. coli* stained by **58**. Reproduced with Zhao *et al.*, Adv. Healthcare Mater. **3**, 88 (2014). Copyright 2014 Wiley-VCH. (c) and (d) Confocal images of (c) *B. subtilis* and (d) *E. coli* stained by **59**, insets show photographs of **59** stained bacteria suspension in the presence of graphene oxide under a UV lamp. Van: vancomycin. Reproduced with permission from Feng *et al.*, Chem. Commun. **51**, 12490 (2015). Copyright 2015 Royal Society of Chemistry.

To address the targeting ability towards specific bacteria, very recently, Liu *et al.* developed a red emissive AIE probe (**59**) for fluorescence imaging and naked eye detection of Gram-positive bacteria.[129] Vancomycin (Van) as a glycopeptide antibiotic has a very high binding affinity towards the peptidoglycan sequence N-acyl-D-Ala-D-Ala presented on Gram-positive.[130] The probe, **59** (Fig. 25), comprising two Van groups and a core TPE derivative, shows negligible red fluorescence in aqueous solution, benefiting from the excellent solubility of Van groups. In the presence of Gram-positive bacteria without Van resistance such as *Bacillus subtilis*, **59** is able to turn on its red fluorescence centered at 650 nm, while **59** leaves Gram-negative bacteria intact with negligible signal [Figs. 25(c) and 25(d)]. In addition, **59** also possesses some binding affinities towards Van resistant strains such as *Enterococcus faecium* (Van A) and *Enterococcus faecalis* (Van B), which also exhibit fluorescence turn-on in the presence of both bacteria strains. Different from conventional bacterial staining dyes, which have intrinsic fluorescence before bacteria labelling, the negligible fluorescence of **59** at initial stage and largely enhanced brightness after binding provide a unique opportunity for direct naked eye detection of Gram-positive bacteria. The naked eye detection was performed at a relatively high **59** concentration of 20 μM, with the help of graphene oxide to further reduce the background signal. *B. subtilis* aqueous suspension provides bright red emission, while *Escherichia coli* suspension does not emit any light [inset, Figs. 25(c) and 25(d)]. On the other hand, Van A and Van B also exhibit a different degree of red fluorescence. **59** also exhibits excellent photosensitizing ability even in the aggregate state after binding to bacteria, which makes it an excellent antibacterial agent as compared to conventional photosensitizers which suffer from reduced reactive oxygen species generation upon aggregation.[131]

2. Cellular organelle staining

Organelles play pivotal roles in cell life and death, and their malfunctions could lead to serious diseases. Fluorescence imaging that can provide images at nanometer scales with high spatial and temporal resolutions appears to be the best imaging modalities for imaging and monitoring the activities of cell organelles. The development of AIEgens has further enforced the powerful potential of fluorescence imaging, in terms of brightness, biocompatibility, and photostability. The unique feature of AIE based probes to turn on its fluorescence also contributes to the new emerging biological areas. Compound **60** is one of such AIEgens for labelling of cell cytoplasm.[132] **60** was synthesized from TPE by simply attaching β-cyclodextrin (CD) to one phenyl ring of TPE. The β-CD moiety can largely inhibit the active intramolecular rotations of TPE, and as a consequence, **60** is very emissive with a η of ~16.0% even in isolated molecular state, and the high brightness is also inherited by its nanoaggregates which formed naturally when dispersed in aqueous solution. The **60** nanoaggregate was able to penetrate the cell membrane and light up the interior space of cells upon incubation with HeLa cells [Fig. 26(a)]. Moreover, **60** can specially label the cytoplasm of HeLa cells.

Cell membrane is a protective lipid bilayer that segregates cell interior space and regulates the substance influx and efflux. Considering its vital functions in cell adhesion, nutrient transportation and cell signaling, it is of great importance to visualize the membrane and its related events.[133] Currently, only few commercial organic dyes are available for cell membrane staining, and thereby, development of

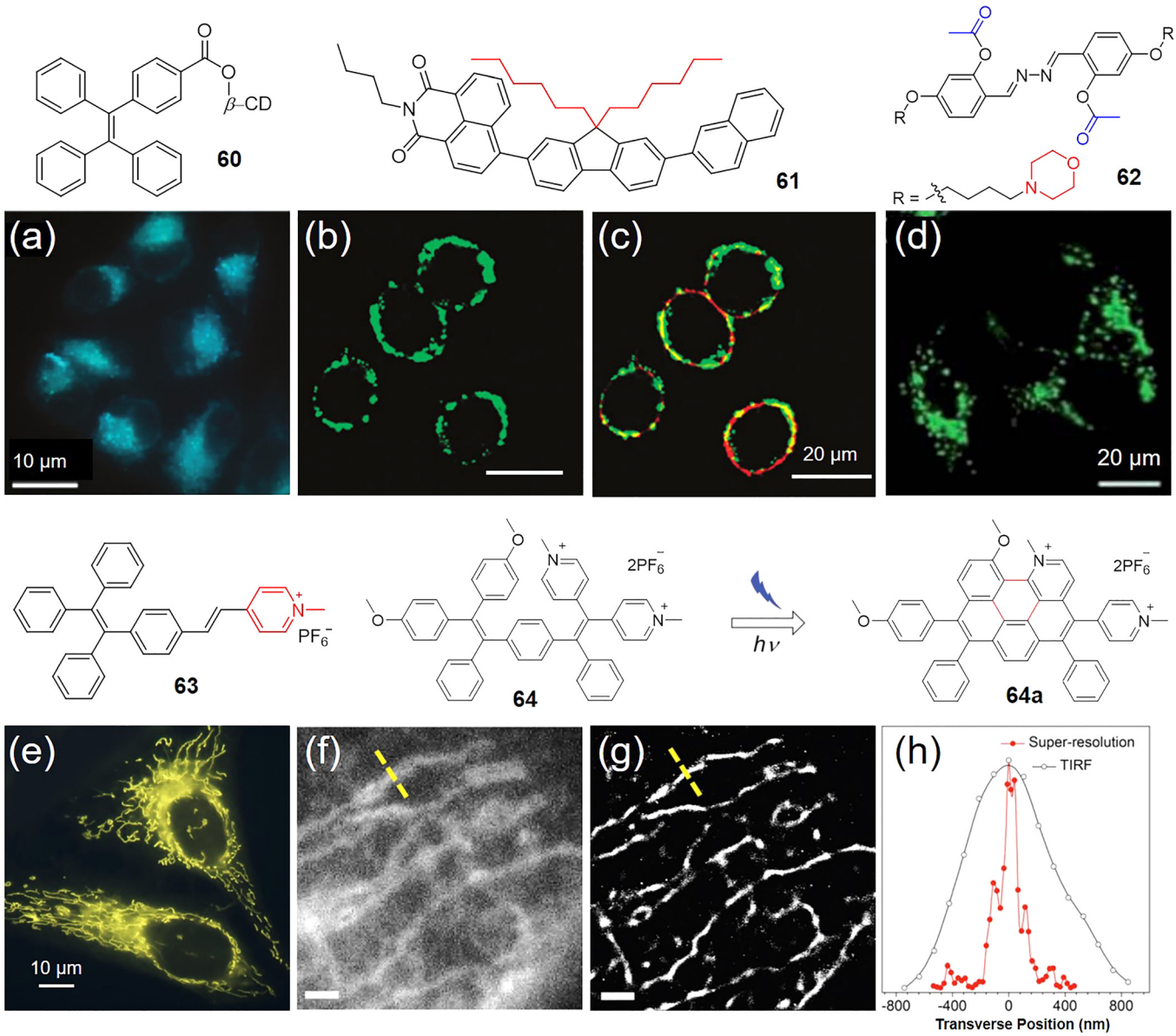

FIG. 26. Representative examples of AIEgens for cellular organelle staining. (a) Confocal image of HeLa cell cytoplasm stained by **60**. Reproduced with permission from Liang *et al*., Chem. Commun. **50**, 1725 (2014). Copyright 2014 Royal Society of Chemistry. (b) and (c) Confocal images of the HepG2 cell membrane stained by (b) **61** and (c) co-stained by **61** and commercial membrane staining dye Dil. Reproduced with permission from Li *et al*., Chem. Commun. **49**, 11335 (2013). Copyright 2013 Royal Society of Chemistry. (d) Confocal image of MCF-7 cell lysosomes stained by **62**. Reproduced with permission from Gao *et al*., J. Mater. Chem. B **2**, 3438 (2014). Copyright 2014 Royal Society of Chemistry. (e) Fluorescence image of HeLa cell mitochondria stained by **63**. Reproduced with permission from Zhao *et al*., J. Mater. Chem. C **1**, 4640 (2013). Copyright 2013 Royal Society of Chemistry. (f) Epifluorescence image and (g) super-resolution image of HeLa cell mitochondria structures stained by **64**. (h) Transverse profiles of the single mitochondrion along the yellow dotted line marked in the images (f) and (g). Reproduced with permission from Gu *et al*., Adv. Mater. **28**, 5064 (2016). Copyright 2016 Wiley-VCH.

membrane staining dye is of practical importance. Very recently, Li *et al*. developed an AIE probe (**61**) derived from 1,8-naphthalimide for specific labelling of cell membranes with excellent photostability and low cytotoxicity.[134] **61** exhibits a bright green emission in solid state with an absolute η of 73.0%. Due to its inherent high hydrophobicity, **61** forms nanoparticles in aqueous solution with an average diameter of 150 nm. **61** nanoparticles show very poor cellular uptake and they have a tendency to localize at the cell membrane, where intense green emission is detected on the membrane, but not in the cytoplasm and nucleus region [Fig. 26(b)]. Colocalization experiments with commercially available membrane staining dye Dil [Fig. 26(c)] further confirmed the exclusive staining of cell membranes. **61** exhibits much higher photostability as compared to Dil where continuous laser scanning for 200 s can only lead to less than 12% signal loss for **61** but over 65% loss for Dil. Furthermore, **61** stays on HepG2 cell membranes and emits strong green emission even after passage for 4 days. Together with the very low toxicity, **61** represents an excellent noninvasive membrane staining and tracking probe with high photostability.

Lysosomes are cell membrane-bound organelles, which are hydrolytic enzyme containing spherical vesicles and

responsible for cellular homeostasis, membrane repair as well as cell signaling, etc. Visualization of their morphology changes and mapping their intracellular distribution have great implications in studying their functional activities. However, the accumulation of conventional fluorogens in lysosomes often leads to self-quenching due to the high localized concentration. To visualize lysosome and monitor the lysosome esterase activity, Liu *et al*. developed a specific light-up probe based on AIE and ESIPT in 2014.[135] This probe (**62**) comprises a salicyladazine fluorophore, two esterase reactive acetoxyl groups, and two lysosome-targeting morpholines. The acetyl group (blue color) of **62** is cleaved by esterase which leads to the formation of hydrogen bond and activates the ESIPT and AIE processes in aqueous medium to show bright fluorescence centered at 532 nm with a large Stokes shift over 176 nm. **62** shows a fast fluorescence turn-on response towards esterase with excellent selectivity in solution. Upon incubation with MCF-7 cells, the fluorescence from **62** provided a discrete labelling pattern of lysosome [Fig. 26(d)], which showed very good overlapping with LysoTracker Red, revealing its high specificity for lysosomes in intracellular environment. Continuous laser scanning revealed a high photostability of **62** as compared to LysoTracker Red, where signal losses of 20% and 70% were observed for **62** and LysoTracker Red, respectively, after 8 min scanning. In addition, they also verified the critical role of morpholine in targeting lysosome, where the control group without morpholine conjugation showed low cellular uptake, low signal contrast, and no specificity. With this stable and bright probe, the spatial and temporal distribution and slight movement of lysosomes have been clearly visualized and tracked.

Mitochondrion, the powerhouse of the cells, plays prominent functions in cellular metabolic activities, such as regulating cell cycles, growth, and cellular differentiation.[136] The dysfunction of mitochondrion leads to numbers of diseases, such as cardiac dysfunctions, heart failure, and Alzheimer's disease. Direct visualization and active tracking of mitochondrion morphology changes are able to provide valuable insights for apoptosis and degenerative conditions. To achieve this goal, fluorescent dyes should have high specificity and good photostability. Considering the excellent photostability and largely intensified brightness upon enrichment at the targeted site, AIE based mitochondrion probes are promising candidates for mitochondrion imaging and tracking. The mitochondrion targeting AIE probe (**63**) was synthesized through the reaction between 1,4-dimethylpyridinium iodide and 4-(1,2,3-triphenylvinyl)benzaldehyde.[137] **63** is a typical AIEgen, which shows very weak fluorescence in THF solution, but strong emission in both amorphous and crystalline states. Living HeLa cells after incubation with 5 μM **63** for 15 min show strong distinct yellow emission in mitochondria [Fig. 26(e)], which is further verified by co-staining experiments with commercial MitoTracker Red. Continuous laser scanning was used to evaluate the photostability of **63**, which showed bright emission from distinct mitochondria patterns after 180 s scanning, while the emission for MitoTracker Red was completely bleached under the same conditions.

Encouraged by the exciting performance of AIEgens for organelle staining, more dedicated efforts from different aspects have been devoted to this area. One notable example is a photoactivatable fluorescence turn-on AIE probe **64** with mitochondrion targeting for localization super-resolution microscopy.[138] The super-resolution imaging technique breaks the light diffraction limits ($\sim$200 nm for most fluorescence microscopies), which has attracted great research interest in biological science recently. It increases the imaging resolution to nanometer scale, which provides a powerful tool for visualization of intracellular structures, especially the morphologies of different organelles. One of the promising super resolution imaging techniques is single-molecular localization microscopy, such as stochastic optical reconstruction microscopy (STORM), which relies on fluorescence switching between bright and dark states. The brightness, on/off signal ratio, and the specific targeting ability of fluorogens are the three key factors affecting the imaging quality. Due to D-A (methoxy group as donor, 1-methylpyridinium group as acceptor) configuration, the aggregate of **64** is very bright in non-polar solvent (e.g., toluene), but it exhibits very weak emission in aqueous media with high polarity.[138] **64** can undergo a novel photoactivation mechanism of photocyclodehydrogenation to form **64a**, during which its brightness is largely intensified (Fig. 26) with an enhancement factor of over 160-fold as compared to **64**. Further treating the probe with appropriate power could photobleach the molecules to dark state. The fluorescence switchable ability makes **64** promising for super resolution imaging. The intracellular location of **64** was first evaluated before applying it for super-resolution imaging. HeLa cells labelled by **64** show very weak fluorescence, and applying 10 s of light irradiation for photoactivation reaction could lead to largely intensified emission on the mitochondria of HeLa cells, demonstrating rapid and efficient in-cell turn-on processes as well as excellent mitochondria specificity. The epifluorescent image of mitochondria was first acquired prior to STORM imaging, which showed totally blurred structures with low resolution [Fig. 26(f)]. On the contrary, the STORM image reconstructed from the bright and dark states displayed a clearer mitochondrial morphology with much more detailed mitochondria structures [Fig. 26(g)]. The transverse profiles revealed a full-width at half-maximum of 104.5 nm and 697.1 nm for STORM image and epifluorescence image, respectively [Fig. 26(h)]. The unique photoactivation behavior of **64** makes it a promising probe for super-resolution imaging with much improved resolution than traditional fluorescence techniques.

3. Cell tracking

Continuous tracking of cell activities by fluorescence in a non-invasive manner over a long period of time is pivotal to extract critical spatiotemporal cellular information of physiological displacement, translocation, and the fate of cancer and stem cells.[139] This information facilitates the understanding of cancer or stem cell development and intervention, providing insights for basic oncological researches and the development of preclinical cell based therapies.

Fluorescent proteins have been widely used for cell tracking. However, virally introduce fluorescent protein gene into cell genome or non-virally transfecting green fluorescent protein (GFP) in cytoplasm have their own caveats, such as potential random mutations for the former, low and varied GFP expression efficiencies for different cells for the latter. Direct labelling with organic fluorescent materials is therefore a fairly straightforward approach. As fluorescence decreases upon cell division, fluorescent cell trackers should possess excellent cellular uptake, high brightness and good biocompatibility. In this regard, fluorescent nanoparticles with excellent cellular retention as compared to their small molecular counterparts are one of the most suitable solutions. Different from conventional ACQ dyes, which suffer from decreased or diminished fluorescence upon encapsulation into nanoparticles, the AIE based nanoparticles show much stronger and stable emission making them the excellent candidates for cell tracking.

Liu's group has been actively involved in the development of cell trackers with multiple colors to facilitate different biological researches.[140–143] They developed a general and simple technique to fabricate ultra-bright AIE dots for cell tracking applications. One of the good examples is the AIE cell tracker using the green emissive AIEgen **65** [Fig. 27(a)] as the core.[140] Biocompatible block copolymer lipid PEG such as 1,2-distearoyl-sn-glycero-3-phosphoethanolamine-*N*-[methoxy(polyethylene glycol)–2000] (DSPE-PEG_{2000}) and 1,2-distearoyl-sn-glycero-3-phosphoethanolamine-*N*-[amino(-polyethylene glycol)–2000] (DSPE-PEG_{2000}-Mal) were used as the matrices to encapsulate AIEgens to ensure the compact packing and high loading efficiency of these molecules into AIE nanoparticles. Once these nanoparticles have average sizes of ~30 nm, they were further termed as AIE dots. The surface maleimide groups on the AIE dots are able to facilitate efficient surface conjugation with cell penetration peptide HIV-1 Tat (RKKRRQRRRC) to yield **65**-Tat AIE dots [Fig. 27(a)]. These AIE dots exhibit bright green emission centered at 547 nm, with a very high η of 63.0%. The **65**-Tat AIE dots show very high cellular uptake with nearly 100% cell labelling efficiencies towards different animal and human cell lines, which outperform the non-viral GFP transfection approach in cell labelling, as GFP expression efficiencies varied significantly from 1.3% to 68.7% among different cells. When using human embryonic kidney 293T (HEK-293T) cells, which have the highest GFP expression for cell tracking, **65**-Tat AIE dots could track its activity up to 10 days. The cell labelling rate was kept above 90% on day 5 and over 70% on day 7 while nearly no cell gave GFP expression at day 5 post infection or incubation [Fig. 27(b)]. This clearly indicated that the **65**-Tat AIE dots could be efficiently internalized into

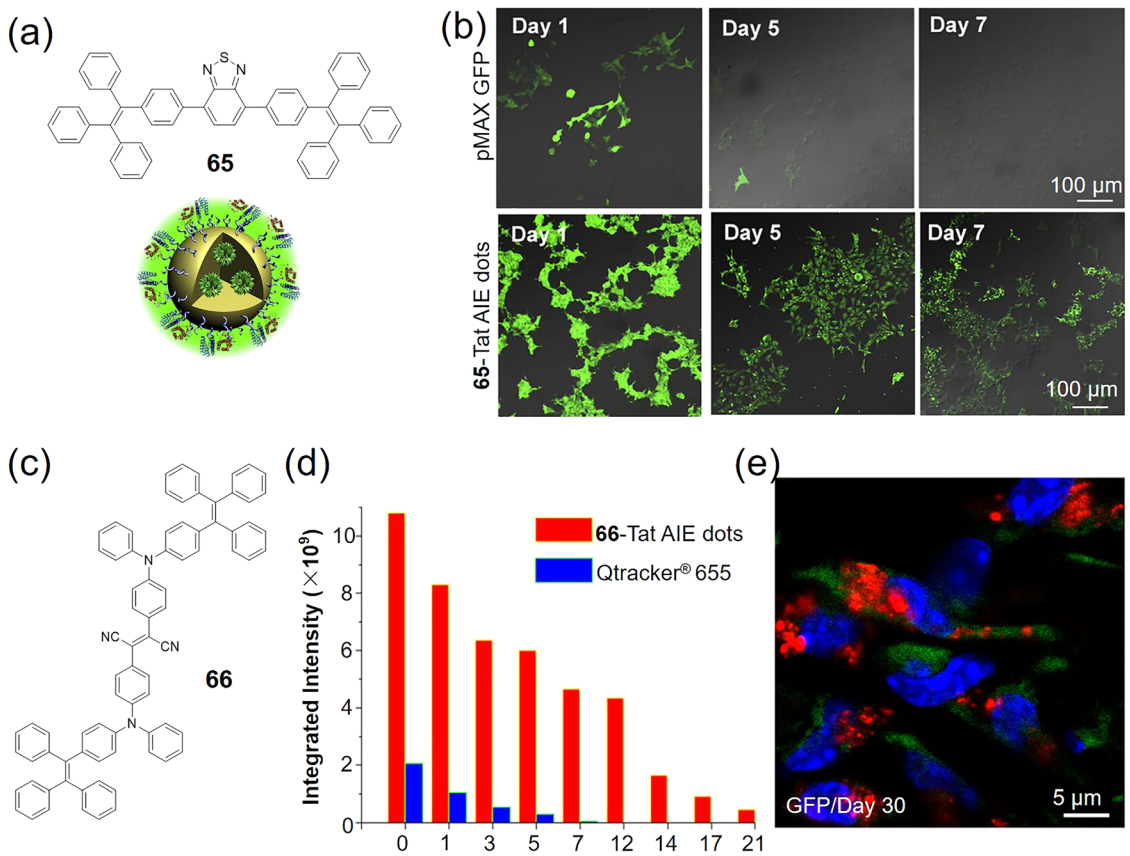

FIG. 27. Representative examples of AIEgens for cell tracking. (a) Chemical structure of **65** and schematic illustration of **65**-Tat AIE dots. (b) Confocal images of HEK-293T cells labelled by pMAX-GFP (upper) and **65**-Tat AIE dots (lower) at different days of post-incubation. Reproduced with permission from Feng *et al.*, Biomateirals **35**, 8669 (2014). Copyright 2014 Elsevier Inc. (c) Chemical structure of **66**. (d) The integrated PL intensities of the region of interest at tumor sites labelled by **66**-Tat AIE dots or Qtracker® 655, on designated days post cell injection. Reproduced with permission from Li *et al.*, Sci. Rep. **3**, 1150 (2013). Copyright 2013 Nature Publishing Group. (e) Tracking of ADSCs labelled by **66**-Tat AIE dot *in vivo* at single-cell resolution. Reproduced with permission from Ding *et al.*, ACS Nano **8**, 12620 (2014). Copyright 2014 American Chemical Society.

cells and passed to daughter cells during proliferation, which offered a powerful cell tracker that can uncover some biological events that cannot be visualized before.

For *in vivo* cell tracking, far-red (FR)/NIR emission is highly desired to avoid the interference from autofluorescence as wells as to have a deep tissue penetration depth. To facilitate this objective, Liu and Tang *et al.* also developed FR/NIR emissive AIE-Tat dots by using **66** as the emissive AIE core [Fig. 27(c)].[143] The obtained **66**-Tat dots show an absorption peak at 511 nm and an emission maximum located at 671 nm with a tail extending to 900 nm. The **66**-Tat dots have a high η of 24.0%, which is over 10-fold brighter than commercial Qtracker 655 with similar emission maximum. Moreover, **66**-Tat dots exhibit stable fluorescence under continuous laser scanning while Qtracker 655 blinks. **66**-Tat AIE dots are able to track the MCF-7 cell activity over 12 generations while Qtracker 655 can only track for 5–6 generations in *in vitro* experiments. When using **66**-Tat AIE dots to track the growth of C6 glioma cells in mouse, the fluorescence could be tracked for 21 days, while the fluorescence of Qtracker 655 vanished at day 7 [Fig. 27(d)]. Encouraged by the superior cell tracking ability of AIE dots, **66**-Tat AIE dots were further applied for noninvasive tracking of stem cells and their regenerative capability.[144] Stem cells that can differentiate into specialized cells are noted with regenerative capability for tissue engineering.[145] Monitoring the cell fate and regenerative therapy of adipose-derived stem cells (ADSCs) is of great importance for stem cell therapy development. **66–**Tat AIE dots also outperform Qtracker 655 in tracking of ADSCs. At day 30 after ADSC administration, the red fluorescence from **66**-Tat AIE dots overlaps very wells with green fluorescence of GFP gene transplanted ADSCs [Fig. 27(e)], indicating the high accuracy of AIE-Tat dots for *in vivo* tracking of ADSCs. With the help of bright red fluorescence from the AIE-Tat dots, it reveals that ADSCs engaged in blood vessel formation *via* formatting vascular structures. Along with development of AIEgens, more and more AIE based cell trackers have been developed with excellent performance.[16,141,142,146,147] To conclude, AIE-Tat dots are simple, safe, and effective cell labelling and tracking reagents, which have shown remarkable advantages over current commercially available cell trackers.

4. Vascular imaging

Blood vessels serve as a physical barrier and function in a highly responsive dynamic manner, allowing the regulation of the transport rate of solutes, macromolecules, and cells between blood and tissue.[148,149] The loss of barrier functions or malfunction of blood vessel is commonly associated with neurological disorders.[150] Two-photon fluorescence imaging (TPFI) has been one of the most widely used techniques for the visualization of blood vascular networks. Using DSPE-PEG_{2000} as the matrix and **65** as the core, the developed **65** AIE dots are an excellent TPFI material for visualization of blood vascular networks.[151] Besides the ultra-high brightness under one-photon excitation, the AIE dots based on **65** also show high two-photon cross section (σ) and two-photon action cross section ($\sigma\eta$) of 10.2×10^4, and 6.3×10^4 GM, respectively. Three intravital TPFI models: brain [Fig. 28(a)], bone marrow [Fig. 28(b)], and ear [Fig. 28(c)] were used to evaluate the TPFI imaging capability of **65** AIE dots

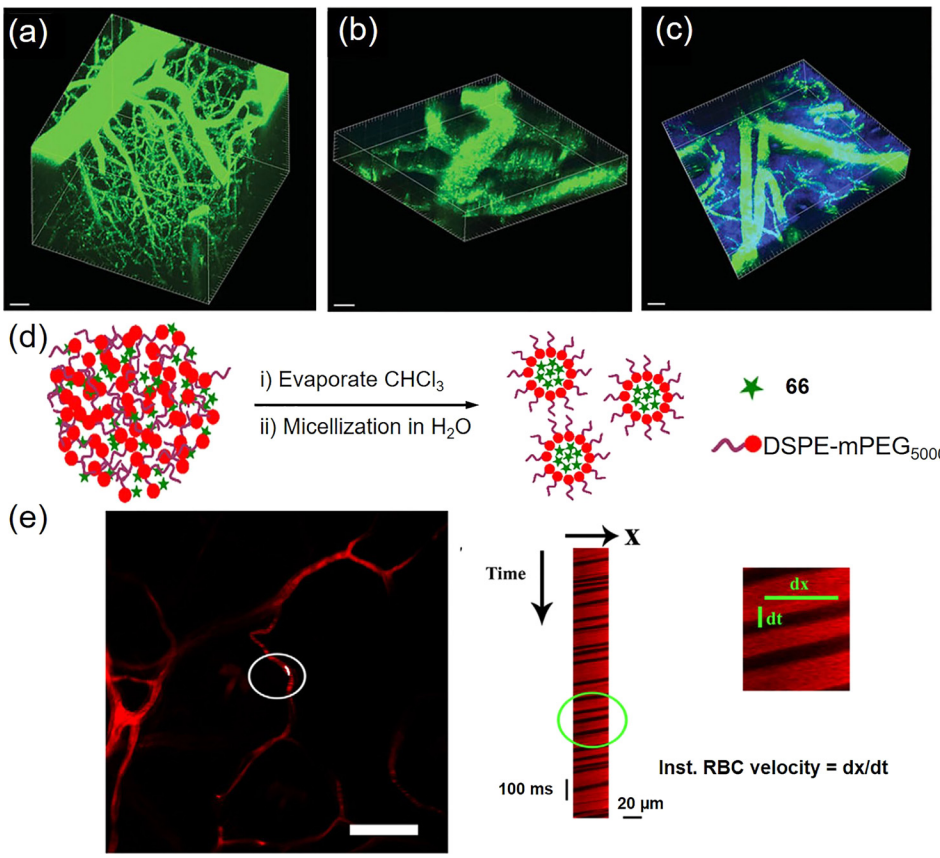

FIG. 28. Representative examples of AIEgens for vascular imaging. (a) Brain, (b) bone marrow, and (c) ear blood vessels stained by **65** AIE dots. Reproduced with permission from Ding *et al.*, Adv. Mater. **25**, 6083 (2013). Copyright 2013 Wiley-VCH. (d) Schematic illustration of **66** AIE dots fabrication. (e) Line scan along capillaries of a mouse brain was used to observe RBC flow and determine its instantaneous velocity (dx/dt) with two-photon confocal microscope. Scale bar: 100 mm. Reproduced with permission from Wang *et al.*, Sci. Rep. **4**, 4279 (2014). Copyright 2014 Nature Publishing Group.

for two-photon real-time blood vascular visualization. Prior to AIE dot injection, almost no fluorescence in the range of 542 ± 27 nm was observed upon excitation at 800 nm. Upon intravenous administration, the intrinsic fluorescence from **65** AIE dots immediately lights up all the vascular networks, where not only the major blood vessels but also the smaller capillaries in the pia mater could be clearly observed by the intense green fluorescence from the AIE dots. **65** AIE dots exhibit much better blood vascular retention as compared to Evans Blue, the most widely adopted vascular labelling reagents. The average fluorescence intensity from AIE dots stained blood vessels is around 3-fold and 20-fold brighter than those labelled by QD655 and Evan Blue, respectively.

Meanwhile, FR/NIR emissive AIEgen **66** was also selected for the development of AIE dots for *in vivo* two-photon visualization of vascular network and evaluation of red blood cell (RBC) velocity.[152,153] As shown in Fig. 28(d), the AIE-dot aqueous suspension was prepared by a micellization method. The chloroform solution of DSPE-mPEG$_{5000}$ and **66** was first sonicated to prepare a homogeneous solution, which was further dried using a vacuum rotary evaporator. The obtained red film was subjected to water addition and sonication to induce micelle formation. The obtained AIE dots and nanoparticles had a size range of 20–180 nm depending on feeding ratio of **66**. Upon intravenous injection into mice, a bright two-photon fluorescence signal from ear blood vessels can be detected under femtosecond (100 fs) laser excitation at 800 nm, while no emission signal in the blood vessels can be obtained upon one-photon excitation at 543 nm. The diminished fluorescence signal under one photon excitation is mainly due to the absorption/scattering loss of 543 nm laser in skin/blood, which provides direct evidence of the large improvement in imaging depth of the TPFI. Benefited from their PEG shells, the injected AIE dots cannot internalize into red blood cells flowed in the blood plasma, and individual red blood cells appeared as shadows flowing with the fluorescent plasma during the fluorescence imaging [Fig. 28(e)], which provides a facile approach for measuring red blood cell (RBC) velocity.

Multiphoton fluorescence is a non-linear optical (NLO) process where multiple photons can be simultaneously absorbed to generate the excited state to provide fluorescence.[154] He and Tang *et al.* recently reported the three-/four-photon excited luminescence (3PL/4PL) of AIEgens using **66** as an example.[155] Although **66** in the chloroform/toluene mixture only shows 3PL under 1560 nm femtosecond laser excitation, its solid state simultaneously exhibits 3PL and third harmonic generation (THG) spectra upon excitation by a 1560 nm femtosecond laser [Fig. 29(a)]. In addition, the 3PL intensity showed a linear relationship with the intensity of the THG, both are proportional to the femtosecond laser power. The THG photons directly generated from femtosecond excitation could be reabsorbed by **66** to produce the 3PL signal [Fig. 29(b)]. The **66**-doped-silica nanoparticles possess both THG and 3PL signals, making it a nanoprobe for multimodal NLO imaging. HeLa cells treated by **66**-doped-silica nanoparticles showed green (THG) and red (3PL) emission, which overlap well with each other [Figs. 29(c) and 29(d)]. The bright 3PL signal also makes **66** AIE nanoparticles an excellent reagent for visualization of the vascular network in mouse brain with imaging depth up to 550 μm [Fig. 29(e)]. It should be noted that **66** was also capable to generate 4PL as well as THG under 1950, 2010, or 2070 nm femtosecond laser excitation, where 4PL and THG are two independent NLO effects as the THG photons of 650, 670, and 690 nm are not able to be reabsorbed to produce fluorescence. The high brightness, excellent photostability and high biocompatibility, together with the capability to be excited under two-photon or multiphoton excitation clearly demonstrate the superiority of AIE dots as vascular labelling and tracking reagents.[153,156–159]

5. Theranostics

Nanomaterials with multidisciplinary and interdisciplinary functions have become one of the most promising

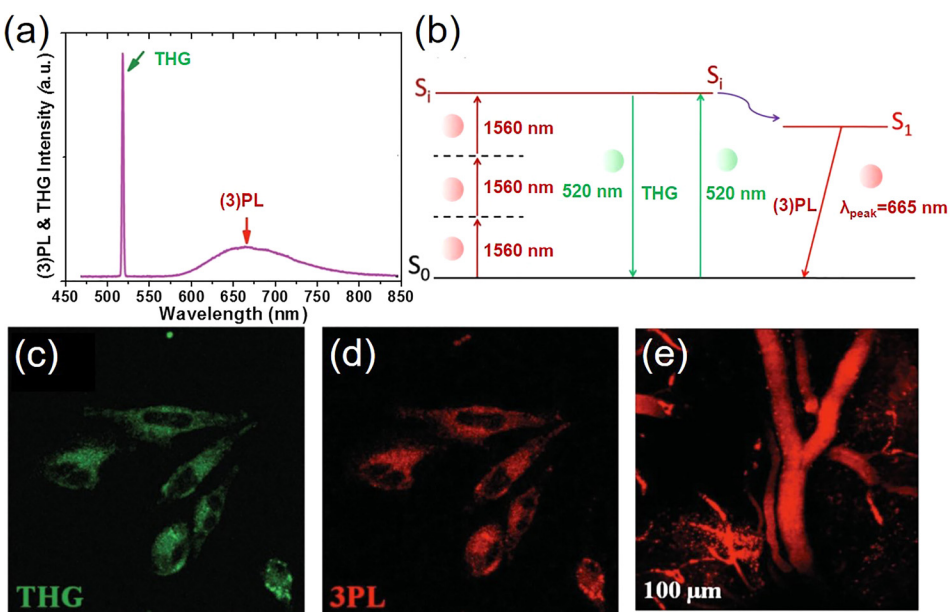

FIG. 29. (a) Simultaneous three photon excited luminescence (3PL) and third harmonic generation (THG) spectra from **66** solid (excited by a femtosecond laser at 1560 nm). (b) Diagrams showing the proposed excitation mechanisms of THG and THG-induced 1PL. (c) THG and (d) 3PL images of HeLa cells which were treated with **66** AIE nanoparticles for 2 h. (e) 3PL microscope image of mouse brain blood vessels (intravenously injected with **66** dots) at an imaging depth of 100 μm. Reproduced with permission from Qian *et al.*, Adv. Mater. **27**, 2332 (2015). Copyright 2015 Wiley-VCH.

technologies for cancer diagnosis and therapy. These nanomaterials provide a multifunctional platform that allows simultaneous diagnosis and therapy, which is known as theranostics.[160,161] The combination of diagnosis and therapeutics in one system enables the detection of targets, monitoring bio-distribution of drug carrier as well as the evaluation of therapeutic responses.[162,163] So far, most of the AIEgens used in sensing and imaging show emission color or brightness changes under different environment.[128,134,135,140,141,143,144,146,164,165] In this section, we discuss the great opportunities of multifunctional AIEgens in the development of future theranostic platforms.

In principle, fluorescence is produced when the fluorogens undergo radiative dissipation from singlet excited states to ground state. The exciton can also undergo the intersystem crossing (ISC) process to triplet excited states, which can either produce phosphorescence or react with surrounding molecules or oxygen to produce radicals or singlet oxygen species ($^1O_2$).[166] Utilizing photosensitizers (PSs) to produce $^1O_2$ for cancer therapy is known as photodynamic therapy (PDT). However, conventional PSs suffer from ACQ effects, where both fluorescence and $^1O_2$ production are dramatically decreased when the PSs are in the aggregate state,[167] making it more challenging for efficient PDT and the visualization of PS location. Through elegant molecular design, the photophysical properties of AIEgens can be fine-tuned, which not only provide distinguishable emissions from visible to FR/NIR region, but also render them with photosensitizing ability. Fortunately, opposite to traditional PSs, in the aggregate state, the non-radiative pathway of AIEgens is largely blocked, which promotes both the radiative pathway and ISC process. As a consequence, AIE-based PSs are able to produce both bright emission and efficient $^1O_2$ for image-guided PDT.

Since the discovery of AIEgens as photosensitizers, their applications in image-PDT have attracted great research interest. One of the early examples is the study reported by Liu *et al.*, with 2-(2,6-bis((*E*)-4-(phenyl(4-(1,2,2-triphenylvinyl)-[1,10-biphenyl]-4-yl)amino)styryl)-4H-pyran-4-ylidene)malononitrile (**67**) [Fig. 30(a)] as the AIE photosensitizer.[168] **67** shows AIE characteristics. The dual functional AIE dots were synthesized *via* a modified nanoprecipitation approach, where the dot surface was conjugated with cyclic Arg-Gly-Asp (cRGD) tripeptide for selective targeting integrin overexpressed cancer cells. The **67**-cRGD dots have an average size of 32 nm with a low polydispersity of 0.12. Using 1,3-diphenylisobenzofuran (DPBF) as the $^1O_2$ indicator, the **67**-cRGD dots show efficient $^1O_2$ generation in solution even with a very short light irradiation of 1 min. **67**-cRGD dots can be exclusively uptaken by MDA-MB-231 cells as evidenced by the intense red emission inside the cytoplasm [Fig. 30(b)]. In addition, **67**-cRGD dots can also efficiently generate $^1O_2$ in intercellular environment as indicated by the strong green fluorescence in cytoplasm from the cellular ROS indicator dichlorofluorescein diacetate (DCF-DA) [Fig. 30(c)]. Among the tested cell lines, **67**-cRGD dots only show obvious toxicity towards MDA-MB-231 cells under light irradiation with a half-maximal inhibitory concentration (IC_{50}) of 1.5 μg/ml, while the

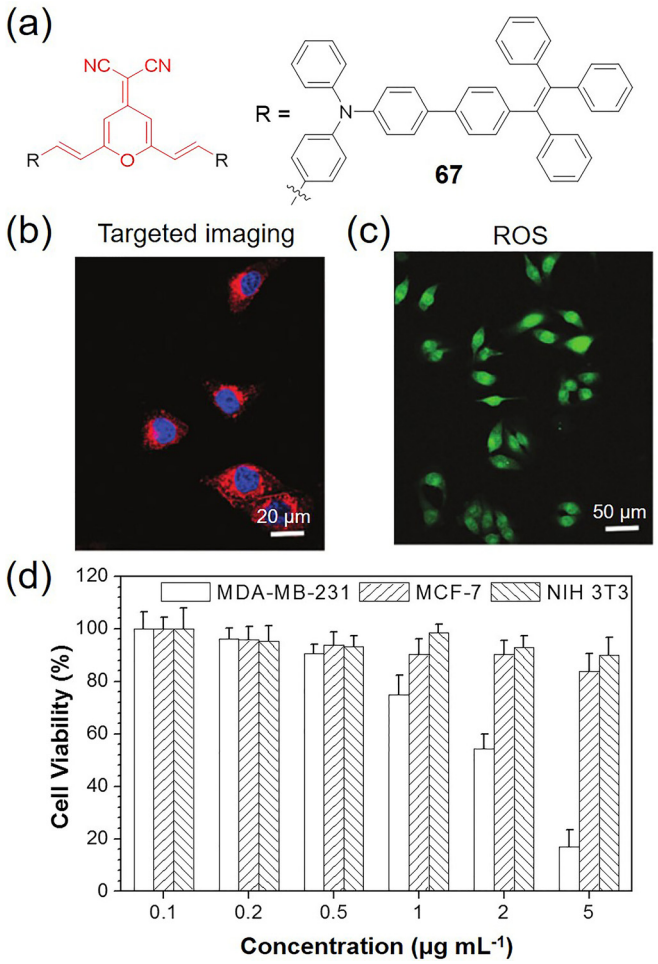

FIG. 30. (a) Chemical structure of **67**. (b) Confocal image of MDA-MB-231 cells treated with **67**-cRGD dots. (c) Detection of intracellular ROS production by dichlorofluorescein diacetate (DCF-DA) in MDA-MB-231 cells after incubation with **67**-cRGD dots followed by light irradiation. (d) Viabilities of MDA-MB-231, MCF-7 and NIH-3T3 cells in the presence of **67**-cRGD dots with light irradiation. Reproduced with permission from Yuan *et al.*, Chem. Commun. **50**, 8757 (2014). Copyright 2014 Royal Society of Chemistry.

control cells of MCF-7 and NIH-3T3 exhibited high cell viability [Fig. 30(d)]. It should be noted that **67**-cRGD dots show negligible toxicity to all the cells in the dark. AIE PS dots thus represent a simple and flexible approach for image-guided PDT.

As $^1O_2$ production results from triplet excited state, improving the ISC process by reducing singlet-triplet energy gap (ΔE_{st}) should promote the triplet excited state generation. Recently, Liu *et al.* reported a simple strategy to improve photosensitizing ability of AIEgens by fine-tuning the HOMO-LUMO distribution and reducing the ΔE_{st} to favor $^1O_2$ production.[169] Based on the TPE core, a series of AIEgens with different energy acceptors were designed and synthesized to tune the HOMO-LUMO levels [Fig. 31(a)]. These three AIEgens show a decreased ΔE_{st} value from 0.48 eV for **68**, 0.35 eV for **69**, and 0.27 eV for **70**, respectively. Along with the decrease in the ΔE_{st} values, the photosensitizing ability is largely enhanced, which is evidenced by the decomposition of an $^1O_2$ indicator, 9,10-anthracenediyl-bis(methylene) dimalonic acid. With the smallest ΔE_{st}, **70** shows the quickest

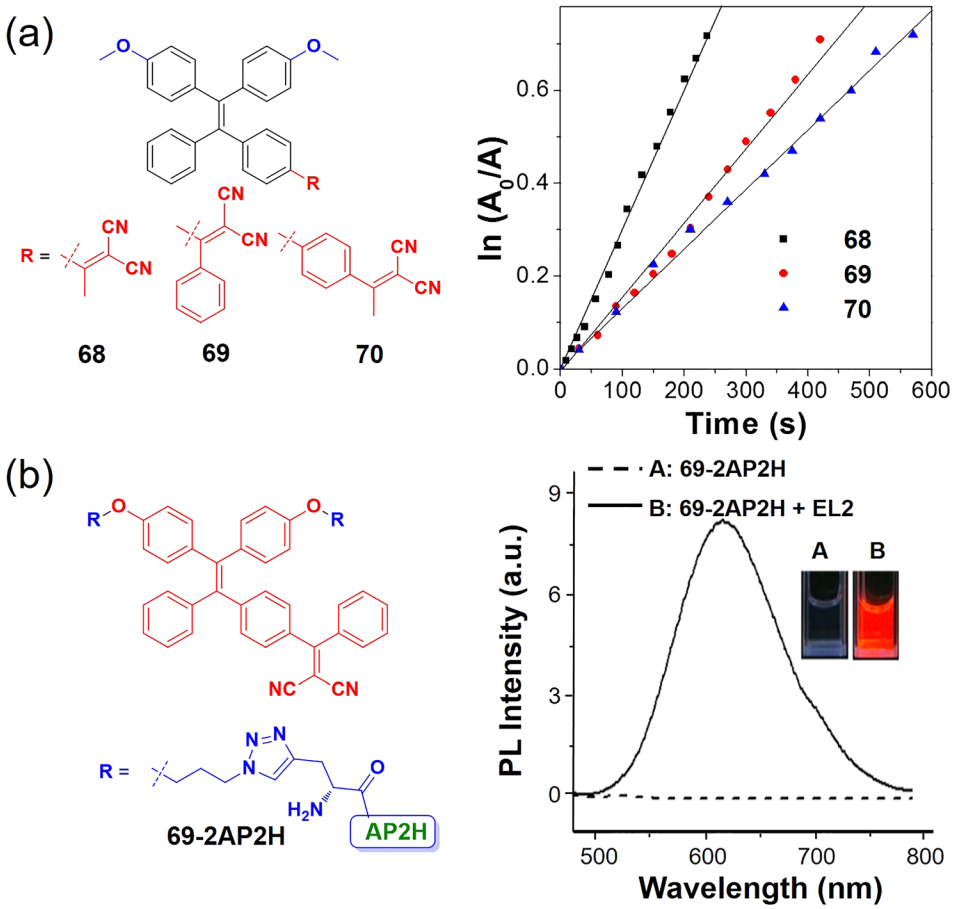

FIG. 31. (a) Chemical structures of **68, 69**, and **70** with different ΔE_{st}, and their photosensitizing ability measured by monitoring of the decomposition rate of $^1O_2$ indicator 9,10-anthracene-diyl-bis(methylene)dimalonic acid, under light irradiation. Reproduced with permission from Xu *et al.*, Chem. Sci. **6**, 5824 (2015). Copyright 2015 Royal Society of Chemistry. (b) Chemical structure of **69**-2AP2H and its light-up property upon binding to EL2. The inset shows the corresponding fluorescence. Reproduced with permission from Hu *et al.*, Anal. Chem. **86**, 7987 (2014). Copyright 2014 American Chemical Society.

decomposition rate towards the indicator [Fig. 31(a)] with the highest $^1O_2$ quantum yield of 89%, while the other two AIEgens also have relatively high $^1O_2$ quantum yields of 32% and 28%, respectively. It should be noted that all the tests were conducted in aqueous solution, where all three AIEgens formed aggregates with bright red emission under UV illumination. The dual functional AIE dots were then prepared using DSPE-PEG-Mal as the encapsulation matrix, and cell penetration peptide Tat as surface biomolecules to enhance cellular uptake, which showed an IC_{50} of 1.28 μg/ml,[169] revealing excellent photodynamic ablation of cancer cells.

On the other hand, AIE molecular probes can also be used as dual functional nanomaterials for targeted imaging and PDT of cancer cells.[170] We selected the probe developed by Zhang *et al.* as an example.[170] The probe consists of an AIE core (**69**) and two peripheries of 2AP2H (IHGHHIISVG) peptide [Fig. 31(b)]. The probe **69**-2AP2H has specific binding towards lysosomal transmembrane 4 beta (LAPTM4B) proteins that are overexpressed on most solid tumors. By introducing alkoxyl groups as the energy donor (D) and $-[PhC{=}C(CN)_2]$ as the energy acceptor (A) to TPE, the resultant AIEgen exhibits an emission maximum centered at 630 nm in aqueous buffer. In addition, the presence of $-[PhC{=}C(CN)_2]$ also endows the probe with strong photosensitizing ability to produce $^1O_2$ upon light irradiation. **69**-2AP2H is non-emissive in aqueous media, but it is able to selectively light up on the hydrophobic extracellular loop (PYRDDVMSVN) of LAPTM4B [Fig. 31(b)], making **69**-2AP2H an ideal probe for selective detection of cancer cells, such as HeLa cancer cells. The efficient $^1O_2$ generation further renders **69**-2AP2H as a non-invasive reagent for tumor treatment with minimized side effects to normal tissues with the help of fluorescence-guided light treatment. **69**-2AP2H showed very low cytotoxicity towards all the tested cells, while under light irradiation, it can cause quick cancer cell death to HeLa or U2OS cells with LAPTM4B overexpression, but not to HEK293 cells. The selectivity of such a probe has been further improved through the incorporation of enzyme-responsive peptides, such as -Gly-Phe-Leu-Gly, which could be cleaved by Cathepsin B, an enzyme over-expressed in the lysosome of cancer cells.[171] The dual-targeted probe has further reduced the intrinsic probe toxicity to offer more specific image-guided cancer ablation.

The theranostic platform offering the traceable cancer therapy attracted great research interest in personalized medicine. With this platform, it becomes possible to actively track when, where, and how the pharmaceutically active payload is delivered to cells as well as to monitor the *in situ* therapeutic response. Very recently, Liu *et al.* reported an all-in-one pH-response nanoprobe for tracking photosensitizer delivery, monitoring photosensitizer activation and the therapeutic response.[172] This nanoprobe is composed of a poly-L-lysine (PLL) grafted with diisopropylamino (DPA) side group to control probe hydrophobicity, **71** as an AIE fluorescence indicator, pheophorbide A (PheA) as the ACQ photosensitizer, and a PEG block for further conjugation with targeting ligands [Fig. 32(a)]. Benefiting from the protonation of DPA groups in acidic medium, the probe denoted

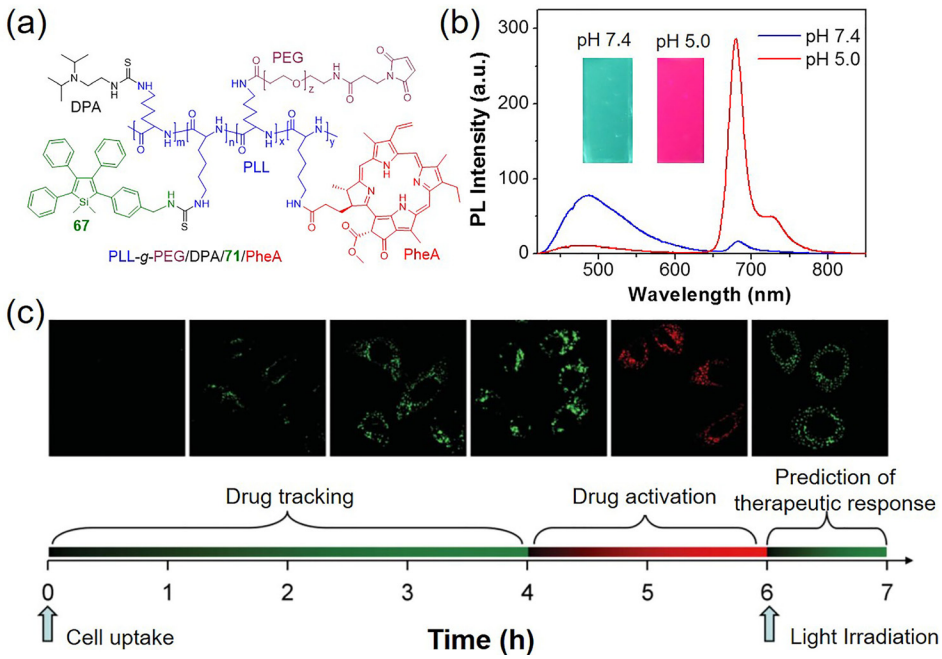

FIG. 32. (a) Chemical structures of PLL-*g*-PEG/DPA/**71**/PheA nanoprobe. (b) PL spectra of PLL-*g*-PEG/DPA/**71**/PheA at pH 7.4 and 5.0 upon excitation at 365 nm. Inset: the corresponding photographs taken under illumination of UV lamp at 365 nm. (c) Schematic illustration of the pH-responsive nanoprobe for self-tracking, PS activation monitoring, cancer cell ablation, and *in situ* therapeutic response prediction. Reproduced with permission from Yuan *et al.*, Small **11**, 4682 (2015). Copyright 2015 Wiley-VCH.

as PLL-g-PEG/DPA/**71**/PheA, shows pH-responsive behavior. At normal physiological condition of pH around 7.4, the nanoprobe forms aggregates and emits green fluorescence originated from **71** for self-tracking, where the red emission and $^1O_2$ production of PheA are quenched. While at acidic environment such as lysosome (pH = 5.0), DPA is protonated, the nanoprobe is disassembled, which results in diminished green emission and turn-on of red fluorescence as well as $^1O_2$ generation for phototoxicity [Fig. 32(b)]. In addition, the decreased probe size from 115.0 nm at pH = 7.4 to 15.0 nm at pH = 5.0 also verifies the disassembly of the nanoprobe. The probe was further conjugated with cRGD to target the integrin overexpressed cancer cells. Figure 32(c) demonstrates how the nanoprobe works for self-tracking, photosensitizer activation, cancer ablation, and *in situ* therapeutic response monitoring. Upon incubation MDA-MB-231 cells with the nanoprobe, the gradually increased punctuated green fluorescence inside cells clearly indicates the cellular uptake of the nanoprobe. The red fluorescence appears inside the MDA-MB-231 cells overlaps very well with the lysosomal stain, indicating that the nanoprobe is located at lysosomes. With increased incubation time, the red emission intensity further increases at the expense of green emission, indicating activation of the photosensitizer due to acidic environment of the lysosome. Upon light irradiation, the active PheA generates $^1O_2$ and leads to cell ablation as well as the disruption of lysosome. The reappearance of the green emission clearly indicates the therapeutic responses. In addition, other reagents such as drugs or up-conversion NPs have also been integrated with AIE PSs to realize combination therapy that is highly desirable for *in vivo* applications.[173–182]

V. SUMMARY AND OUTLOOK

In this review, we have introduced the plentiful opportunities for AIEgens to researchers from different perspectives. AIE represents a unique photophysical phenomenon that is exactly opposite to conventional ACQ. AIEgens can emit more efficiently in practically useful aggregate state than the solution state which generated great opportunities in various research disciplines such as optoelectronic devices, energy, environmental monitoring, materials themselves, etc. The working mechanism of AIE was defined as RIM, which was responsible for largely enhanced emission in aggregate state. Multiple AIE systems derived from AIEgens are introduced, including small molecules, macromolecules, and unconventional systems, which can be engineered and synthesized from incorporation of ACQ fluorogens with AIE units or building directly from AIEgens according to the RIM mechanism. At last, the technological applications of AIEgens in different fields from optoelectronic devices, physical or stimuli processes to biological applications are discussed with the scope focused on publications within the recent three years.

The study of AIE just started a decade ago. More investigations are still expected and await further exploration. The future advance of AIEgens should be focused on but not limited to deepen understanding of this unique photophysical process, design of novel molecular structures, development of innovative and real-world applications. Very recently, Aprahamian and Liptak *et al.* reported a novel class of AIEgens, which unveiled the AIE mechanism from another perspective of Kasha's rule.[183] They demonstrated that the emission of their AIEgens was from the states with higher energy rather than the singlet state ($>S_1$), where the RIM is able to be suppressed the internal conversion to the dark S_1 state, leading to this unique photophysical phenomenon. This study further reveals the important roles of activation of RIM: it not only modulates the excited state energy dissipation but also helps to tune the energy states of AIEgens. Such different approaches to exposit the mechanism, structure-property relationships and how the molecular packing and orientation affect the photophysical properties of AIEgens will guide the future design of molecules with

desirable functions. In addition, the promising performance of AIEgens in OLEDs, bioimaging as well as other fields encourages further exploration in the commercialized products. Several AIEgens are available on Sigma-Aldrich catalogue, and the biomedical start-up company "LuminiCell" has commercialized the breakthrough technology of AIE dots for long-term tracking of biological processes and vascular imaging.[184] As a novel class of fluorophores, the research and technological applications of AIEgens are still at the early stage. We hope that this review will stimulate more research interests from physics, chemistry, life science and biomedical fields. Together, we will further advance AIEgens as a tool for future light-based technologies.

ACKNOWLEDGMENTS

We thank the Singapore National Research Foundation (R-279-000-443-281, R279-000-483-281), National University of Singapore (R279-000-482-133), Institute of Materials Research and Engineering of Singapore (IMRE/14-8P1110), and the Hong Kong Innovation and Technology Commission (ITC-CNERC14SC01) for financial support.

[1]R. Y. Tsien, Angew. Chem. Int. Ed. **48**, 5612 (2009).
[2]L. Möckl, D. C. Lamb, and C. Bräuchle, Angew. Chem. Int. Ed. **53**, 13972 (2014).
[3]P. Von Dollen, S. Pimputkar, and J. S. Speck, Angew. Chem. Int. Ed. **53**, 13978 (2014).
[4]U. Resch-Genger, M. Grabolle, S. Cavaliere-Jaricot, R. Nitschke, and T. Nann, Nat. Methods **5**, 763 (2008).
[5]T. Förster and K. Kasper, Z. Phys. Chem. **1**, 275 (1954).
[6]Y. Hong, J. W. Y. Lam, and B. Z. Tang, Chem. Commun. **2009**, 4332.
[7]J. Luo, Z. Xie, J. W. Y. Lam, L. Cheng, H. Chen, C. Qiu, H. S. Kwok, X. Zhan, Y. Liu, D. Zhu, and B. Z. Tang, Chem. Commun. **2001**, 1740.
[8]B. Z. Tang, X. Zhan, G. Yu, P. P. Sze Lee, Y. Liu, and D. Zhu, J. Mater. Chem. **11**, 2974 (2001).
[9]J. Mei, N. L. C. Leung, R. T. K. Kwok, J. W. Y. Lam, and B. Z. Tang, Chem. Rev. **115**, 11718 (2015).
[10]J. Mei, Y. Hong, J. W. Y. Lam, A. Qin, Y. Tang, and B. Z. Tang, Adv. Mater. **26**, 5429 (2014).
[11]R. T. K. Kwok, C. W. T. Leung, J. W. Y. Lam, and B. Z. Tang, Chem. Soc. Rev. **44**, 4228 (2015).
[12]Y. Hong, J. W. Y. Lam, and B. Z. Tang, Chem. Soc. Rev. **40**, 5361 (2011).
[13]R. Hu, N. L. C. Leung, and B. Z. Tang, Chem. Soc. Rev. **43**, 4494 (2014).
[14]J. Liang, B. Z. Tang, and B. Liu, Chem. Soc. Rev. **44**, 2798 (2015).
[15]Z. Zhao, J. W. Y. Lam, and B. Z. Tang, J. Mater. Chem. **22**, 23726 (2012).
[16]D. Ding, K. Li, B. Liu, and B. Z. Tang, Acc. Chem. Res. **46**, 2441 (2013).
[17]M. Wang, G. Zhang, D. Zhang, D. Zhu, and B. Z. Tang, J. Mater. Chem. **20**, 1858 (2010).
[18]G.-F. Zhang, Z.-Q. Chen, M. P. Aldred, Z. Hu, T. Chen, Z. Huang, X. Meng, and M.-Q. Zhu, Chem. Commun. **50**, 12058 (2014).
[19]J. Shi, N. Chang, C. Li, J. Mei, C. Deng, X. Luo, Z. Liu, Z. Bo, Y. Q. Dong, and B. Z. Tang, Chem. Commun. **48**, 10675 (2012).
[20]S. Li, S. M. Langenegger, and R. Haner, Chem. Commun. **49**, 5835 (2013).
[21]G. Huang, G. Zhang, and D. Zhang, Chem. Commun. **48**, 7504 (2012).
[22]J. Zhao, D. Yang, Y. Zhao, X.-J. Yang, Y.-Y. Wang, and B. Wu, Angew. Chem. Int. Ed. **53**, 6632 (2014).
[23]Z. Shuai and Q. Peng, Phys. Rep. **537**, 123 (2014).
[24]A. Qin, J. W. Y. Lam, F. Mahtab, C. K. W. Jim, L. Tang, J. Sun, H. H. Y. Sung, I. D. Williams, and B. Z. Tang, Appl. Phys. Lett. **94**, 253308 (2009).
[25]J. Luo, K. Song, F. L. Gu, and Q. Miao, Chem. Sci. **2**, 2029 (2011).
[26]N. L. C. Leung, N. Xie, W. Yuan, Y. Liu, Q. Wu, Q. Peng, Q. Miao, J. W. Y. Lam, and B. Z. Tang, Chem.—A Eur. J. **20**, 15349 (2014).
[27]Z. He, L. Shan, J. Mei, H. Wang, J. W. Y. Lam, H. H. Y. Sung, I. D. Williams, X. Gu, Q. Miao, and B. Z. Tang, Chem. Sci. **6**, 3538 (2015).
[28]S. Hecht and J. M. J. Fréchet, Angew. Chem. Int. Ed. **40**, 74 (2001).
[29]L. Chen, S. Xu, D. McBranch, and D. Whitten, J. Am. Chem. Soc. **122**, 9302 (2000).
[30]J. Wang, Y. Zhao, C. Dou, H. Sun, P. Xu, K. Ye, J. Zhang, S. Jiang, F. Li, and Y. Wang, J. Phys. Chem. B **111**, 5082 (2007).
[31]Z. Zhao, S. Chen, J. W. Y. Lam, P. Lu, Y. Zhong, K. S. Wong, H. S. Kwok, and B. Z. Tang, Chem. Commun. **46**, 2221 (2010).
[32]Q. Zhao, X. A. Zhang, Q. Wei, J. Wang, X. Y. Shen, A. Qin, J. Z. Sun, and B. Z. Tang, Chem. Commun. **48**, 11671 (2012).
[33]J. Huang, J.-H. Su, and H. Tian, J. Mater. Chem. **22**, 10977 (2012).
[34]Z. Zhao, S. Chen, C. Y. K. Chan, J. W. Y. Lam, C. K. W. Jim, P. Lu, Z. Chang, H. S. Kwok, H. Qiu, and B. Z. Tang, Chem.–Asian J. **7**, 484 (2012).
[35]R. Hu, C. F. A. Gomez-Duran, J. W. Y. Lam, J. L. Belmonte-Vazquez, C. Deng, S. Chen, R. Ye, E. Pena-Cabrera, Y. Zhong, K. S. Wong, and B. Z. Tang, Chem. Commun. **48**, 10099 (2012).
[36]P. I. Shih, C. Y. Chuang, C. H. Chien, E. W. G. Diau, and C. F. Shu, Adv. Funct. Mater. **17**, 3141 (2007).
[37]Q. Zhao, K. Li, S. Chen, A. Qin, D. Ding, S. Zhang, Y. Liu, B. Liu, J. Z. Sun, and B. Z. Tang, J. Mater. Chem. **22**, 15128 (2012).
[38]H. Meng, S. Yang, Z. Li, T. Xia, J. Chen, Z. Ji, H. Zhang, X. Wang, S. Lin, C. Huang, Z. H. Zhou, J. I. Zink, and A. E. Nel, ACS Nano **5**, 4434 (2011).
[39]C.-A. Chou, R.-H. Chien, C.-T. Lai, and J.-L. Hong, Chem. Phys. Lett. **501**, 80 (2010).
[40]M. Shimizu, H. Tatsumi, K. Mochida, K. Shimono, and T. Hiyama, Chem.–Asian J. **4**, 1289 (2009).
[41]R. Hu, J. W. Y. Lam, Y. Liu, X. Zhang, and B. Z. Tang, Chem.–Eur. J. **19**, 5617 (2013).
[42]J. He, B. Xu, F. Chen, H. Xia, K. Li, L. Ye, and W. Tian, J. Phys. Chem. C **113**, 9892 (2009).
[43]Y.-X. Li, Z. Chen, Y. Cui, G.-M. Xia, and X.-F. Yang, J. Phys. Chem. C **116**, 6401 (2012).
[44]H. Pan, G.-L. Fu, Y.-H. Zhao, and C.-H. Zhao, Org. Lett. **13**, 4830 (2011).
[45]K. Kokado and Y. Chujo, Macromolecules **42**, 1418 (2009).
[46]M. Chen, L. Li, H. Nie, J. Tong, L. Yan, B. Xu, J. Z. Sun, W. Tian, Z. Zhao, A. Qin, and B. Z. Tang, Chem. Sci. **6**, 1932 (2015).
[47]J. E. Kwon and S. Y. Park, Adv. Mater. **23**, 3615 (2011).
[48]R. Wei, P. Song, and A. Tong, J. Phys. Chem. C **117**, 3467 (2013).
[49]Y. Chen, W.-C. Xu, J.-F. Kou, B.-L. Yu, X.-H. Wei, H. Chao, and L.-N. Ji, Inorg. Chem. Commun. **13**, 1140 (2010).
[50]K. Huang, H. Wu, M. Shi, F. Li, T. Yi, and C. Huang, Chem. Commun. **2009**, 1243.
[51]R. Hu, J. L. Maldonado, M. Rodriguez, C. Deng, C. K. W. Jim, J. W. Y. Lam, M. M. F. Yuen, G. Ramos-Ortiz, and B. Z. Tang, J. Mater. Chem. **22**, 232 (2012).
[52]C. Ma, Q. Ling, S. Xu, H. Zhu, G. Zhang, X. Zhou, Z. Chi, S. Liu, Y. Zhang, and J. Xu, Macromol. Biosci. **14**, 235 (2014).
[53]Y. Xu, L. Chen, Z. Guo, A. Nagai, and D. Jiang, J. Am. Chem. Soc. **133**, 17622 (2011).
[54]Y. Cui, Y. Yue, G. Qian, and B. Chen, Chem. Rev. **112**, 1126 (2012).
[55]Z. Wei, Z.-Y. Gu, R. K. Arvapally, Y.-P. Chen, R. N. McDougald, J. F. Ivy, A. A. Yakovenko, D. Feng, M. A. Omary, and H.-C. Zhou, J. Am. Chem. Soc. **136**, 8269 (2014).
[56]S. Dalapati, E. Jin, M. Addicoat, T. Heine, and D. Jiang, J. Am. Chem. Soc. **138**, 5797 (2016).
[57]Y. Tian, X. Yan, M. L. Saha, Z. Niu, and P. J. Stang, J. Am. Chem. Soc. **138**, 12033 (2016).
[58]Y. Lin, E. Balizan, L. A. Lee, Z. Niu, and Q. Wang, Angew. Chem. Int. Ed. **49**, 868 (2010).
[59]Z. Niu, J. Liu, L. A. Lee, M. A. Bruckman, D. Zhao, G. Koley, and Q. Wang, Nano Lett. **7**, 3729 (2007).
[60]Q. Zhu, L. Huang, Z. Chen, S. Zheng, L. Lv, Z. Zhu, D. Cao, H. Jiang, and S. Liu, Chem.–Eur. J. **19**, 1268 (2013).
[61]Y. Gong, Y. Tan, H. Li, Y. Zhang, W. Yuan, Y. Zhang, J. Sun, and B. Z. Tang, Sci. China Chem. **56**, 1183 (2013).
[62]X. Dou, X. Yuan, Y. Yu, Z. Luo, Q. Yao, D. T. Leong, and J. Xie, Nanoscale **6**, 157 (2014).
[63]M. S. Kwon, D. Lee, S. Seo, J. Jung, and J. Kim, Angew. Chem. Int. Ed. **53**, 11177 (2014).
[64]W. Z. Yuan, X. Y. Shen, H. Zhao, J. W. Y. Lam, L. Tang, P. Lu, C. Wang, Y. Liu, Z. Wang, Q. Zheng, J. Z. Sun, Y. Ma, and B. Z. Tang, J. Phys. Chem. C **114**, 6090 (2010).
[65]W. Zhao, Z. He, Jacky W. Y. Lam, Q. Peng, H. Ma, Z. Shuai, G. Bai, J. Hao, and B. Z. Tang, Chem **1**, 592 (2016).

[66]W. Qin, Z. Yang, Y. Jiang, J. W. Y. Lam, G. Liang, H. S. Kwok, and B. Z. Tang, Chem. Mater. **27**, 3892 (2015).
[67]Z. Ding, R. Xing, Q. Fu, D. Ma, and Y. Han, Org. Electron. **12**, 703 (2011).
[68]L. Chen, C. Zhang, G. Lin, H. Nie, W. Luo, Z. Zhuang, S. Ding, R. Hu, S.-J. Su, F. Huang, A. Qin, Z. Zhao, and B. Z. Tang, J. Mater. Chem. C **4**, 2775 (2016).
[69]W. Qin, J. W. Y. Lam, Z. Yang, S. Chen, G. Liang, W. Zhao, H. S. Kwok, and B. Z. Tang, Chem. Commun. **51**, 7321 (2015).
[70]S. Wang, X. Yan, Z. Cheng, H. Zhang, Y. Liu, and Y. Wang, Angew. Chem. Int. Ed. **54**, 13068 (2015).
[71]H. Uoyama, K. Goushi, K. Shizu, H. Nomura, and C. Adachi, Nature **492**, 234 (2012).
[72]S. Hirata, Y. Sakai, K. Masui, H. Tanaka, S. Y. Lee, H. Nomura, N. Nakamura, M. Yasumatsu, H. Nakanotani, Q. Zhang, K. Shizu, H. Miyazaki, and C. Adachi, Nat. Mater. **14**, 330 (2015).
[73]I. H. Lee, W. Song, and J. Y. Lee, Org. Electron. **29**, 22 (2016).
[74]B. Liu, H. Nie, X. Zhou, S. Hu, D. Luo, D. Gao, J. Zou, M. Xu, L. Wang, Z. Zhao, A. Qin, J. Peng, H. Ning, Y. Cao, and B. Z. Tang, Adv. Funct. Mater. **26**, 776 (2016).
[75]Z. Xie, C. Chen, S. Xu, J. Li, Y. Zhang, S. Liu, J. Xu, and Z. Chi, Angew. Chem. Int. Ed. **54**, 7181 (2015).
[76]C. D. Dimitrakopoulos and P. R. L. Malenfant, Adv. Mater. **14**, 99 (2002).
[77]J. Deng, Y. Xu, L. Liu, C. Feng, J. Tang, Y. Gao, Y. Wang, B. Yang, P. Lu, W. Yang, and Y. Ma, Chem. Commun. **52**, 2370 (2016).
[78]G. Yu, J. Gao, J. C. Hummelen, F. Wudl, and A. J. Heeger, Science **270**, 1789 (1995).
[79]Y. Liu, C. Mu, K. Jiang, J. Zhao, Y. Li, L. Zhang, Z. Li, J. Y. L. Lai, H. Hu, T. Ma, R. Hu, D. Yu, X. Huang, B. Z. Tang, and H. Yan, Adv. Mater. **27**, 1015 (2015).
[80]F. Hu, G. Zhang, C. Zhan, W. Zhang, Y. Yan, Y. Zhao, H. Fu, and D. Zhang, Small **11**, 1335 (2015).
[81]M. Debije, Nature **519**, 298 (2015).
[82]W. H. Weber and J. Lambe, Appl. Opt. **15**, 2299 (1976).
[83]M. G. Debije and P. P. C. Verbunt, Adv. Energy Mater. **2**, 12 (2012).
[84]J. L. Banal, B. Zhang, D. J. Jones, K. P. Ghiggino, and W. W. H. Wong, Acc. Chem. Res. **50**, 49 (2017).
[85]J. L. Banal, J. M. White, K. P. Ghiggino, and W. W. H. Wong, Sci. Rep. **4**, 4635 (2014).
[86]F. De Nisi, R. Francischello, A. Battisti, A. Panniello, E. Fanizza, M. Striccoli, X. Gu, N. L. C. Leung, B. Z. Tang, and A. Pucci, Mater. Chem. Front., "Red-emitting AIEgen for luminescent solar concentrators" (published online).
[87]P. Minei, E. Fanizza, A. M. Rodriguez, A. B. Munoz-Garcia, P. Cimino, M. Pavone, and A. Pucci, RSC Adv. **6**, 17474 (2016).
[88]M. Carlotti, E. Fanizza, A. Panniello, and A. Pucci, Sol. Energy **119**, 452 (2015).
[89]J. L. Banal, K. P. Ghiggino, and W. W. H. Wong, Phys. Chem. Chem. Phys. **16**, 25358 (2014).
[90]J. P. Riehl and F. S. Richardson, Chem. Rev. **86**, 1 (1986).
[91]J. Liu, H. Su, L. Meng, Y. Zhao, C. Deng, J. C. Y. Ng, P. Lu, M. Faisal, J. W. Y. Lam, X. Huang, H. Wu, K. S. Wong, and B. Z. Tang, Chem. Sci. **3**, 2737 (2012).
[92]J. C. Y. Ng, J. Liu, H. Su, Y. Hong, H. Li, J. W. Y. Lam, K. S. Wong, and B. Z. Tang, J. Mater. Chem. C **2**, 78 (2014).
[93]C. Weder, C. Sarwa, A. Montali, C. Bastiaansen, and P. Smith, Science **279**, 835 (1998).
[94]D. D. Prabhu, N. S. S. Kumar, A. P. Sivadas, S. Varghese, and S. Das, J. Phys. Chem. B **116**, 13071 (2012).
[95]D. Zhao, F. Fan, J. Cheng, Y. Zhang, K. S. Wong, V. G. Chigrinov, H. S. Kwok, L. Guo, and B. Z. Tang, Adv. Opt. Mater. **3**, 199 (2015).
[96]Y. Zhao, Z. Xie, H. Gu, C. Zhu, and Z. Gu, Chem. Soc. Rev. **41**, 3297 (2012).
[97]H. Wang, X. Gu, R. Hu, J. W. Y. Lam, D. Zhang, and B. Z. Tang, Chem. Sci. **7**, 5692 (2016).
[98]P. Duan, N. Yanai, Y. Kurashige, and N. Kimizuka, Angew. Chem. Int. Ed. **54**, 7544 (2015).
[99]A. P. de Silva and S. Uchiyama, Nat. Nanotechnol. **2**, 399 (2007).
[100]P. Ceroni, A. Credi, and M. Venturi, Chem. Soc. Rev. **43**, 4068 (2014).
[101]X. Mei, G. Wen, J. Wang, H. Yao, Y. Zhao, Z. Lin, and Q. Ling, J. Mater. Chem. C **3**, 7267 (2015).
[102]M. Tress, E. U. Mapesa, W. Kossack, W. K. Kipnusu, M. Reiche, and F. Kremer, Science **341**, 1371 (2013).
[103]R. Svoboda, P. Pustková, and J. Málek, Polymer **49**, 3176 (2008).
[104]S. Duwe, C. Arlt, S. Aranda, U. Riedel, and G. Ziegmann, Compos. Sci. Technol. **72**, 1324 (2012).
[105]S. Feng, Y. Chen, B. Mai, W. Wei, C. Zheng, Q. Wu, G. Liang, H. Gao, and F. Zhu, Phys. Chem. Chem. Phys. **16**, 15941 (2014).
[106]S. Bao, Q. Wu, W. Qin, Q. Yu, J. Wang, G. Liang, and B. Z. Tang, Polym. Chem. **6**, 3537 (2015).
[107]H.-H. Peng, J. Martel, Y.-H. Lee, D. M. Ojcius, and J. D. Young, Nanomedicine **6**, 643 (2011).
[108]R. Z. Khaliullin, H. Eshet, T. D. Kühne, J. Behler, and M. Parrinello, Nat. Mater. **10**, 693 (2011).
[109]X. Ye, Y. Liu, Y. Lv, G. Liu, X. Zheng, Q. Han, K. A. Jackson, and X. Tao, Angew. Chem. Int. Ed. **54**, 7976 (2015).
[110]J. M. Dragna, G. Pescitelli, L. Tran, V. M. Lynch, E. V. Anslyn, and L. Di Bari, J. Am. Chem. Soc. **134**, 4398 (2012).
[111]J. Li, Y. Li, C. Y. K. Chan, R. T. K. Kwok, H. Li, P. Zrazhevskiy, X. Gao, J. Z. Sun, A. Qin, and B. Z. Tang, Angew. Chem. Int. Ed. **53**, 13518 (2014).
[112]W. Guan, W. Zhou, C. Lu, and B. Z. Tang, Angew. Chem. Int. Ed. **54**, 15160 (2015).
[113]S. Ladet, L. David, and A. Domard, Nature **452**, 76 (2008).
[114]Y. Sun, Y. Li, J. Nie, Z. Wang, and Q. Hu, Chem. Lett. **42**, 838 (2013).
[115]F. Fergg, F. J. Keil, and H. Quader, Colloid Polym. Sci. **279**, 61 (2001).
[116]Z. Wang, J. Nie, W. Qin, Q. Hu, and B. Z. Tang, Nat. Commun. **7**, 12033 (2016).
[117]Q. Li, L. Chen, M. R. Gadinski, S. Zhang, G. Zhang, H. Li, A. Haque, L.-Q. Chen, T. Jackson, and Q. Wang, Nature **523**, 576 (2015).
[118]W. Guan, S. Wang, C. Lu, and B. Z. Tang, Nat. Commun. **7**, 11811 (2016).
[119]K. Ariga, T. Mori, and J. P. Hill, Adv. Mater. **24**, 158 (2012).
[120]T. Hu, B. Yao, X. Chen, W. Li, Z. Song, A. Qin, J. Z. Sun, and B. Z. Tang, Chem. Commun. **51**, 8849 (2015).
[121]C. Feng, K. Wang, Y. Xu, L. Liu, B. Zou, and P. Lu, Chem. Commun. **52**, 3836 (2016).
[122]Q. Zhang, J. Su, D. Feng, Z. Wei, X. Zou, and H.-C. Zhou, J. Am. Chem. Soc. **137**, 10064 (2015).
[123]Z. Wang, H. Nie, Z. Yu, A. Qin, Z. Zhao, and B. Z. Tang, J. Mater. Chem. C **3**, 9103 (2015).
[124]D. R. Larson, W. R. Zipfel, R. M. Williams, S. W. Clark, M. P. Bruchez, F. W. Wise, and W. W. Webb, Science **300**, 1434 (2003).
[125]D. Ivnitski, I. Abdel-Hamid, P. Atanasov, and E. Wilkins, Biosens. Bioelectron. **14**, 599 (1999).
[126]A. C. Gales, A. O. Reis, and R. N. Jones, J. Clin. Microbiol. **39**, 183 (2001).
[127]E. Zhao, Y. Hong, S. Chen, C. W. T. Leung, C. Y. K. Chan, R. T. K. Kwok, J. W. Y. Lam, and B. Z. Tang, Adv. Healthcare Mater. **3**, 88 (2014).
[128]E. Zhao, Y. Chen, S. Chen, H. Deng, C. Gui, C. W. T. Leung, Y. Hong, J. W. Y. Lam, and B. Z. Tang, Adv. Mater. **27**, 4931 (2015).
[129]G. Feng, Y. Yuan, H. Fang, R. Zhang, B. Xing, G. Zhang, D. Zhang, and B. Liu, Chem. Commun. **51**, 12490 (2015).
[130]B. K. Hubbard and C. T. Walsh, Angew. Chem. Int. Ed. **42**, 730 (2003).
[131]S. Y. Park, H. J. Baik, Y. T. Oh, K. T. Oh, Y. S. Youn, and E. S. Lee, Angew. Chem. Int. Ed. **50**, 1644 (2011).
[132]G. Liang, J. W. Y. Lam, W. Qin, J. Li, N. Xie, and B. Z. Tang, Chem. Commun. **50**, 1725 (2014).
[133]Y. Yang, Q. Zhao, W. Feng, and F. Li, Chem. Rev. **113**, 192 (2013).
[134]Y. Li, Y. Wu, J. Chang, M. Chen, R. Liu, and F. Li, Chem. Commun. **49**, 11335 (2013).
[135]M. Gao, Q. Hu, G. Feng, B. Z. Tang, and B. Liu, J. Mater. Chem. B **2**, 3438 (2014).
[136]A. T. Hoye, J. E. Davoren, P. Wipf, M. P. Fink, and V. E. Kagan, Acc. Chem. Res. **41**, 87 (2008).
[137]N. Zhao, M. Li, Y. Yan, J. W. Y. Lam, Y. L. Zhang, Y. S. Zhao, K. S. Wong, and B. Z. Tang, J. Mater. Chem. C **1**, 4640 (2013).
[138]X. Gu, E. Zhao, T. Zhao, M. Kang, C. Gui, J. W. Y. Lam, S. Du, M. M. T. Loy, and B. Z. Tang, Adv. Mater. **28**, 5064 (2016).
[139]M. F. Kircher, S. S. Gambhir, and J. Grimm, Nat. Rev. Clin. Oncol. **8**, 677 (2011).
[140]G. Feng, C. Y. Tay, Q. X. Chui, R. Liu, N. Tomczak, J. Liu, B. Z. Tang, D. T. Leong, and B. Liu, Biomaterials **35**, 8669 (2014).
[141]K. Li, Z. Zhu, P. Cai, R. Liu, N. Tomczak, D. Ding, J. Liu, W. Qin, Z. Zhao, Y. Hu, X. Chen, B. Z. Tang, and B. Liu, Chem. Mater. **25**, 4181 (2013).
[142]W. Qin, K. Li, G. Feng, M. Li, Z. Yang, B. Liu, and B. Z. Tang, Adv. Funct. Mater. **24**, 635 (2014).

[143]K. Li, W. Qin, D. Ding, N. Tomczak, J. Geng, R. Liu, J. Liu, X. Zhang, H. Liu, B. Liu, and B. Z. Tang, Sci. Rep. **3**, 1150 (2013).
[144]D. Ding, D. Mao, K. Li, X. Wang, W. Qin, R. Liu, D. S. Chiam, N. Tomczak, Z. Yang, B. Z. Tang, D. Kong, and B. Liu, ACS Nano **8**, 12620 (2014).
[145]Y. Jiang, B. N. Jahagirdar, R. L. Reinhardt, R. E. Schwartz, C. D. Keene, X. R. Ortiz-Gonzalez, M. Reyes, T. Lenvik, T. Lund, M. Blackstad, J. Du, S. Aldrich, A. Lisberg, W. C. Low, D. A. Largaespada, and C. M. Verfaillie, Nature **418**, 41 (2002).
[146]C. W. T. Leung, Y. Hong, S. Chen, E. Zhao, J. W. Y. Lam, and B. Z. Tang, J. Am. Chem. Soc. **135**, 62 (2013).
[147]Z. Wang, S. Chen, J. W. Y. Lam, W. Qin, R. T. K. Kwok, N. Xie, Q. Hu, and B. Z. Tang, J. Am. Chem. Soc. **135**, 8238 (2013).
[148]O. C. Boerman, H. Rennen, W. J. G. Oyen, and F. H. M. Corstens, Semin. Nucl. Med. **31**, 286 (2001).
[149]E. Vandenbroucke, D. Mehta, R. Minshall, and A. B. Malik, Ann. N. Y. Acad. Sci. **1123**, 134 (2008).
[150]M. H. Barnett and J. W. Prineas, Ann. Neurol. **55**, 458 (2004).
[151]D. Ding, C. C. Goh, G. Feng, Z. Zhao, J. Liu, R. Liu, N. Tomczak, J. Geng, B. Z. Tang, L. G. Ng, and B. Liu, Adv. Mater. **25**, 6083 (2013).
[152]D. Wang, J. Qian, W. Qin, A. Qin, B. Z. Tang, and S. He, Sci. Rep. **4**, 4279 (2014).
[153]J. Geng, C. C. Goh, W. Qin, R. Liu, N. Tomczak, L. G. Ng, B. Z. Tang, and B. Liu, Chem. Commun. **51**, 13416 (2015).
[154]G. S. He, L.-S. Tan, Q. Zheng, and P. N. Prasad, Chem. Rev. **108**, 1245 (2008).
[155]J. Qian, Z. Zhu, A. Qin, W. Qin, L. Chu, F. Cai, H. Zhang, Q. Wu, R. Hu, B. Z. Tang, and S. He, Adv. Mater. **27**, 2332 (2015).
[156]Y. Gao, G. Feng, T. Jiang, C. Goh, L. Ng, B. Liu, B. Li, L. Yang, J. Hua, and H. Tian, Adv. Funct. Mater. **25**, 2857 (2015).
[157]B. Chen, G. Feng, B. He, C. Goh, S. Xu, G. Ramos-Ortiz, L. Aparicio-Ixta, J. Zhou, L. Ng, Z. Zhao, B. Liu, and B. Z. Tang, Small **12**, 782 (2016).
[158]J. Xiang, X. Cai, X. Lou, G. Feng, X. Min, W. Luo, B. He, C. C. Goh, L. G. Ng, J. Zhou, Z. Zhao, B. Liu, and B. Z. Tang, ASC Appl. Mater. Interfaces **7**, 14965 (2015).
[159]J. Geng, C. C. Goh, N. Tomczak, J. Liu, R. Liu, L. Ma, L. G. Ng, G. G. Gurzadyan, and B. Liu, Chem. Mater. **26**, 1874 (2014).
[160]M. S. Muthu, D. T. Leong, L. Mei, and S.-S. Feng, Theranostics **4**, 660 (2014).
[161]T. Lammers, S. Aime, W. E. Hennink, G. Storm, and F. Kiessling, Acc. Chem. Res. **44**, 1029 (2011).
[162]J. Kim, Y. Piao, and T. Hyeon, Chem. Soc. Rev. **38**, 372 (2009).
[163]R. Bardhan, S. Lal, A. Joshi, and N. J. Halas, Acc. Chem. Res. **44**, 936 (2011).
[164]H. Shi, J. Liu, J. Geng, B. Z. Tang, and B. Liu, J. Am. Chem. Soc. **134**, 9569 (2012).
[165]H. Shi, R. T. K. Kwok, J. Liu, B. Xing, B. Z. Tang, and B. Liu, J. Am. Chem. Soc. **134**, 17972 (2012).
[166]I. J. Macdonald and T. J. Dougherty, J. Porphyrins Phthalocyanines **5**, 105 (2001).
[167]L. E. Bennett, K. P. Ghiggino, and R. W. Henderson, J. Photochem. Photobiol. B: Biol. **3**, 81 (1989).
[168]Y. Yuan, G. Feng, W. Qin, B. Z. Tang, and B. Liu, Chem. Commun. **50**, 8757 (2014).
[169]S. Xu, Y. Yuan, X. Cai, C.-J. Zhang, F. Hu, J. Liang, G. Zhang, D. Zhang, and B. Liu, Chem. Sci. **6**, 5824 (2015).
[170]F. Hu, Y. Huang, G. Zhang, R. Zhao, H. Yang, and D. Zhang, Anal. Chem. **86**, 7987 (2014).
[171]Y. Yuan, C.-J. Zhang, M. Gao, R. Zhang, B. Z. Tang, and B. Liu, Angew. Chem. Int. Ed. **54**, 1780 (2015).
[172]Y. Yuan, R. T. K. Kwok, B. Z. Tang, and B. Liu, Small **11**, 4682 (2015).
[173]Y. Yuan, R. T. K. Kwok, R. Zhang, B. Z. Tang, and B. Liu, Chem. Commun. **50**, 11465 (2014).
[174]Y. Yuan, Y. Chen, B. Z. Tang, and B. Liu, Chem. Commun. **50**, 3868 (2014).
[175]G. Feng, W. Wu, S. Xu, and B. Liu, ASC Appl. Mater. Interfaces **8**, 21193 (2016).
[176]Y. Yuan, S. Xu, C.-J. Zhang, and B. Liu, Polym. Chem. **7**, 3530 (2016).
[177]Y. Yuan, S. Xu, X. Cheng, X. Cai, and B. Liu, Angew. Chem. Int. Ed. **55**, 6457 (2016).
[178]R. Zhang, G. Feng, C.-J. Zhang, X. Cai, X. Cheng, and B. Liu, Anal. Chem. **88**, 4841 (2016).
[179]Y. Yuan, C.-J. Zhang, S. Xu, and B. Liu, Chem. Sci. **7**, 1862 (2016).
[180]G. Jin, G. Feng, W. Qin, B. Z. Tang, B. Liu, and K. Li, Chem. Commun. **52**, 2752 (2016).
[181]Y. Yuan, C.-J. Zhang, R. T. K. Kwok, S. Xu, R. Zhang, J. Wu, B. Z. Tang, and B. Liu, Adv. Funct. Mater. **25**, 6586 (2015).
[182]G. Feng, W. Qin, Q. Hu, B. Z. Tang, and B. Liu, Adv. Healthcare Mater. **4**, 2667 (2015).
[183]H. Qian, M. E. Cousins, E. H. Horak, A. Wakefield, M. D. Liptak, and I. Aprahamian, Nat. Chem. **9**, 83 (2017).
[184]X. Lim, Nature **531**, 26 (2016).